Universität der Bundeswehr München
Institut für
Mechanik

Universität der Bundeswehr München

On the Effects of Ozone-induced Ageing on the Mechanical Properties of Natural Rubber

Caroline Treib

Vollständiger Abdruck der von der Fakultät für Luft- und Raumfahrttechnik der
Universität der Bundeswehr München zur Erlangung des akademischen Grades eines

Doktor-Ingenieurs (Dr.-Ing.)

angenommenen Dissertation.

Gutachter 1: Prof. PD Dr.-Ing. habil. Michael Johlitz
Gutachter 2: Univ.-Prof. Dr. Sci. (Tech.) Leif Kari

Die Dissertation wurde am 29.04.2024 bei der Universität der Bundeswehr eingereicht
und durch die Fakultät für Luft- und Raumfahrttechnik am 01.10.2024 angenommen.
Die mündliche Prüfung fand am 11.10.2024 statt.

Acknowledgements

First and foremost, I want to thank my supervisor Prof. Michael Johlitz, not only for the scientific support, but also for 'adopting' me into the Institute of Mechanics at a crossroads in my professional life! Your trust in my success, no matter which problems occured during the experimental part, kept me heading forward to find solutions. Besides all the professional supervision, thank you for ensuring festivities take place and weld the team together with grilled fish in the inner yard or a 'Dienstausflug', as I might have called it.

On one of the plenty conferences you enabled me to participate in, I had the pleasure to meet Prof. Leif Kari, whom I want to thank for the fruitful discussions, nice jokes on the 'supervising life now' and for accepting to be the second reviewer of this dissertation.

Moreover, I want to thank Prof. Alexander Lion. Your passion for mechanics is omnipresent in the insitute and your patience to answer every question - as simple as they must seem to you - is a wonderful gift.

A special part in the process of writing this thesis and therefore many thanks belong to the reseach group at LRT4, making my time at the insitute truly memorable for me! You were always helping me with your experience in experiments and simulation - whenever, wherever necessary! Starting with daily fresh brewed coffee by Dominik and Johannes to band sessions - thank you Bruno for making me improvise without sheets - over hikes, diving experience and sight seeing on holidays. Special thanks to my 'roommates': Tomas and Ondrej for the vynikajúce times and to Michi, without you I would probably still sit in the lab. Thank you Klara for being such a cheerful, energising friend. My 'tremendous' gratitude goes to the LRT4 team.

The many hours spent in the laboratory, I had the pleasure to work with remarkable students as Toni Wollmershäuser, John Bartels, Nicholas Lemos, and Louis-Marie Hardy. Thank you for your curiosity and motivation to contribute not only to finish a thesis but to a greater research question with endurance and precision.

I'd also like to thank the university for offering the mentoring program that gave me the chance to meet Patricia Parlevliet. Thank you for your inspiration and investing your time in mentoring me.

Sometimes, only the UniBw volleyball team kept my body alive after the long hours at the desk or lab. Thank you for always offering an after-workout chat with 'Spezi' or beer, the fun on tournaments and nice evenings with barbecue at the beach courts.

After work, at days without success and no solution in sight as on days to celebrate, my friends and family are always there for me. I truly want to thank you all for listening, encouraging, and partying with me - simply for enriching my life!

Lena and Nick, you are the most genuine, wonderful friends anyone could ask for and you will forever be the best flatmates I will have had, thank you for leveling my ups and downs!

My cuddlemonster, thank you for showing me the benefits of using Vim and Git though me being reluctant to adopt the new tools and 'pomming' around. You make me feel special, laughing honestly when I question my expertise.

Lastly, to my greater family: thank you for the openmindedness and integrity anchoring faith in the good in my world. To my brothers for being role models to me that I can rely on in any situation. Finally, I want to thank my parents for their unshatterable love, patience and support.

~

Kurzfassung

Die Ozonalterung von Naturkautschukvulkanisaten führt in industriellen Anwendungen zu schneller Rissbildung und verkürzter Lebensdauer. Eine Vorhersage des Degradationszustandes ist notwendig, um Komponenten möglichst lange zu nutzen jedoch rechtzeitig zu ersetzen. Das Ziel dieser Arbeit ist die Auswahl eines geeigneten Alterungsparameters und die Modellierung des Ozonalterungsverhaltens anhand generierter Messdatensätze. Dazu werden thermische, chemische und mechanische Experimente durchgeführt, um ein besseres Verständnis des Ablaufs der Ozonalterung zu erhalten und die daraus resultierenden Materialveränderungen zu quantifizieren. Dazu wird ein beschleunigter Alterungsprozess unter Berücksichtigung von Einflussparametern entwickelt und durchgeführt, um die Veränderungen im Material hinsichtlich ihrer Eignung zur quantitativen Beschreibung des Alterungsprozesses zu bewerten. Die Alterungsparameter umfassen unter anderem die Ozonkonzentration, die Alterungszeit und die Temperatur. Neben Veränderungen der thermischen und chemischen Eigenschaften an der Oberfläche ist die Rissbildung das dominanteste Alterungsmerkmal. Die gemessene Risstiefenentwicklung wird zur Erstellung einer Evolutionsgleichung über die Alterungszeit in Abhängigkeit der Ozonkonzentration genutzt. Der maximale Rissfortschritt lässt sich auch bei Verwendung von chemischen Antiozonanten mittles derselben Evolutionsgleichung simulieren. Lediglich durch die Verwendung von Ozonschutzwachs weist die Entwicklung der Risse einen signifikant anderen Verlauf auf. Der Rissentwicklung aller betrachteten Mischungen gemein ist die Verlangsamung ohne finale Stagnation der Rissbildung. Durch die Simulation der künstlichen Alterung im Labor bei verschiedenen erhöhten Ozonkonzentrationen wird ein Bezug zu realistischen niedrigeren Ozonbelastungen hergestellt.

Abstract

The ozone ageing of natural rubber leads to fast cracks and a reduced lifetime of components in industrial applications. To replace fatal components, it is necessary to predict the degradation status, whereby the ultimate objective is to generate a database to model the evolution of the material's ozone-ageing behaviour. To this end, thermal, chemical, and mechanical experiments are conducted to gain more insight into the process of ozone ageing and quantify the resulting changes. An accelerated ageing process is developed to consider various influencing parameters such as the ozone concentration, ageing time, and temperature. The resulting changes are evaluated, based on their usefulness to describe the ageing process. Apart from changes in the thermal and chemical characteristics of the surface, the cracking for ageing under strain is the predominant ageing characteristic. An evolution equation is derived for the development of crack depth in the cross-section. A similar evolution is present for natural rubber compounds with and without antiozonants, except if wax is part of the compound as this leads to different crack growth rates. The findings indicate a deceleration but no stagnation of crack growth and enable a relation of accelerated ageing time under increased ozone concentration to realistic ozone loading for long periods.

Contents

List of Symbols

Symbol	**Description**	**Unit**
σ_R	1. Piola-Kirchhoff stress	$\mathrm{N\,mm^{-2}}$
σ	Cauchy stress	$\mathrm{N\,mm^{-2}}$
t_a	Ageing time	h
A	Area	mm
r	Correlation coefficient	nan
h_c	Crack depth	µm
Q	Differential heat flow	$\mathrm{mW\,mg^{-1}}$
F	Force	N
T_g	Glass transition temperature	K
h	Height	mm
n_X	Number of conducted load cycles at force X	nan
N_X	Number of load cycles at failure at force X	nan
c_{oz}	Ozone concentration	pphm
m_p	Sample mass (DSC)	µg
m_s	Sapphire sample mass (DSC)	µg
p	Significance Level	nan
c	Species concentration	$\mathrm{mol/m^3}$
c_p	Specific heat capacity	$\mathrm{J\,g^{-1}\,K^{-1}}$
ϵ	Strain	%
λ	Strain	nan
T	Temperature	K
t	Time	s
b	Width	mm

List of Abbreviations

Abbr.	**Description**
6PPD	*N*-(1,3-dimethylbutyl)-*N*′-phenyl-p-phenylenediamine
BR	Butadiene rubber
`C1`	Compound 1 (with 6PPD and wax)
`C2`	Compound 2 (with 6PPD)
`C3`	Compound 3 (without antiozonants)
DLO	Diffusion-limited oxidation
DMA	Dynamic mechanical analysis
DSC	Differential scanning calorimetry
EIT	Indentation Modulus
`EXP`	Exponential function based on monomolecuar reaction Eq.(4.9)
FT-IR	Fourier transform infrared spectroscopy
GA	Genetic algorithm
χ	Goodness of fit
`LIN`	Loagrithmic Linear function Eq.(4.10)
`LN+`	Modified logaritmic function Eq.(4.11)
`LR`	Linear regression
LSM	Laser Scanning Microscope
MAE	Mean absolute error
MAEr	Mean relative absolute error
MCT	Micro computer tomography
NAAQS	National Ambient Air Quality Standards
NMVOC	Non-methane volatile organic compound
NR	Natural rubber
PDMS	Polydimethylsiloxane
PK	Piola-Kirchhoff
PMMA	Polymethylmethacrylate
`POW`	Power law function Eq.(4.12)
PPD	*p*-phenylenediamine
PyGC-MS	Pyrolysis-gas chromatography mass spectrometry
RMSE	Root-mean-square Error

SIC	Strain-induced-crystallisation
UV	Ultra-violet
VOCs	Volatile organic compounds
pphm	Parts per hundred million
ppm	Parts per million

List of Figures

Buy less, choose well, make it last.

— Vivienne Westwood

1

Introduction

Contents

1.1 Motivation

The Unique Characteristics of Natural Rubber (NR)

NR is an irreplaceable ingredient in industrial components in construction, combustion, or the aviation industry. It achieves excellent values in the so-called magic triangle of abrasion resistance, wet grip, and rolling resistance which presents a constant challenge for tyres. Regarding earth mover tyres, a large crack growth resistance is necessary, which NR can deliver by high strain-induced-crystallisation (SIC) [1] and with elongations at break of approximately 700 %. Additionally, the isolation capabilities of NR are deployed in applications such as earthquake or bridge bearings and for suspension joints in bridges that benefit from the low heat built up at moderate deformations. Further characteristics

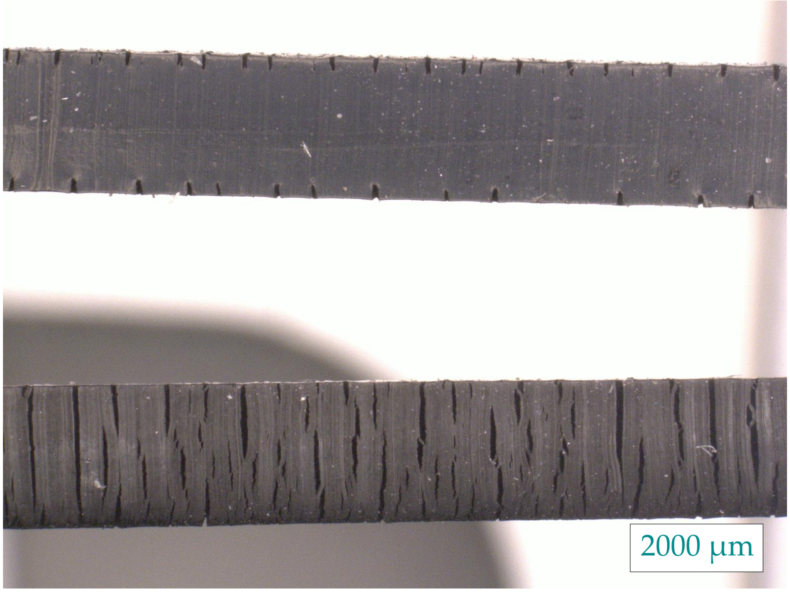

Figure 1.1 Cracks in the cross-section and surface of ozone-aged NR at 52 pphm (pars per hundred million) ozone for 37 hours under 20 % strain.

of NR are described in Section 1.3.1.

Impact of Ozone on Rubber

Apart from mechanical loads, environmental loads affect material characteristics and durability. In this context, influence is attributed to temperature, UV light, and humidity, in addition to surrounding media such as oil, fuel, oxygen, and ozone. Especially irreversible chemical attacks, such as from gaseous ozone, markedly change the material characteristics and service life, as indicated by Braden and Gent [2] and the literature review prepared by Mars and Fatemi [3]. The antioxidants that are used to prevent thermo-oxidative and thermal ageing are not necessarily effective against ozone [4] and the damage caused by ozone accelerates the reduction of lifetime by fast cracking, see Figure 1.1, outpacing the degradation by thermo-oxidative ageing [5]. With high crack growth resistance being a special characteristic of NR [1], the presence of crack depth due to ageing is decisive for the reduction of capacity of an NR component.

Environmental Impact of NR Production

NR is a polymer that is largely harvested in nature from one plant, namely *hevea brasiliensis*. The use of intensive monoculture practices to supply the demand for rubber in industry resulted in parasites and fungal diseases proliferating throughout former cultivation areas in South America. Today, more than half of

NR production is located in South Asia and significant parts in Africa [6].

To date, the only competitive source of NR is *hevea brasiliensis*. However, generating NR from the roots of other plants (Taraxacum kok-saghyz) and (Scorzonera tau-saghyz) has been explored for some time and these options are recently being re-examined [7–11]. The rubber content is increased by the cultivation of plants to generate latex in a commercially attractive concentration. Since 2018, *Continental*© sells bicycle tyres made solely from dandelion rubber, although the biggest share of the world market is used in tyres for cars and trucks and the alternative has not yet reached the high performative area. Overall, the annual world consumption of NR is approximately 14 million tonnes, which is double the value compared to 20 years ago [12]. There are numerous other applications for NR in most areas of industry and in everyday life, including isolators for bridges or motors, hoses, and sealings. In addition to the limits to natural production, various forecasts on ground-level-ozone values predict trends to higher values due to climate change, thereby increasing the ozone-dependent degradation of NR components. Consequently, the prolonging of service life is examined by understanding and predicting damage mechanisms. Economic and ecological interest raises questions concerning the optimal cost-effectiveness in relation to aspects of safety and durability regarding the challenges in material production closely connected to raw material costs, trends of ozone levels, and field damage cases. Extended durability and prolonged service life are common customer requests, as outlined in the work of Andrew [13] and Zaghdoudi *et al.* [14].

Therefore, it is necessary to advance scientific knowledge about degradation of NR to address the challenge of maximal use time and least material waste. For example, in bridge bearings, predictive maintenance saves additional connected costs for closing roads and lifting bridge decks for the exchange. In this context, the known damage due to ozone includes the rapid development of a hardened surface layer, named frosting, leading to cracks for low strain levels. However, the extent of the damage is not predictable to date, despite its importance for enhancing material use. Thus, the motivation and aim of the research outlined in this thesis is to determine the evolution of the ozone ageing process in NR depending on the loading history.

1.2 Research Objective and Structure of the Thesis

The research objective is to derive an enhanced understanding of the ageing of NR due to ozone. The findings will be applied to develop approaches for a better selection of additives to protect and sustain NR as a resource for the future. To this end, a degradation characteristic will be selected based on an artificial ageing procedure accelerating the real ageing conditions to quantify the evolution of degradation and be able to predict the ageing state for a more precise replacement schedule.

In Chapter 2, artificial ageing is discussed to model ground-level ozone loading on NR. As a result, suitable ageing parameters are chosen for the sample geometries available.

Subsequently, the consequences of the artificial ageing procedure are experimentally analysed in Chapter 3. Ozone-related chemical, thermal, and mechanical changes in NR are identified and quantified using several experimental approaches. The results are documented and discussed in Section 3.4, which deduces the main ageing parameters apart from ozone concentration: ageing time, mechanical strain, and ageing protectants. The most relevant damage variable is considered to be the crack development which is quantified by its depth.

Considering the damage variable crack depth, an evolution is derived and validated in Chapter 4 to predict the damage relating to lower ozone concentrations over long exposure times.

In Chapter 5, the results are concluded and existing and innovative protection approaches are discussed which might be analysed in future studies.

1.3 State of the Art

1.3.1 Overview of the Properties of Rubber

The chemical monomer structure of NR is `poly(cis-1,4-isoprene)`. Through polymerisation, chain lengths of over 100 000 isoprene units are formed that are connected in a wide meshed network.

Isoprene monomer:

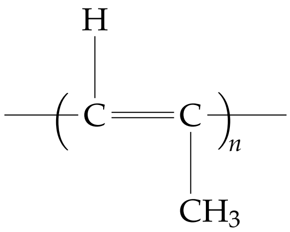

$$-\left(\overset{\displaystyle H}{\overset{|}{C}}=\underset{\underset{\displaystyle CH_3}{|}}{C}\right)_n-$$

Prior to the vulcanisation process, these chains are entangled but not connected. Controlled by additives, elevated temperature and pressure, with the addition of sulphur, cross-linking is induced among the chains. This process was elucidated by Charles Goodyear in 1839. Since NR decomposes at high temperatures, there is an optimum for the vulcanisation parameters. The most common vulcanisation is sulphur cross-linking for NR, however vulcanisation with peroxides is also possible. Although crosslinking prevents chain slippage, mechanical deformation may stretch the chains into less favourable thermodynamic configurations, thereby reducing entropy. When the external force is released, the system returns to its original intertwined state.

Two states of the material can be classified over temperature, defined as rubbery and glassy states, which are distinguished by the glass transition temperature T_g. Above T_g, the material is entropy-elastic, as entropy changes lead to its elastic behaviour above T_g, while below this temperature, it is energy elastic in the glassy state. In NR, this transition occurs around -50 to $-65\,°\mathrm{C}$, which makes the entropy elastic state the application area.

To adapt the material characteristics of elastomers, the initial ingredients are customised and crosslinking levels are adjusted by vulcanisation parameters and additives. Further, by adding non-entropy-elastic fillers, the properties can be modified regarding their abrasion resistance and tensile strength. Carbon black (CB) plays a pivotal role among the active fillers, and it is available in various types specified by surface area, size, colour, or even the conductivity used to enhance mechanical properties such as tensile strength or simply to increase the volume.

Within the entropy elastic state, NR is increasingly nonlinear elastic, with deformation resulting in an S-shaped stress-strain curve. Although it regains its original configuration, due to its viscoelastic characteristics, this requires a certain amount of time depending on the load history. The viscoelastic behaviour leads to a dependence on deformation rate without equilibrium hysteresis being beneficial for isolation applications, while the heat build-up is low during harmonic loading. The damping behaviour under dynamic load can be assessed by loss and storage moduli that display dependence on the amplitude in a process termed the *Payne Effect*. In addition, the so-called *Mullins Effect* describes a strain-induced softening depending on the maximum load. It is only observed in filled elastomers and is thus associated with a filler-to-network interaction and, possibly, breakage of the filler-to-network bonds. However, with time, the bonds can be recreated, thereby making the effect reversible in the long term. Research to comprehensively characterise and model the dynamic material properties of filled NR are still ongoing especially considering ageing phenomena [15, 16].

The elongation at break of NR is extremely high, at several 100 %, making it difficult to measure for its almost incompressible behaviour leading to intense lateral contraction. In combination with the unique SIC, this leads to an outstanding crack growth resistance, as shown by [17–22]. Gehling *et al.* [1] emphasises the benefit of the SIC behaviour to dynamic fatigue tests correlated to the increase of crack tip bifurcation with SIC.

1.3.2 Fundamental Characteristics of Ozone

Ozone molecules are unstable, with a half-life of approximately 3 days in laboratory conditions depending on temperature, humidity, and air movement [23].

Molecular structure:

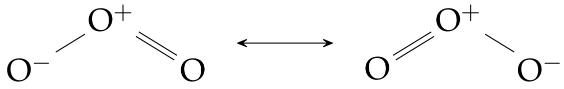

As a strong oxidant, the ozone concentration on the ground level (see Section 2.2) is tracked by environmental agencies as an air pollutant and human health threat. For example, the National Ambient Air Quality Standards (NAAQS) based on the Clean Air Act from 1990 require a maximum 8 h average concentration of 7 pphm (parts per hundred million) considering the fourth highest annual value averaged over 3 years since 2015 [24]. European and German environmental agencies also track ozone levels [25]. At high concentrations, ozone is toxic to humans and causes lung inflammation and function decline by damaging the underlying tissue. According to Brück [26], the oxidative potential of ozone also causes the ageing of numerous materials such as rubber. However, despite all the unwanted reactions that ozone is associated with, it is also effectively used to purify water and air.

1.3.3 Ozonolysis Compared to Oxidative Radical Reactions

Compared to free radical auto-oxidation, ozonolysis is faster and has a different reaction mechanism. The macroscale result due to ozone is fast cracking at little tensile strain. Moreover, even in the absence of strain and hence with no cracking, Huntink *et al.* [27] showed that the change due to ozonolysis covers some molecular layers after which the reaction stops. In contrast, a several mm change is observed due to oxidation without cracking, for example by Charrier *et al.* [28]. Bhala [4] also contrasts surface frosting and cracking for ozone attack to hardening or softening throughout the rubber under thermo-oxidative loads. In Section 3.2.1 the depth of change will be compared via infrared spectroscopy measurements.

The chemical reaction of ozone with rubber is an ozonolysis attacking unsaturated double bonds. Criegee [29] analysed ozonolysis with alkenes in solution leading to a cleavage of the double bond in the alkene. A three-step mechanism, shown in Figure 1.3, is outlined, beginning with a 1,3-dipolar electrophilic cycloaddition of ozone to the polymer chain and the formation of a primary ozonide. In the next step, the unstable primary ozonide separates into a carbonyl and a carbonyl oxide, which eventually reconnect to a secondary ozonide such as trioxolane. After the three steps, the secondary ozonide reduces, oxidises, thermolyses, photolises, or hydrolyses when additional reactants e.g. water are available to form products such as ketone derivatives, as shown in [4, 27, 30–32]. Although some conflicting results were obtained, Christian Geletneky [33] indicated that the Criegee mechanism is the only approach that is compatible with their O-NMR spectroscopy results. Furthermore, Zheng *et al.* [34] indicate that even the additional creation of the superoxide, olefin, and hydrogen radicals mentioned by Criegee [29] have potential for gas phase ozonolysis. In IR measurements carried out by Kendall and Mann [35], the researchers found peroxy biradicals after the ozone-ageing of NR. The presence of radicals was also observed by Murphy and Orr [23] when exposing unsaturated rubbers to ozone. The double bonds being scissioned in the backbone of NR in the second step are assumed to initiate crack evolution on a microscopic scale when mechanical strain is present as illustrated by [35–37] and in Figure 1.2.

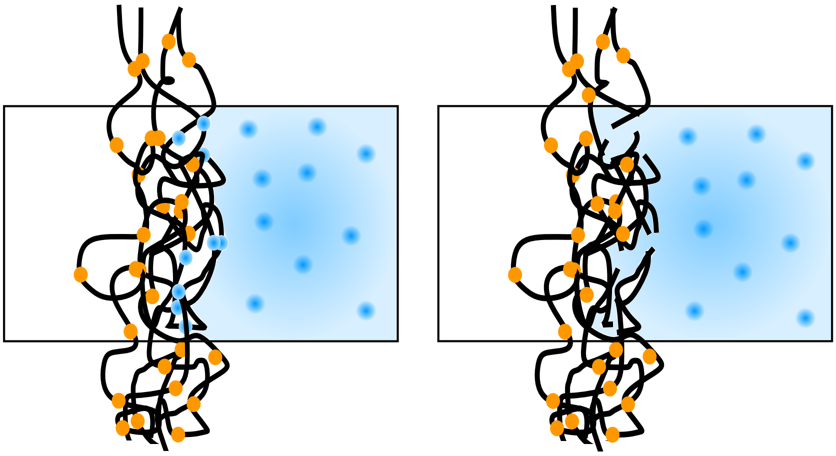

Figure 1.2 Illustration of crack initiation due to a split of the double bonds (orange dot) in the backbone of an entangled NR molecule.

Unlike in ozonolysis, the free radical chain auto-oxidation is initiated by a radical and, as indicated by [5, 38], the reaction scheme is widely accepted for thermo-oxidative ageing. Here, hydrogen is possibly abstracted from the rubber molecule, forming initial radicals. With these, the reaction may propagate via addition to double bonds or hydrogen abstraction until two radicals combine and terminate the chain reaction by deactivating each other. Many branching and

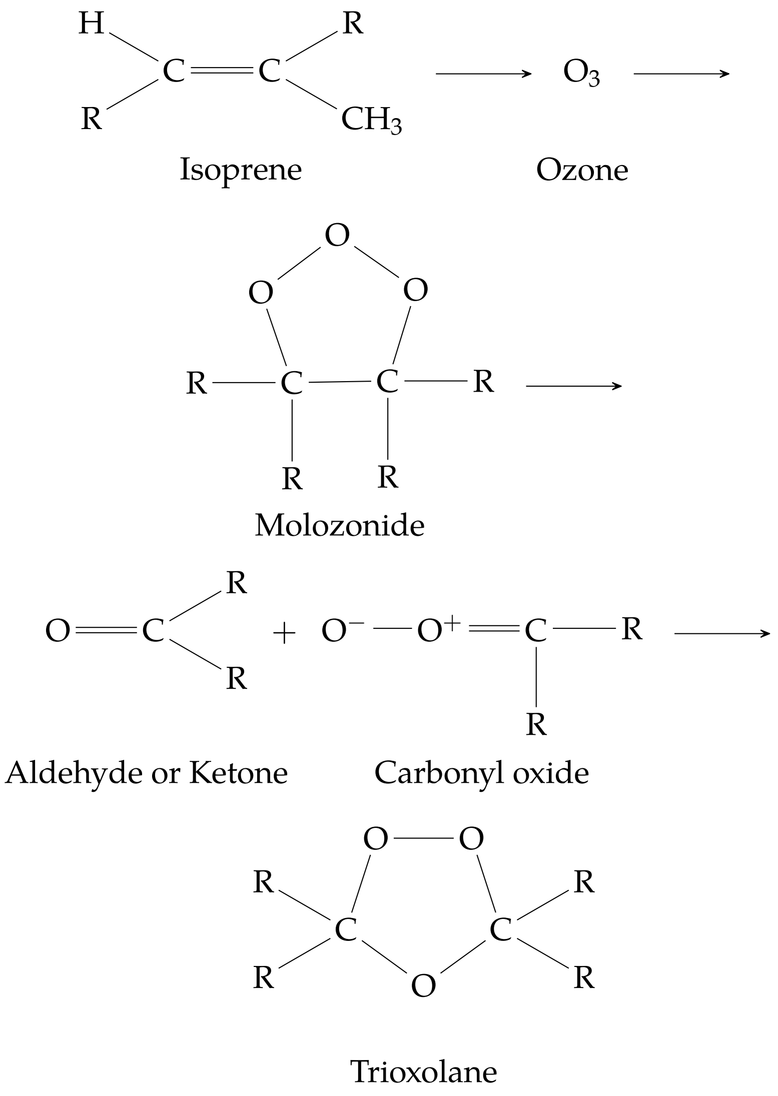

Figure 1.3 Criegee's tree-step mechanism of ozonolysis according to [29].

secondary reactions are possible, as shown by Andrew [13].

1.3.4 Existing Experimental Results

Publications on ozone-induced ageing experiments in NR are comparatively rare in contrast to examinations of other environmental loads, e.g. thermal and thermo-oxidative ageing, for which a comprehensive database of experiments is available in addition to ongoing examinations as shown in [14, 39–44]. The lack of experimental data on ozonolysis in elastomers was recently also highlighted by [30, 34, 36, 45–47].

Several standards provide testing procedures concerning ozone resistance. For instance, standards such as `DIN ISO 1431-1` [48] and `DIN ISO 1431-3` [49] name specific procedures to test elastomeric material against ozone resistance including the methods of ozone detection. The crack appearance and stage are categorized depending on the ozone ageing time under static and dynamic deformation, with dynamic meaning a cyclic loading at 0.5 Hz between 0 and a maximum strain that is equal for static and dynamic loading of 5 – 80 %. The regular ozone concentration is 50 pphm (optionally lower at 25 pphm), both with tolerated differences of ± 5 pphm.

Three procedures are distinguished to document the result after ageing:

1. Description of visible cracks after a defined ageing time
2. Ageing time until first cracks appear
3. The threshold strain necessary for cracks to initiate at all (only static strains)

Another current standard is `ASTM D1149`, while several older standards such as `IEC 60811-2`, `TGL 24418`, and `DIN53509` deal with the ozone exposure of polymers. In summary, the available standards currently focus on the onset of cracks and visual description to compare materials regarding their resistance to ozone but do not provide an objective measure for the degradation caused.

In contrast, experiments found in the literature analyse a wider range of ageing parameters in greater detail and document several ageing results due to ozonolysis. Especially the presence of mechanical strain during ageing is discussed and thus structures the overview provided.

Without strain and at a 50 pphm concentration, no cracks are observed, and a glossy, sticky surface layer evolves, as reported in Kamaruddin and Muhr [47]. The authors suspect a reaction to lower molecular weight products during ozonolysis. Even for ozone levels of only 0.1 pphm, Mott and Roland [50] observes changes in the opacity of polybutadiene. Nevertheless, most experimental investigations are conducted at higher levels of ozone concentration. Based on ozone consumption experiments, Huntink *et al.* [27] observes a changed layer of approximately 10 – 40 molecular layers' thickness. Brück [26] propagates a layer, namely the frosting thickness of 0.5 µm, that hinders further diffusion for the fast reaction of ozone with double bonds in the main polymer chain of unsaturated vulcanizates. Similar behaviour has been observed for thermo-oxidative ageing by Edge *et al.* [39] and Rodrigues *et al.* [37] in deeper layers of approximately 100 µm. By means of PyGC-MS (Pyrolysis–gas chromatography–mass spectrometry), Forrest [21] detected volatile substances after ageing in ozone-contaminated environments in addition to extremely low mechanical strength in a 0.1 mm thick surface layer. In the case of general ageing, the process is said to be observable by DMA measurements via the changing modulus with the ageing state, as indicated by Forrest [21]. However, in cases of ozone ageing – even if strong concentrations such as 500 pphm are applied for 5 days – no change in elongation at break was measured by Spreckels [51]. Similarly, no change in hardness could be detected for the sulphur vulcanized NR used, regardless of whether protecting wax is used or not [51]. Früh *et al.* [45] states that a diffusion-reaction process is dominating the ozone ageing process. The diffusion limitation is expected to be more intense than for thermo-oxidative ageing, since shallower ageing depths occur after ozone ageing. Regarding thermo-oxidative ageing, changes are observed in NR of up to 0.4 mm by Herzig [52], 0.8 mm by Musil [44] in NBR, and even 1 – 5 mm in thermo-oxidatively aged components [28, 53, 54]. The values are similar to a measured ageing depth of 4 mm in an 80 year natural ageing project by Kamaruddin, Le Gac, *et al.* [55] that was exposed to oxygen and light in addition to ozone. In thermo-oxidatively aged samples, Neuhaus [53] used microindentation and Herzig [52] measured a density change in NBR using MicroCT, whereas Colin *et al.* [54] analysed the ageing depth with IR measurements detecting changes in the carbonyl groups and mass uptake. As in the case of UV light and oxygen exposure for several weeks, the approach of detecting carbonyl groups in FT-IR measurements is used to quantify the ageing behaviour of other elastomers [56, 57]. Musil [44] applied the so-called *modulus profiling* approach introduced by Gillen, Clough, *et al.* [58], which was also used by Clough and Gillen [59] for ozone-aged elastomers other than NR. A precise preparation with a focus on the surface roughness is decisive for the result, as indicated by Geels *et al.* [60]. Both Clough and Gillen [59] and Musil [44] measured a gradient in stiffness over the sample cross-section, which is facilitated by cutting the samples, and metallographically polishing and measuring the indentation depth of a tip e.g. a Vickers indentor of a microhardness tester. In addition, a stiffness gradient was assessed by tension tests conducted on layers of previously aged and subsequently split samples by Musil [44]. The change on the surface after ozonolysis of NR was analysed using IR spectra as early as 1956 by Kendall and Mann [35]. Considering ozonized air and ozonized oxygen, he found carbonyl groups after ageing in ketones and peroxy-biradicals. Thereafter, Andries *et al.* [61] observed ozonides and carbonyl compounds on unprotected NR surfaces after ageing. The presence of a strong band at 1736 cm^{-1} is shown by Lemaire *et al.* [31] after ageing for 100 h at 105 ppm. A significant increase in the carbonyl content on the surface is measured by Zheng *et al.* [34] after ageing for only up to 9 hours at 50 pphm and 100 pphm. Additionally, the cross-linking density, tensile strength, and specimen surface change due to ozone ageing, according to Zheng *et al.* [34].

Early experiments conducted by Newton [62] included strain during ageing, and the researchers describe the effects due to ozone loading on rubber separable from other environmental loads. Buckley and Robison [63] claims an accelerated creep behaviour due to ozone loading, while [2, 64, 65] and [66, 67] published a series about an embrittled surface layer and the appearance of cracks correlating to ozone. Andrews and Braden [67] specify the depth of the inextensible layer to about 0.5 µm. In general, they deal with the initiation, growth, and prevention of cracks by different antiozonants including a *p*-phenylenediamine (PPD), which has a similar mode of action to `6PPD`[1] which is still used. The necessity of 3 – 5 % strain for cracks to appear in an orthogonal direction to uniaxial stretching is highlighted and the authors observed a constant crack growth from an initial flaw as soon as a critical stress value is exceeded. Contrary to a threshold stress level, several aspects are not considered to be crucial for the appearance of cracks, including the main polymer, the vulcanisation system, and the antiozonants applied [67]. Albeit, they affect the rate of crack growth, as mentioned by Braden and Gent [2], whereby the number of ozone-related cracks are said to be proportional to the mechanical load level [20, 64]. After investigations without initiated flaws, Lake [68] also found that the growth in crack number and decline in length for rising static strain levels up to 200 %, which is explained by cracks being initiated from smaller flaws in interacting with their neighbours. The minimum strain level for cracks to appear is measured at 4 % for 700 pphm ozone concentration. Lake [68] assessed the crack depth via direct measurement in the cross-section, relaxation considering the cracked cross-sectional area, and the endured cycles in fatigue tests. Concerning the depth, he found a dependence on the strain level, gas flow conditions, and sample size. If the reaction of stretched rubber and ozone is fast, insufficient gas flow may lead to a lower concentration in the vicinity of the sample surface. In the context of severe cracking, Andrews and Braden [66] assessed the evolution from increased surface roughness over fissures to macroscopic cracks for a range of strain levels from 0 to 30 %. Again, a minimum tensile strain is shown to be necessary for crack initiation, which Cataldo [30] correlates to the separation of cleaved double bonds. The necessity of a threshold strain is also observed by Spreckels [51] in static strained samples exposed to ozonised air considering the shoulder part of a tensile bar. When using an NR compound protected by wax, no cracks were observed for ozone concentrations

---

[1] *N*-(1,3-dimethylbutyl)-*N′*-phenyl-p-phenylenediamine

of 50 pphm and below, and even at subsequent exposures at 800 pphm, no cracks evolved. Spreckels [51] concluded that a conditioning phase in which the wax migrates takes place, which protects the surface at low concentrations when the ozone attack is sufficiently slow. This is in accordance with the findings of Lake [68] correlating the necessary amount of antiozonant to the velocity of the ozone attack depending on its concentration.

The crack growth rate was analysed by Lake and Lindley [69] by applying cyclic strain up to 0.8 %. A major reduction in lifetime due to fissures or cracks [66] acting like a notch might occur, as measured by Schieppati, Schrittesser, Tagliabue, *et al.* [70]. Moreover, Flamm *et al.* [71] assumes that ozone cracks might initiate the flaw at which the mechanical crack growth initially occurs. Apart from a crack growth due to pre-existing defects, cracks could also nucleate after a specific number of load cycles [72]. Even in ageing states without mechanical loading and in the absence of cracks, the surface frosting might affect the load cycles concerning the crack nucleation and thus the lifetime endured. In an unaged state, NR has a unique crack growth resistance due to SIC [71, 73, 74]. Below the critical crack growth energy for purely mechanic dynamic loading, a linear relationship between ozone concentration and crack growth rate is observed [20, 65] while above the critical level, the ozone concentration is said to have no influence. Consequently, ozone is the decisive factor for crack growth at lower dynamic mechanical loads [20]. Spreckels [51] analyses slow cyclic loads with a frequency of 1 cycle per hour and a mean tensile strain simultaneously exposed to different ozone concentrations between 1 – 300 pphm. The correlation between the time until the final tear and the ozone concentration is linear in double logarithmic scaling excluding ozone concentrations below 30 pphm with more rapid lifetime increase [51]. In a second test batch, Spreckels [51] applies an amplitude between 0 – 30 mm deformation. Apart from an increase in scatter, a logarithmic linear correlation between ozone concentration and lifetime is observed [51], concordant with the stated beneficial R-value above 0 by Gehling *et al.* [1]. In service life testing, Schmid *et al.* [75] found a highly negative damage prediction regarding the indirectly proportional ozone concentration to lifetime.

1.3.5 Protection by Antiozonants

Several authors proposed that double bonds are susceptible to ozone in polymer chains [3, 5, 30, 76, 77]. An electron is extracted, resulting in scissioned main chains. Without deformation, the mentioned frosting slows down the degradation on the surface [26, 76], although most applications include deformation throughout the lifetime. Lewis [76] lists several protection options against ozone attack:

- No tensile strain
- Choice of resistant rubber type, without dienes
- Blend with more than 25% of resistant rubber
- Surface lamination or modification
- Bulk modification by surface-diffusing antiozonants

The first three options exclude most applications that are under strain and in need of the special characteristics of NR. As a surface lamination is critical for large and or dynamic strains, it is attempted to protect rubber in applications by using surface-diffusing antiozonants. Two antidegradants are commonly applied [4, 27, 30, 68]:

- **6PPD**, which works chemically as a radical scavenger and counteracts oxidation by preferentially reacting with ozone instead of rubber and forming impermeable reaction products. Andries *et al.* [61] enhance the scavenger and protection layer theory in FT-IR tests that show a faster spectral change compared to the reaction of ozone with unprotected NR which is equal to spectra of ozonised PPD.
- **Paraffin wax**, forming a physically protecting, non-reactive barrier by migration to the surface.

Apart from wax, a non-reactive barrier can also be applied on the surface with different materials, for example, by introducing polymethylmethacrylate (PMMA) cover layers, as described by Früh *et al.* [45], silicone grease as indicated by Braden and Gent [2] and Lake [68], or other coatings [78]. All non-reactive barriers work by limiting or stopping the diffusion of ozone to the underlying material. The physically protecting layers are only stretchable within limits [68], and cracks open in response to alternating mechanical strain. In addition, they might be rubbed off the surface due to friction or wear. A different approach includes blending with ozone-resistant polymers [76] which changes the elastomers' characteristics. Like wax, `6PPD` migrates to the location of consumption, which usually is the surface. In general, the migration is enabled by the low molecular weight of both antidegradants, as Datta *et al.* [79] shows. Both antidegradants display beneficial effects concerning protection, although static strain limits the effect of PPDs and both antiozonants fail to prevent cracking under cyclic loading [30, 76, 80]. The degree of efficiency closely correlates with the migration characteristics and is conditional on the temperature, degree of cross-linking, and solubility, as described by Bhala [4] and Ignatz-Hoover *et al.* [81]. Despite the limited effect of PPDs for static and dynamic strain, and even though they have a strong staining effect, Cataldo [36] found them to provide the best protection at present. In addition, due to being radical scavengers, they protect against thermo-oxidative ageing, as shown by Bhala [4].

1.3.6 Damage Parameters and Simulation

In general, the damage due to ageing can be classified to the change in material characteristics as a change in stiffness, and macroscopic damage as cracks [82]. Ozone ageing triggers both types of damage, whereby cracks only appear in samples aged under strain but change is measurable on the surface without cracks, as reviewed in Section 1.3.4. The changes in material characteristics are superficial in ozone-aged NR, and cracks are often used to quantify the damage [47, 50, 62, 66, 68, 83]. As the artificial ageing process in laboratories is limited in time, acceleration is necessary and consequently extrapolation to regions that cannot directly be measured. Therefore, based on the measured data, a suitable mathematical description of the ageing process is usually derived. Concerning the fitting of a damage evolution, the accelerating variable and the quantified damage parameters are crucial.

Acceleration Variable

Numerous ageing processes can be accelerated using elevated temperatures. Specifically, the Arrhenius law is widely applied to model environmental ageing processes sped up by higher temperatures [53, 84]. In the case of thermo-oxidative ageing, the reaction rate is often assumed to solely be governed by elementary processes [85] and then connected to the change measured in material characteristics. Consequently, a logarithmic linear relation between ageing time and the temperature maps the status of a material characteristic [52, 86]. In the case of Herzig [52], the resulting reaction rate at a thermo-oxidative ageing front contains two Arrhenius laws in temperature-dependent material characteristics: one in the solubility and the second in the rate of change in cross-link density. However, even though the origin is a temperature dependence, the Arrhenius equation might be adapted for other acceleration parameters, and Larsen and Furst [87] successfully used the exponential dependence for a time-cure-superposition instead of a time-temperature-superposition. Furthermore, in a non-elementary process due to competing ageing mechanisms, Celina, Gillen, and Assink [88] use the sum of Arrhenius rates to model a change in the dominant degradation mechanisms resulting in a curved extrapolation.

Concerning UV light exposure, a time equivalent for real outdoor ageing is correlated to the power of the laboratory lamp compared to the irradation in nature [89].

Another approach is to relate the physical ageing phenomenon to the concentration of reactants determining the rate of underlying chemical reactions. Dakin [90] abstractly relates tensile strength reduction to scissions in molecule chains of cellulose. Assuming a monomolecular first-order reaction, the concentration and/or physical properties decrease exponentially with the reaction time. He clarifies the importance of the monomolecular assumption considering that most ageing processes are more complex. Especially for strong diffusion-limited oxidation (DLO) effects, Gillen, Bernstein, *et al.* [91] indicate that no monomolecular reaction is suitable to model the thermo-oxidative ageing process. In ozone ageing, diffusion limitation completely blocks ageing in the core [27, 92]. However, Murphy and Orr [23] state that bond rupture can be modelled by a first-order kinetic correlation leading to macroscopic failure.

The previously described Arrhenius law and monomolecular reaction process are usually used to model changes in material characteristics. In cases where strain is present during ozone ageing, cracks appear as macroscopic damage.

Macroscopic Damage

Conditions for Crack Nucleation The time t until cracks appear in strained samples due to ozone loading is described by several authors [93–95] to be indirectly proportional to the concentration c, expressed as

$$t = \frac{\mathrm{B}}{c^{\mathrm{n}}}, \tag{1.1}$$

with B and n being material parameters and the latter set to $\mathrm{n} = 1$ for NR according to Zuev and Pradvednikova [93]. Others use fracture energy equations to explain earlier crack formation under ageing conditions [50].

Crack Growth Buckley and Robison [63] state the crack growth is linearly proportional to the square of ozone concentration for a tested butyl rubber compound. As tests are conducted under high concentrations, extrapolation to realistic concentrations as found in the atmosphere is seen as critical. Considering an initial crack, the evolution of crack depth h_c with time t is stated to rise at the constant rate of α_{ozone}, depending on the ozone concentration [2, 51].

$$\frac{dh_c}{dt} = \alpha_{\text{ozone}} \tag{1.2}$$

Concerning dynamic loading, Gent [20] recommends obtaining the crack growth per applied cycle N by multiplying the quotient of time under stress in each cycle τ, divided by the frequency ν with the the ozone-dependent constant crack growth velocity α_{ozone}, as shown by [96]:

$$\frac{dh_c}{dN} = \frac{\tau}{\nu} \cdot \alpha_{\text{ozone}} \tag{1.3}$$

Ehrhardt [97] employs an empirical logarithmic approach to relate the crack states c_1 and c_2 of different ozone concentrations to their ageing times t_{i}:

$$\log\left(\frac{t_1}{t_2}\right) = k(c_1 - c_2) \tag{1.4}$$

Correlating Damage to Realistic Loading Conditions

Laboratory tests must be conducted in an accelerated manner, and thus a relation to realistic ageing loads is necessary. In the case of a constant loading under real conditions, Spreckels [51] uses Eq. (1.1) to relate the ageing time and ozone concentration, leading to identical ozone cracks. He thus obtains a simple indirect proportional correlation between the ageing time and ozone concentration. Regarding elongation at break, the measurements were in good agreement above 75 pphm in case of dynamic loading above 50 pphm whereby both are strongly above expected ground-level ozone concentrations. Low concentration tests at 3 – 5 pphm are conducted by Lewis [76] but without relation to accelerated ageing conditions. The application of ozone concentration populations for different seasons such as winter and summer is recommended, in addition to the use of an average seasonal concentration to calculate equivalent laboratory conditions [51].

There are a lot of people who will give money or materials,
but very few who will give time and affection.

— By: Daniel Keyes *Flowers for Algernon*

2

Artificial Ageing and Sample Preparation

Contents

2.1 Material Compounds

NR has an extraordinary high content of 99.5 % `cis-1-4-polyisoprene`, shown in Figure 2.1, combined with a high molecular weight of $1 \times 10^3\,\mathrm{kg\,mol^{-1}}$ [98]. Additionally, non-rubber components are responsible for its unique material characteristics, which causes all attempts concerning full substitutes to fail [99].

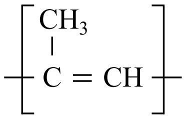

$$\left[\begin{array}{l}\mathrm{CH_3}\\ | \\ \mathrm{C = CH}\end{array}\right]$$

Figure 2.1 Monomer structure.

In general, caoutchouc needs to be vulcanized to generate the commonly known elastic material characteristics of rubber, whereby different chemical processes can be applied depending on the polymer type. Regarding NR and styrene-butadiene rubber, sulphur vulcanisation is applicable. Some of the hydrogen atoms adjacent to the carbon-carbon double bonds (see Figure 2.1) are replaced by sulphur linkages. Thus, different molecular chains of the NR are connected by sulphur links of variable length by different numbers of sulphur atoms in a row. The latter influences the rubber's characteristics.

Table 2.1 Mixture of the NR compounds under investigation.

Component	[phr][1]		Compound
NR CV 60	100	Base Polymer	1, 2, 3
Carbon Black N330	40	Filler	
Zinc Oxide	3	Vulcanizing Agents	
Sulphur	2		
Stearic Acid	1		
TBBS[2]	1		
6PPD	3	Antiozonant	1, 2
Paraffin Wax	3		1

The major compound investigated in the present study was conventionally manufactured by *The Centre of Polymer Systems* (CPS), Zlin. The mixing ratios are listed in Table 2.1. Supplied by *Thuan Loi Rubber Company Limited, SVR CV 60*, NR of constant Mooney viscosity 60 is the main ingredient at 100 phr. Working as stabilisation against UV light [21], in this compound, carbon black is applied to strengthen the rubber and improve its physical properties. With 40 phr, *High Abrasion Furnace* carbon black *N330* from *Cabot Corporation* has the second-largest ratio in the compound and is at the optimum regarding fatigue strength accoring to Gehling *et al.* [1]. Its particle size should range from 26 nm up to 30 nm and

---

[1] parts per hundred rubber
[2] *N*-tert-Butyl-2-benzothiazolesulfenamide

improve the heat conduction compared to unfilled NR. Four vulcanizing agents are applied: inorganic zinc oxide provided by *SlovZink* activates the vulcanisation process, as does the organic stearic acid by *Sigma Aldrich* in addition to functioning as a softener and dispersant. Third, is sulphur by *Eastman Chemical Company* and last is the accelerator TBBS by *Behn Meyer Europe GmbH, Perkacit*.

Two common antidegradants are applied: chemically-acting 6PPD, provided by *Behn Meyer Europe GmbH, BEMOX*, and physically protecting paraffin wax, provided by *Werba-chem GmbH*. As introduced in Section 1.3, in industry, 6PPD is mostly applied and, in some applications, this is used together with wax. Compound 1 (`C1`) contains 3 phr of each and compound 2 (`C2`) only 6PPD whereas compound 3 (`C3`) is without antiozonants as listed in Table 2.1. Via a special molecular structure, 6PPD works against thermo-oxidative and ozone-induced ageing. It can both react radically and electrophilically, which makes it a favoured antidegradant in industry.

In the fatigue tests conducted, a different rubber compound is applied, named compound 4 (`C4`). The samples are manufactured by *BOGE Rubber & Plastics* using a blend consisting of 90 % NR and 10 % butadiene rubber (BR). Chemical and physical antidegradants are present in the compound reaching a Shore A hardness of 49 at a carbon black content of 20 %. In the other three compounds, the vulcanisation system is sulphur-based.

2.2 Ground-Level Ozone

Most industrial components face ground-level ozone concentration, some higher ones in production facilities. Consequently, the present ground-level concentration is discussed regarding its creation, measurements in environmental stations, and future trends to expect.

2.2.1 Creation

In general, ozone concentrations measured on the ground level are the result of an equilibrium state, illustrated in Figure 2.2. Molecular oxygen is split by UV radiation or electric discharge to oxygen atoms which subsequently react with each other to form ozone [23]. The necessary energy is mainly available in the stratosphere, showing some downward flux to the troposphere [100]. However, in situ photochemistry and air pollution with substances contributing to ozone formation by far exceed the influence of downward flux [100]. At ground level in the troposphere, volatile organic compounds (VOCs), carbon dioxides, or nitric oxide support ozone production by donation of oxygen atoms at less energy-rich radiation e.g. electric devices or long-waved UV light. However, nitric oxide and carbon monoxide reduce ozone to oxygen again. Since ozone is unstable, it may also decompose thermally and in response to photolysis or electron impact, whereby the availability of precursors shifts the resulting ozone concentration.

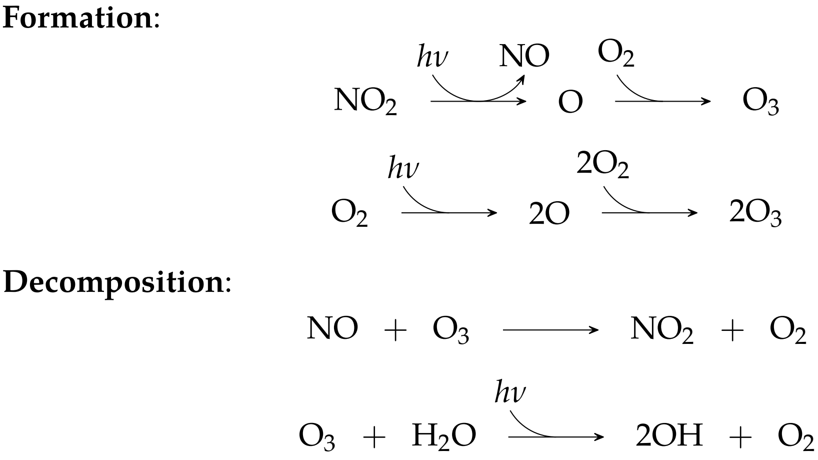

Formation:

$$NO_2 \xrightarrow{h\nu \,\searrow\; \nearrow\, NO} O \xrightarrow{O_2\,\searrow} O_3$$

$$O_2 \xrightarrow{h\nu\,\searrow} 2O \xrightarrow{2O_2\,\searrow} 2O_3$$

Decomposition:

$$NO + O_3 \longrightarrow NO_2 + O_2$$

$$O_3 + H_2O \xrightarrow{h\nu\,\searrow} 2OH + O_2$$

Figure 2.2 Reactions for forming and decomposing ozone creating an equilibrium state on the ground level.

In this context, De *et al.* [18] found a concentration of 2 – 5 pphm in unpolluted environments, whereas pollution with peroxy radicals from hydrocarbon emissions transform nitric oxide to nitrogen dioxide and thus shift the steady state to higher ozone levels up to 50 pphm. The temperature range in the air at the ground level has no strong effect on ozone formation, which is in contrast to the UV radiation delivering the energy necessary to split oxygen and subsequently create ozone.

2.2.2 Measurements

Ozone concentrations on the ground level are measured by a dense net of environmental surveillance stations. In Europe, like in the USA, the measured data is predominantly available as 1- and 8-hour-average concentrations and the numbers of limits exceeded per year [25, 101]. As explained in Section 2.2.1, the creation of ozone is strongly dependent on the availability of reactants such as nitrogen dioxide [102] and VOCs [30] which both rise in concentration with increased air pollution. This causes local differences [103] leading to accumulations which stationary meteorological stations cannot capture, clarified by their operators such as [25, 104, 105]. Besides high concentrations due to geographic air pollution and fluctuating energy sources [30, 102, 103], periods of higher ozone exposure might occur in industrial applications due to local pollution and energy radiation. The differences between areas that are close to traffic, rural areas and industrial areas are noted by the German environmental agency [25] and the exceeding of threshold values clearly mark a difference in location. Lake and Mente [106] even highlight possible ozone concentrations 10 times higher in air-polluted areas compared to clean environments. In addition, marked differences are observed between marine and continental areas, as reported by Crutzen *et al.* [100] and Salisbury *et al.* [107]. The latter observed a background level of 3 – 4 pphm at night, referring to measurements of the Mace Head Atmospheric Research Station.

To contextualize the concentrations of ozone used to artificially age samples, some values published by the German environmental agency [25] are highlighted, whereby ground-level ozone concentrations rose to about 350 $\mu g\,m^{-3}$ resp. 16.4 pphm [1] in the maximum 1-hour-average, measured in August 2023. Both measurements usually reach a daily maximum of around 100 $\mu g\,m^{-3}$ resp. 4.7 pphm. In 2019, the 8-hour-average climbed up to 210 $\mu g\,m^{-3}$, which is equal to approximately 9.8 pphm. The number of days per year with an 8-hour-average exceeding 5.6 pphm ozone in the same station is below 20 in Germany [25], whereas in Europe [108], it is about 40 days. The long-term European target is 5.6 pphm, the information threshold 8.4 pphm, and the alarm threshold 11.7 pphm. However, these levels are rarely achieved.

In this context, it is important to note that even a few pphm of ozone cause severe damage, as shown by Datta *et al.* [79], as does exposure to a high concentration within a shorter time scale. The measurements show that the usual daily range seems to fluctuate around 3 – 5 pphm with peaks of about 15 pphm being reached on summer afternoons and nights.

2.2.3 Trend

The ground-level ozone concentrations are not constant over decades, as precursors from emissions change [109]. In Europe, the emissions of NO_x and NMVOC peaked around 1985 but have been decreasing since then. Consequently, the peak concentrations in summer day-time decreased [110] although during the night-time and all day in winter, increasing ozone concentrations are measured,

---

[1] The measurements are given in $\mu g\,m^{-3}$ referring to the barometric pressure at 20 °C. The unit pphm (volume fraction of parts per hundred million) used in laboratory devices is pressure-independent. The factor between pphm and $\mu g\,m^{-3}$ for 0 °C at 1012 hPa is 21.4.

more frequently exceeding 3.5 pphm as the 8-h mean value [109].

2.3 Selected Range of Ageing Parameters

Artificial ageing needs to reduce ageing times compared to ordinary lifetimes of components to simulate the degradation of NR in feasible time scales in a laboratory setting [111]. In `DIN ISO 1431-1` [48], the parameters named include the ozone concentration, temperature, relative humidity, and strain levels. In addition to the following parameters that are described in detail, further requirements for the ozone ageing chamber and the sample geometry are listed. An overview of the ageing parameters that were selected for this thesis is shown in Figure 2.10.

2.3.1 Temperature

Two common adjustment parameters that can be employed to accelerate chemical processes include the elevation of temperature or the concentration of a deficient reaction partner.

A temperature increase to above 60 °C is the method applied in many thermal and thermo-oxidative research projects such as [14, 44, 52, 112–115]. Only a few researchers, such as Broudin *et al.* [43] apply temperatures below 60 °C. In such cases, the ageing times are longer than 21 days, and obtain a prominent change in properties for even longer ageing times above 100 days.

Nevertheless, the stabilization of ozone concentrations is contingent upon a temperature threshold of approximately 60 °C, as evidenced by Tamm [116]. According to [51], at higher temperature an enhanced decay of ozone goes beyond the production rates. In addition, unintended chemical or physical reactions might take place, thereby changing the ozone degradation from that observed at the application temperature [40]. Bhala [4] even states that there is no dependence on temperature for ozonation or cure.

At a temperature of 40 °C, thermo-oxidative ageing occurs but should not be strongly accelerated. In Figure 2.3, the stress-strain curve is compared for pristine versus thermo-oxidatively aged samples without antidegradants after 111 h at 40 °C without deformation during ageing. The findings indicate that there is a stiffness increase of a maximum of 11 % regarding the average of three samples tested, whereby the range of measurements strongly overlaps. Even with high static deformation during ageing, the surface displays only slight flaws compared to samples being exposed to ozone, as addressed in the following, see Figures 3.34 and 3.39.

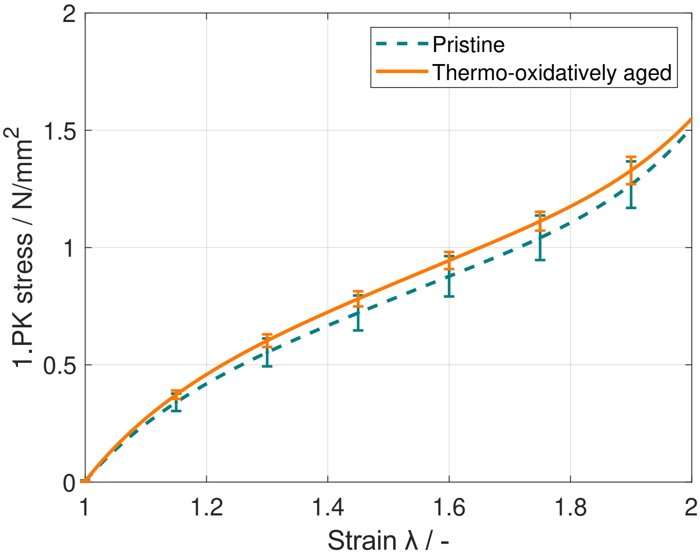

Figure 2.3 No significant increase in stiffness after 40 °C for 111 h for `C3`.

Thus, a temperature of 40 °C with an accuracy of ±2 °C is chosen, as proposed in `DIN ISO 1431-1` [48]. Concerning the experiments conducted, it is considered to be suitable for the examination of ozone-induced ageing—mostly excluding thermal and thermo-oxidative ageing effects—although temperature might affect the migration behaviour of the antiozonants. However, the influence is considered negligible since 40 °C is covered by the service temperature of paraffin wax and the content of 6PPD did not change in the surface layer when examined using a gas chromatography mass spectrometry analysis.

Consequently, in order to accelerate the chemical processes associated with ozone ageing, the second potential method of increasing the concentration of the reaction partner ozone is employed.

2.3.2 Ozone Level

As indicated by Kamaruddin and Muhr [47], the ozone ageing of NR should be adequately reproduced artificially on shorter time scales in a laboratory setting. Ozone generators are applied to increase the concentration, and they require a fast measurement response to regulate the generator to obtain the desired concentration. Meteorological stations publish 1- to 8-hour averages using slower indirect measurement methods [18, 103]. Most laboratory devices use the corona discharge method for ozone production and UV absorption spectroscopy for the measurement as ozone blocks some wavelengths in the range of UV light, as the device by *Anseros® Klaus Nonnenmacher GmbH*. Direct and indirect measurement systems have different degrees of precision, with the faster UV absorption spectroscopy being less accurate. The limits of detection for direct methods range from 2.9 – 3.6 pphm, as reviewed by Silveira Petruci *et al.* [103]. A possible deviation of ± 5 pphm was found by *Anseros® Klaus Nonnenmacher GmbH* for its ozone climate simulator, in accordance with the requirements of `DIN ISO 1431-1` [48]. Next to inhouse artificial ageing with the ozone climate simulator *SIM7500-TH* by *Anseros® Klaus Nonnenmacher GmbH* series `Z` (see Figure 2.10) was externally aged at the *Centre of Polymer Systems of the Tomas Bata University Zlin* with a device by *Gibitre® Instruments srl.*

The concentrations that were applied in the study begin at 10 pphm for series `Z` and 25 pphm for series `U` and `D`. The minimum value and difference comparing series `Z` originates in the different climate chambers used: series `Z` was externally aged at the *Centre of Polymer Systems of the Tomas Bata University Zlin* with a device by *Gibitre® Instruments srl.* whereas all other series are aged by the author with the ozone climate simulator *SIM7500-TH* by *Anseros® Klaus Nonnenmacher GmbH*. In `DIN ISO 1431-1` [48], 25 or 50 pphm are named as standard ozone concentrations, with the lower limit of 25 pphm being approximately double the maximal measured ground-level ozone concentrations. To avoid changes in the chemical process of ozone attack, no more than 75 pphm are applied in this study. Between the lower and upper limits, a logarithmic distribution was chosen as ageing processes tend to run on a logarithmic timescale [53, 91].

2.3.3 Humidity, Air Exchange Rate, Fan

Humidity's influence on gaseous ozone degrading rubber was observed by Buckley and Robison [63] without quantitative analysis. Iwase *et al.* [46] found intensified ageing above a level of 50 % relative humidity as water vapour reacts with ozone into hydroxyl radicals attacking rubber in a similar way to ozonised water. In general, humidity offers more possibilities for the subsequent reaction after the scission of the double bonds as explained in Section 1.3.3. In addition, `DIN ISO 1431-1` [48] requires less than 65 % relative humidity, and 50 % relative humidity is chosen as the artificial ageing parameter.

According to [48], the purified air must be ozonised either by a UV lamp or a corona discharge method. Afterwards, the exchange needs to be fast enough to ensure a constant ambient concentration in the proximity of the sample. Concerning all tests on the device *SIM7500-TH* by *Anseros® Klaus Nonnenmacher GmbH*, the fan frequency was set to 30 Hz, resulting in an air speed in the ozone chamber of 370 mm s^{-1} and the airflow being measured to 0.181 m^3 s^{-1} in the 0.3 m^3 large chamber. This is very high compared to the proposed 12 – 16 mm s^{-1} in the standard, although it is claimed that up to 600 mm s^{-1} might be necessary to ensure a sufficient supply of ozone to guarantee ambient conditions. In order to be able to make comparisons, the gas flow is set constant for all measurements except for the first samples aged in the ozone chamber of *Gibitre® Instruments srl.* with undocumented gas flow. In addition, all samples are clamped in a rotating carousel that moves the samples through the chamber in case of an inhomogeneous distribution of ozone concentration.

2.3.4 Deformation During Ageing

Apart from the main parameters of influence concerning the ageing concentration and ageing time, deformation during ageing strongly influences crack development and evolution. Without tensile strain being applied during the ageing process, no cracks were measurable. As stated in Section 1.3.4, `DIN ISO 1431-1` [48] describes one classification of ozone resistance using the threshold strain for crack appearance. Many other authors, such as [64, 76, 106] confirm a threshold of about 2 % strain for the onset of cracks. When comparing a pristine to a strongly ozone-aged sample without deformation during ageing, little difference is observed in the stress-strain curve depicted in Figure 2.4.

Different strain levels are chosen for the artificial ageing, ranging from 0 – 80 % of static tensile strain and a cyclic deformation of (12.5 ± 5.0) %, (20 ± 20) % and (30 ± 10) % applied during artificial ageing. As numerous applications are prestressed, a pulse around a tensile load is additionally considered. Regarding the static strains, `DIN ISO 1431-1` [48] proposes between 5 – 80 %, however the dynamic strain in the standard is recommended, different to that applied here, at maximal 10 % strain and always between 0 % and maximal strain.

2.3.5 Ageing Time

The ageing times standardised in `DIN ISO 1431-1` [48] range from 2 – 96 h, independently of the mechanical strain applied. Regarding the dynamic strains, a frequency of 0.5 Hz is selected. In this project, the ageing times mainly begin at 4 h, considering a 30 min set-up and cool-down phase in the ozone chamber. The onset of cracking is found after approximately 3 h at 50 pphm by Kamaruddin and

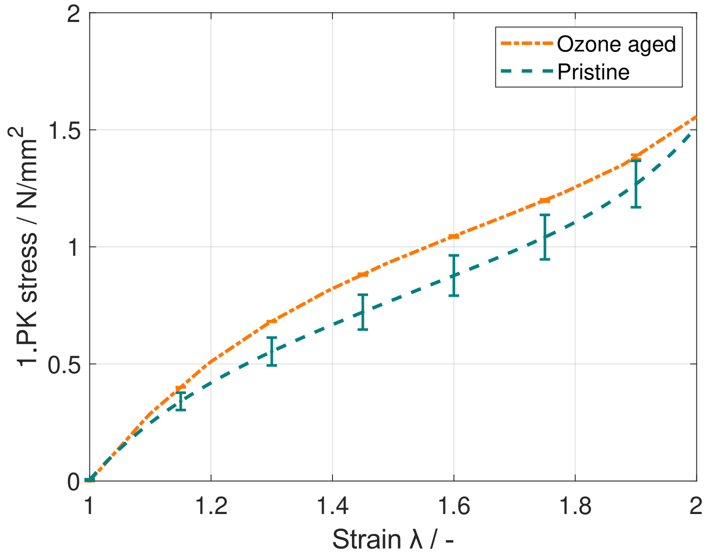

Figure 2.4 Stress-strain curve for a pristine vs an aged sample at 75 pphm for 111 h without strain.

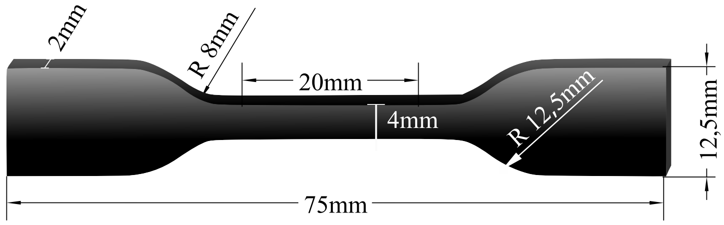

Figure 2.5 Standard S2 tension test sample.

Muhr [47]. Concerning lower ozone concentrations such as 1 – 3 pphm, ageing times of a few days are recommended by Lewis [76] to measure cracking. Times of up to 500 h are tested to examine the maximal degradation for the relatively low ozone level of 25 pphm.

2.4 Sample Fabrication

2.4.1 Vulcanisation Moulds

Standard bone-shaped tensile bars `S2` and `S3`, see Figure 2.5, according to `DIN 53504` [117], plates of 12.5 x 12.5 cm and hourglass-shaped buffer samples, see Figure 2.6, are vulcanised. After the artificial ageing process, they are further prepared for the experiments described in the following.

Buffers for the fatigue tests are vulcanised to metal plates including screws

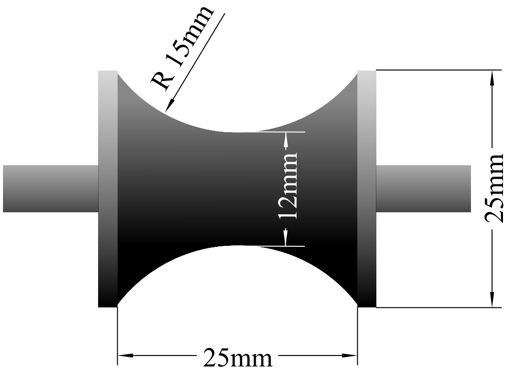

Figure 2.6 Hourglass geometry of buffer sample used in series `F` vulcanised to steel adapters.

to connect samples with clamps in the ozone chamber and load the samples cyclically during the fatigue test, as depicted in Figure 2.6.

The thickness of the tension bars should be 1 mm (`S3`) resp. 2 mm (`S2`), in addition to 4 mm for the plates. The true thickness varies after being vulcanised: 1 mm samples vary between 0.94 and 1.61 mm, while 2 mm samples vary between 1.87 and 2.31 mm, measured for bars before uniaxial tension tests, as shown in Figure 2.13. The plates are used to obtain a one-dimensional ageing gradient and punch bone-shaped or bar-shaped samples for further experiments described in Section 2.6.

2.4.2 Splitting Layers

NR sheets are split to obtain samples of different desired thicknesses or to obtain layers of the cross-section after the ageing process. This was achieved by using an *FBS AB320* precision band knife splitting machine, manufactured by *Fortuna GmbH*. To avoid heating of the sample and friction between the knife and sample, a lubricant containing water (3000 mL), isopropyl (100 mL), and a drop of liquid soap is used. The sample is grabbed by adjustable distanced rollers transporting it in a controlled manner through the running blade. Even with a precision of 0.05 mm on the upper roller and 0.01 mm on the lower one, some compression on the rubber is necessary to ensure a smooth movement forward. The blade leaves traces on the surface of the rubber sheets, as shown in Figure 2.7, which is excluded from the requirements for normative sample geometries [49].

Therefore, the surface roughness parameters are analysed on a *VK-X210* Laser Scanning Microscope (LSM) by *Keyence*. Since most parameters are dependent on

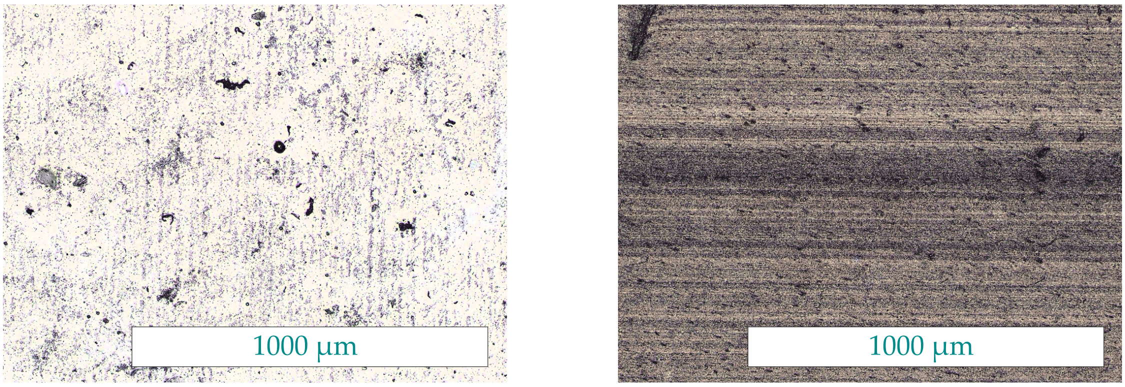

(**a**) Vulcanised. (**b**) Split by band knife.

Figure 2.7 Surface picture of unaged samples.

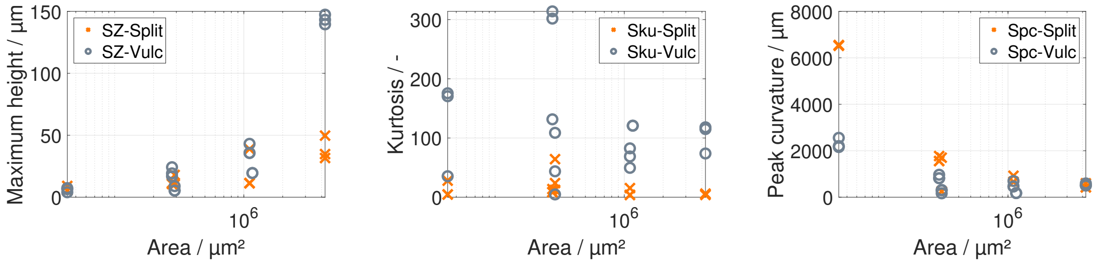

(**a**) Maximum height. (**b**) Kurtosis. (**c**) Arithmetic mean peak curvature.

Figure 2.8 Surface roughness parameters analysed on a *VK-X210* LSM by *Keyence*.

the area taken into account, different magnification factors such as 5, 10, 20, and 50 are considered. The maximum height, defined as the maximal valley-to-peak difference increases with the scale, as depicted in Figure 2.8a. However, in small areas, there is no difference between the split and vulcanised surface. The height difference in areas above 10^6 µm might be due to larger inhomogeneities in the surface than the traces from splitting. Looking at the kurtosis of the roughness profile in Figure 2.8b, the vulcanised surface delivers higher values equal to a more spiked height distribution. In concordance, for the arithmetic mean peak curvature, see Figure 2.8c, more rounded shapes, meaning higher values, are obtained for the split surface and more pointed ones for the vulcanised surface. In conclusion, the vulcanised surface is more uneven than the split surface.

Nevertheless, the texture direction clearly shows the orientation of the knife's traces, which act as flaws in the sample when strained. Thus, the traces need to be oriented in parallel to the strain direction during ageing to obtain an equivalent crack picture as observed in samples with vulcanised surfaces (see Figure 2.9).

Optimally, the precision of the resulting sheet thickness is ±15 µm, while the

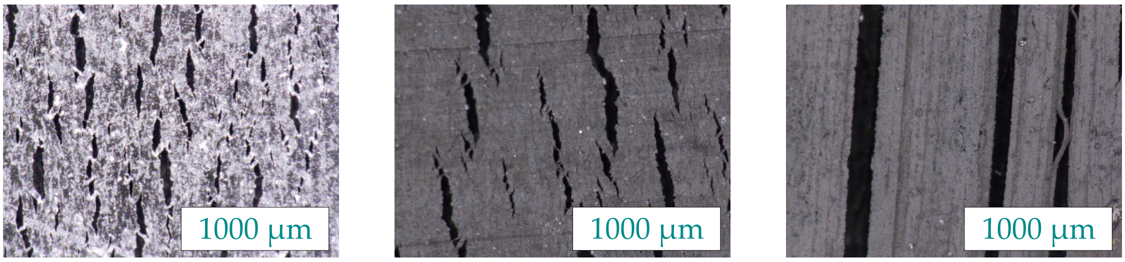

(**a**) Cracks on vulcanised surface.

(**b**) Cracks on split surface with traces parallel to the loading direction.

(**c**) Cracks on split surface with traces lateral to the loading direction.

Figure 2.9 Optical change in the surface after the artificial ageing process.

minimum thickness achieved reaches about 150 µm. The split specimens often have a bulge within the precision at the last edge being transported through the knife, especially if the edge at the end underwent an ageing process.

All samples were stored vacuum-packed in a fridge or freezer to avoid, or at least slow, the ageing processes in the laboratory environment due to light, temperature, or oxygen exposure. The raw material of all samples was manufactured off-site and was transported in plastic bags without cooling. It was only vacuumed and stored upon arrival.

2.5 Ageing Series

Different ageing series were conducted, named `Z`, `U`, `D`, `C` and `F` depicted in Figure 2.10. Given the availability of the ozone climate simulators, the first series `Z` was aged with an ozone chamber manufactured by *Gibitre® Instruments srl.* in the Czech Republic by the *Centre of Polymer Systems of the Tomas Bata University Zlin*. Regarding all other series `U`-`F`, the *SIM7500-TH* device developed by *Anseros® Klaus Nonnenmacher GmbH* was used.

Regarding the geometry of the artificially-aged samples, series `Z` is vulcanised as a bone-shaped specimen and then aged. Hence, its edges are in a two-dimensional ageing state. In contrast, series `U`, `D`, and `C` have one-dimensional ageing states as their samples were punched from plates after ageing. A special series `F` of ageing was conducted on hourglass-shaped buffers as depicted in Figure 2.6. Section 2.4 describes the vulcanised specimen geometries in more detail.

The applied concentrations of ozone start at 10 pphm for series `Z` resp. 25 pphm for the other series, depending on the device used. The maximal concentration applied is 75 pphm ozone in both cases, except for some complementing experiments in series `F`. Besides the ozone concentrations, the ageing times of the series are also distributed logarithmically up to 111 h, including some individual measurements up to 500 h to enhance the findings. The logarithmic distribution is chosen for a logarithmically linear relationship between the ageing time and material characteristic, as is frequently reported, e.g. by Ehrenstein and Pongratz [86]. In contrast to all other series, in series `Z` the ageing times are doubled up to 96 h like those in the standard `DIN ISO 1431-1` [48].

In the first series `Z`, all samples are aged at 20 % static deformation. The second series `U` includes more strain levels up to 40 % deformation, as does series `D` with static strain states only. Series `D` aims to quantify the onset of cracking and to relate the strain level to the cracks observed including strain levels 2, 6, 10 % and, in addition, 80 % strain.

The fact that cyclic deformation is frequently present in components is applied in series `C` on bar-shaped samples at the levels of (12.5 ± 5.0), (20 ± 20), and (30 ± 10) to analyse the impact on crack growth. Large deformations are considered to achieve realistic loading states as described in fatigue experiments [71, 73].

Additionally, in series `F`, the fatigue behaviour is analysed for buffer samples of `C4` after static and cyclic loading during ageing to analyse the lifetime change after ozone exposure.

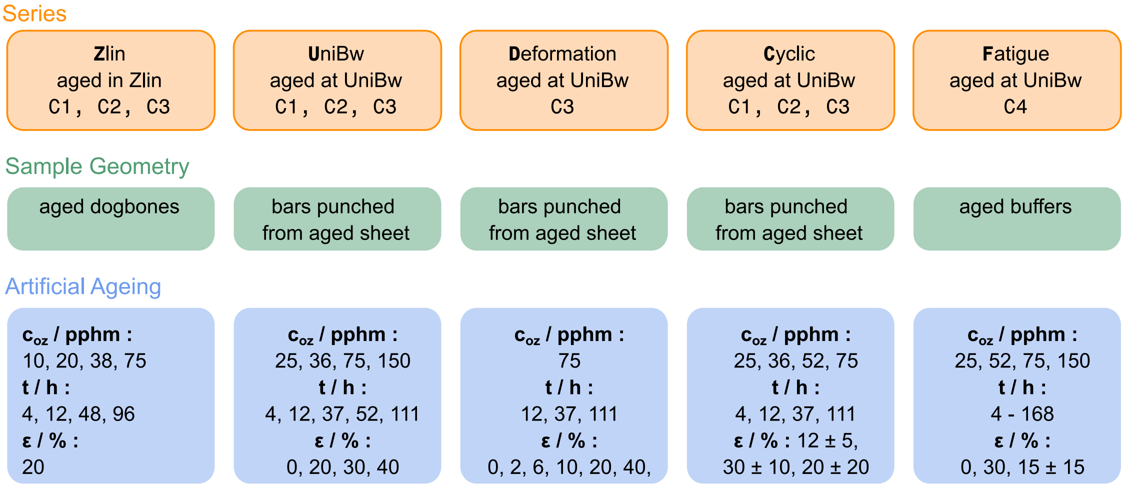

Series	**Z**lin aged in Zlin `C1, C2, C3`	**U**niBw aged at UniBw `C1, C2, C3`	**D**eformation aged at UniBw `C3`	**C**yclic aged at UniBw `C1, C2, C3`	**F**atigue aged at UniBw `C4`
Sample Geometry	aged dogbones	bars punched from aged sheet	bars punched from aged sheet	bars punched from aged sheet	aged buffers
Artificial Ageing	**c_{oz} / pphm :** 10, 20, 38, 75 **t / h :** 4, 12, 48, 96 **ε / % :** 20	**c_{oz} / pphm :** 25, 36, 75, 150 **t / h :** 4, 12, 37, 52, 111 **ε / % :** 0, 20, 30, 40	**c_{oz} / pphm :** 75 **t / h :** 12, 37, 111 **ε / % :** 0, 2, 6, 10, 20, 40,	**c_{oz} / pphm :** 25, 36, 52, 75 **t / h :** 4, 12, 37, 111 **ε / % :** 12 ± 5, 30 ± 10, 20 ± 20	**c_{oz} / pphm :** 25, 52, 75, 150 **t / h :** 4 - 168 **ε / % :** 0, 30, 15 ± 15

Figure 2.10 Overview of ageing series.

The clamping system is important in cases of almost incompressible rubber to obtain the desired value of strain. Rectangular plates are frequently used to clamp the sample endings, thereby leaving a clear span h_0 in between, as illustrated in Figure 2.11a. In case of rubbers, the Poisson ratio is close to 0.5 and the contraction during elongation may lead to slippage. Hence, to avoid slippage, high pressures are necessary which potentially induce flaws at the

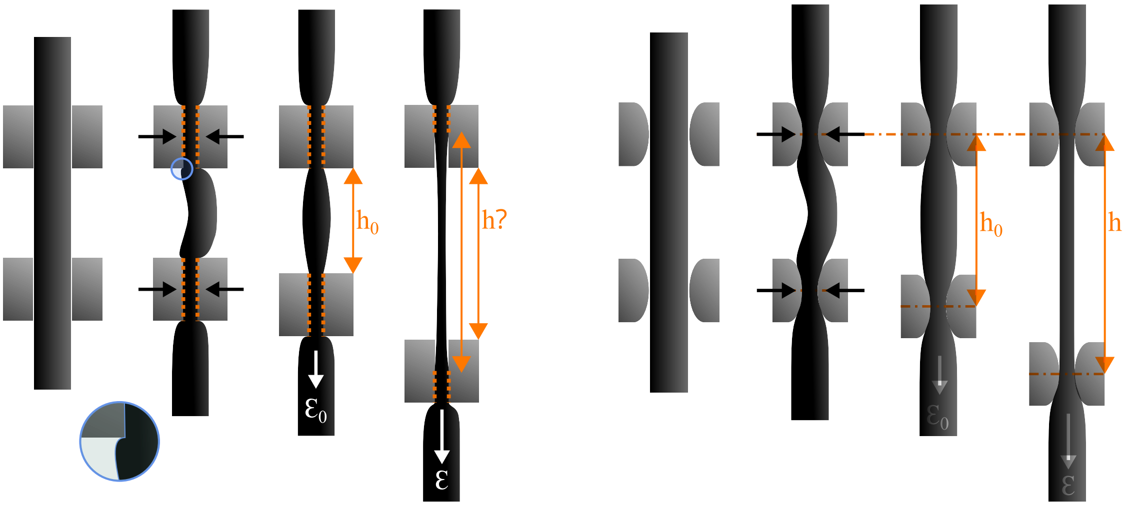

(**a**) With common rectangular clamps.

(**b**) With adapted rounded clamps.

Figure 2.11 Clamping of rubber tension samples.

clamp's edges, as depicted in the blue circle in Figure 2.11a. In addition, the pressure line is not clearly defined throughout the experiment, leading to an undefined height. Thus especially for the thicker samples, the clamping system is adapted to ensure that no points of singularity are introduced, to reduce slipping for higher strains, and to obtain a defined maximum pressure line, as outlined in Figure 2.11b. Since the clamping is fastened, the almost incompressible NR squeezes out of the clamps and buckles. Hence, a small pre-strain is applied to straighten the samples before the actual loading.

Series `Z` and the strain states of 0 and 20 % of series `U` are clamped with flat clamps. Thus, the ageing states should be comparable even if the strain of 20 % may not be fully accurate. The worst possible error to the desired strain of 20 % is -5 to 9 %, considering the clamping length and clamp dimension. Regarding series `U`, the strain state of 20 % is repeated with rounded clamps to be comparable to the strain states of 30 and 40 %. Series `D` and `C` are artificially aged using the rounded clamps.

After the artificial ageing without deformation, it was observed that the compounds without wax generated a sticky surface. The glossy surface is attributed to the chain scissions, explained in Section 1.3.4, leaving short molecules adhering to the surface. When deformed after the ageing process, some samples of `C3` display shallow cracks, see Figure 2.12, indicating that the adherent molecule layer may crack due to subsequent loading. Regarding `C2`, cracks only appeared for extremely high ozone concentrations, as depicted in Figure 2.12. Since 6PPD must migrate to the surface where it is consumed, it cannot protect the NR against an unlimited high ozone concentration.

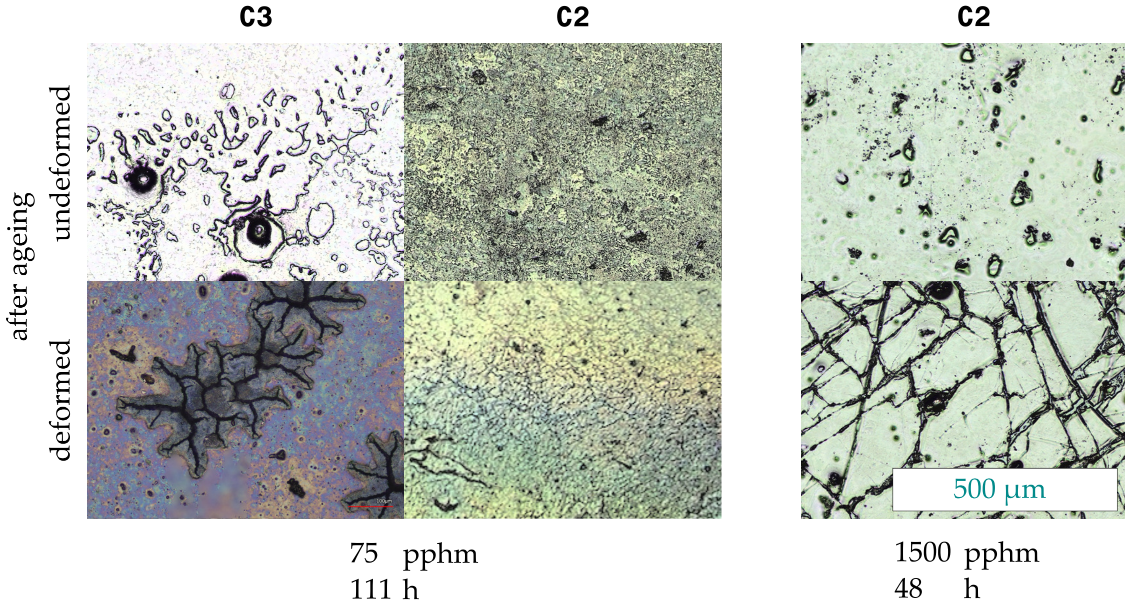

Figure 2.12 Surface pictures taken by LSM after ageing for 111 h at 75 pphm resp. 48 h at 1500 pphm without deformation during ageing but afterwards to crack a possible surface layer regarding `C3` (left) and `C2` (right).

2.6 One-Dimensional Ageing State

In order to obtain a uniaxial ageing gradient, tension test samples are punched from previously aged plates. The punching system, with blades that are sharpened on both sides, leaves visual traces at about 0.7 mm distance to the edge, yet no influence on any measurement was detected though possible cracking as in Figure 2.12. Friction and the necessary strain for cutting are attributed to the marks after punching. After punching, the bars should have 7 mm width and the thickness of the vulcanised or split plate. Regarding the ageing series `U` and `D`, all samples were measured with thickness dial gauges by *Käfer Messuhrenfabrik GmbH & Co. KG*. They determine the thickness with a controlled load of 0.5 N ± 10 % for *JD 200/25* and 1.0 N ± 10 % for *FD 100/25*, both under a 10 mm diameter circular contact plate. Figure 2.13a shows different ageing states of series `U`. One group of samples is measured with *JD 200/25*, showing the influence of a 0.5 N contact force instead of 1.0 N with *FD 100/25* applied for the other strain states. In contrast to the contact force, the ageing state – and thus different crack states – did not influence the measured width. Regarding the samples measured at 1.0 N in

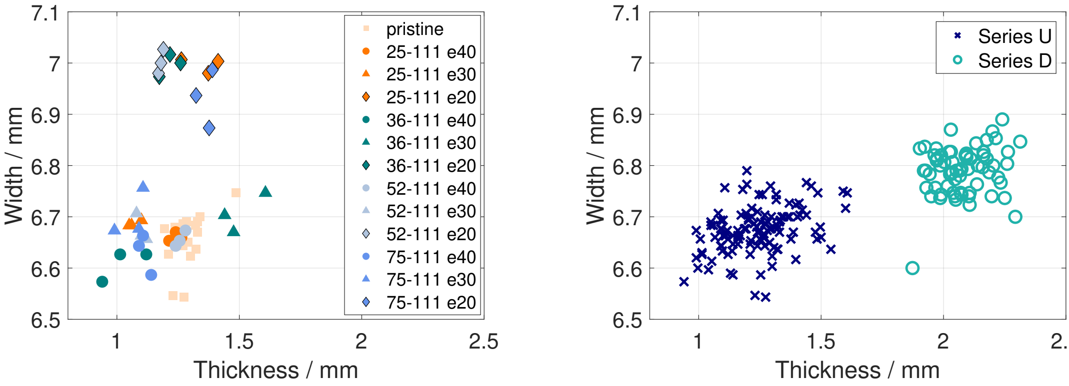

(**a**) Different ageing states (ozone/pphm – time/hours – static deformation/%) of series `U`.

(**b**) Samples including aged states of series `U` and `D` measured with 1.0 N contact force.

Figure 2.13 Relationship of width to thickness of the punched bars after the artificial ageing process.

Figure 2.13b, a minor influence of the sample thickness on the measured width is visible for the range of thicknesses of 0.94 – 2.31 mm. To exclude the possibility of a change in thickness caused by the ageing process, the samples were measured before and after ageing at ambient laboratory temperature.

If you haven't failed yet, you haven't tried anything.
— Reshma Saujani

3
Experimental Analysis

Contents

3.1 Overview of Experiments

Figure 3.1 depicts all experiments conducted to analyse the change due to ozone ageing.

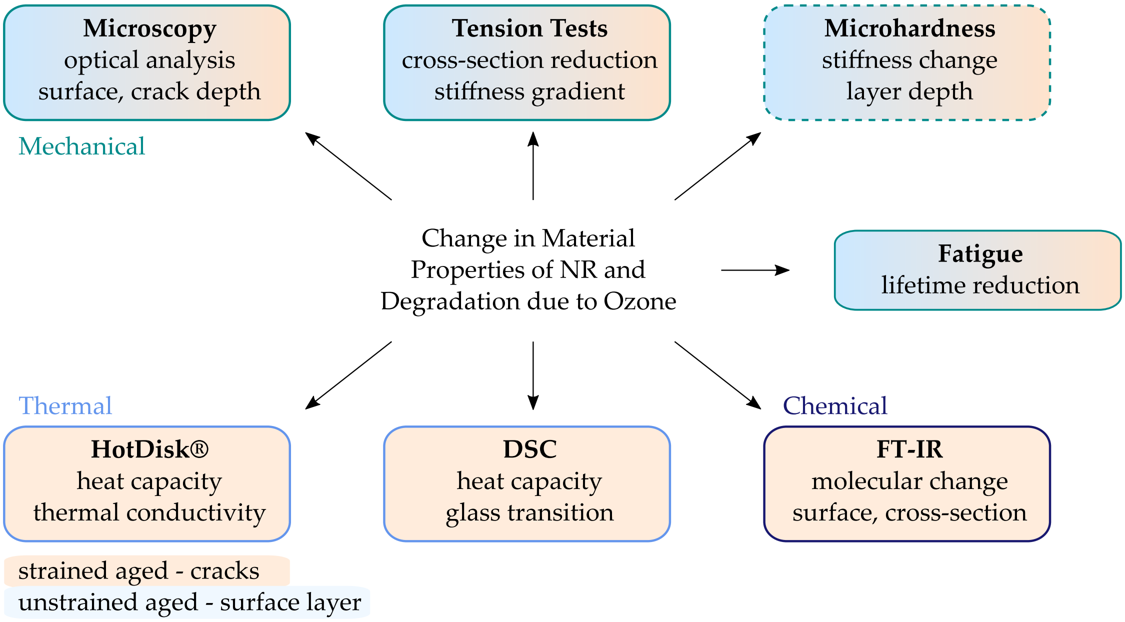

Figure 3.1 Overview of the experiments conducted.

3.2 Chemical and Thermal Experiments

3.2.1 FT-IR

Method

Fourier transform infrared spectroscopy (FT-IR) is a method based on the molecular vibrations excited by infrared radiation. The absorbed bands reveal functional groups and main chain bonds as the molecular mass and binding strength result in characteristic spectra. If ageing states force chemical changes in the molecular structure of NR, the corresponding spectra of unaged compared to aged samples look different.

The spectra are recorded by a *Vertex70* model from *Bruker*$^{©}$ equipped with an attenuated total reflectance (ATR) unit *Platinum ATR* using one monolithic diamond crystal. Its mode of operation is outlined in Figure 3.2. The IR beam runs through the ATR unit, hitting the rubber sample. This creates an evanescent wave with a refraction to be collected by the detecting unit. Wavelengths in a range of $400 – 4000\,\mathrm{cm}^{-1}$ are analysed at a resolution of $4\,\mathrm{cm}^{-1}$ in 32 scans per measurement. To ensure good contact, the aged ozone surface of the rubber sample is pressed onto the crystal.

This method is only applicable to closed planes and not to the edges of a sample. To measure changes towards the sample core, spectra that are close to the edge of the prepared cross-section are required.

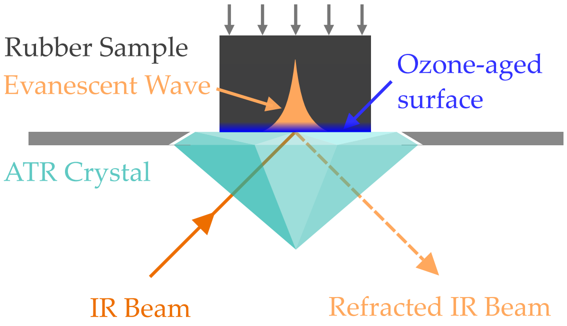

Figure 3.2 Mode of operation: single spectrum ATR FT-IR based on [92].

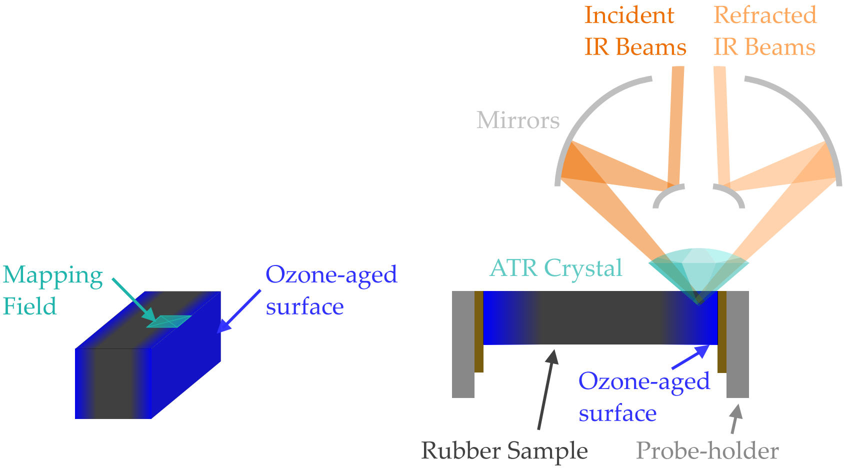

Figure 3.3 Mode of operation: ATR FT-IR microscope and sample preparation with mapping field location modified from [92].

Thus, an FT-IR microscope (*LUMOS II* by *Bruker*©) is used together with an ATR unit. Its mode of operation and sample preparation are shown in Figure 3.3. This device covers a range from 750 – 4000 cm^{-1} at a resolution of 1.6 cm^{-1}, averaging 5 scans. In contrast to the *Vertex70*, the germanium crystal approaches the sample and maps a field of 40 × 40 µm dissolved into 32 × 32 points with each imprint. Since the crystal deforms the rubber during the measurement, the resulting depth of change could be slightly less than documented. Instead of one single point for the surface analysis, mirrors enable the beam to cover the whole mapping field with 32 × 32 measurement points. The mapping field is chosen to cover the edge of the cross-section prepared by cutting samples with a scalpel and fixing them between clamps. It is important to cut the sample at once to create a smooth surface. The probe-holder has a peak around 1100 cm^{-1} used to set the probe edge in the mapping field of the resulting single-point spectra.

In the case of both measurements, the reactions due to carbon dioxide and moisture of the surrounding air are subtracted on the basis of a baseline measurement derived before each spectral image.

A higher density of the material leads to less intense peaks as the IR waves enter less deeply into the sample. In addition to the intensity that changes the results, carbon black raises the measurement noise, hiding narrow and shallow peaks due to its high index of refraction which is close to that of a diamond.

Results

Based on Section 1.3.3, a change in density and molecular groups is expected due to ozone ageing, especially a structural degradation of double bonds to carbonyl groups.

Surface As the intensity of the resulting spectra depends on the contact pressure, the y-axis is an arbitrary unit (Figure 3.4). However, both aged and pristine spectra display differences in the peaks occurring at specific wavelengths.

Changing bandwidths for each of the three compounds are depicted in Figure 3.4. In the surface test, the ageing intensity selected is strong with 15 ppm for 48 h to assess the most important changes and ensure that the end products of the molecular reaction are present on the surface. The spectra of the pristine material were measured to detect the main polymer branches, specified according to Hummel [118]. The peaks at wavelengths corresponding to the main polymer chains do not change during the ageing process. Others do change after the ageing process and both are listed in Table 3.1.

Regarding the larger wavelengths of 1435 $\mathrm{cm^{-1}}$, 1370 $\mathrm{cm^{-1}}$ and 825 $\mathrm{cm^{-1}}$, the peaks are slightly visible while the other main chain vibrations at 2962 $\mathrm{cm^{-1}}$, 2920 $\mathrm{cm^{-1}}$ and 2850 $\mathrm{cm^{-1}}$ are more pronounced. Hummel [118] correlates them to the symmetrical and asymmetrical stretching vibrations of $\delta_s CH_3$, $\delta_a CH_3$, $\delta{=}CH_2$, $\nu_a CH_3$, $\nu_a CH_2$, $\nu_s CH_2$, and CH. If the compound contains 6PPD, a migration of the antiozonant towards the surface due to consumption during ageing is expected. The assigned changes in the spectra of `C1` and `C2` are at 1518 $\mathrm{cm^{-1}}$, 1500 $\mathrm{cm^{-1}}$ and 1320 $\mathrm{cm^{-1}}$. `C1` contains wax in addition to 6PPD, which displays peaks at 2900 – 3000 $\mathrm{cm^{-1}}$ that overlap with the main NR backbone chain peaks. Hummel [118] suggests C–C or C–O bonds causing a peak at 1600 $\mathrm{cm^{-1}}$, whereas C=C–C=C groups are correlated to the vibration by Zheng *et al.* [34]. Consistent with the results of Zheng *et al.* [34] and Lemaire *et al.* [31], the `C3` shows the evolution of a strong carbonyl group vibration around 1740 $\mathrm{cm^{-1}}$. The ozonation of alkenes leaves disrupted vinyl groups such as carbonyl or ketone groups behind, as shown by Criegee [29].

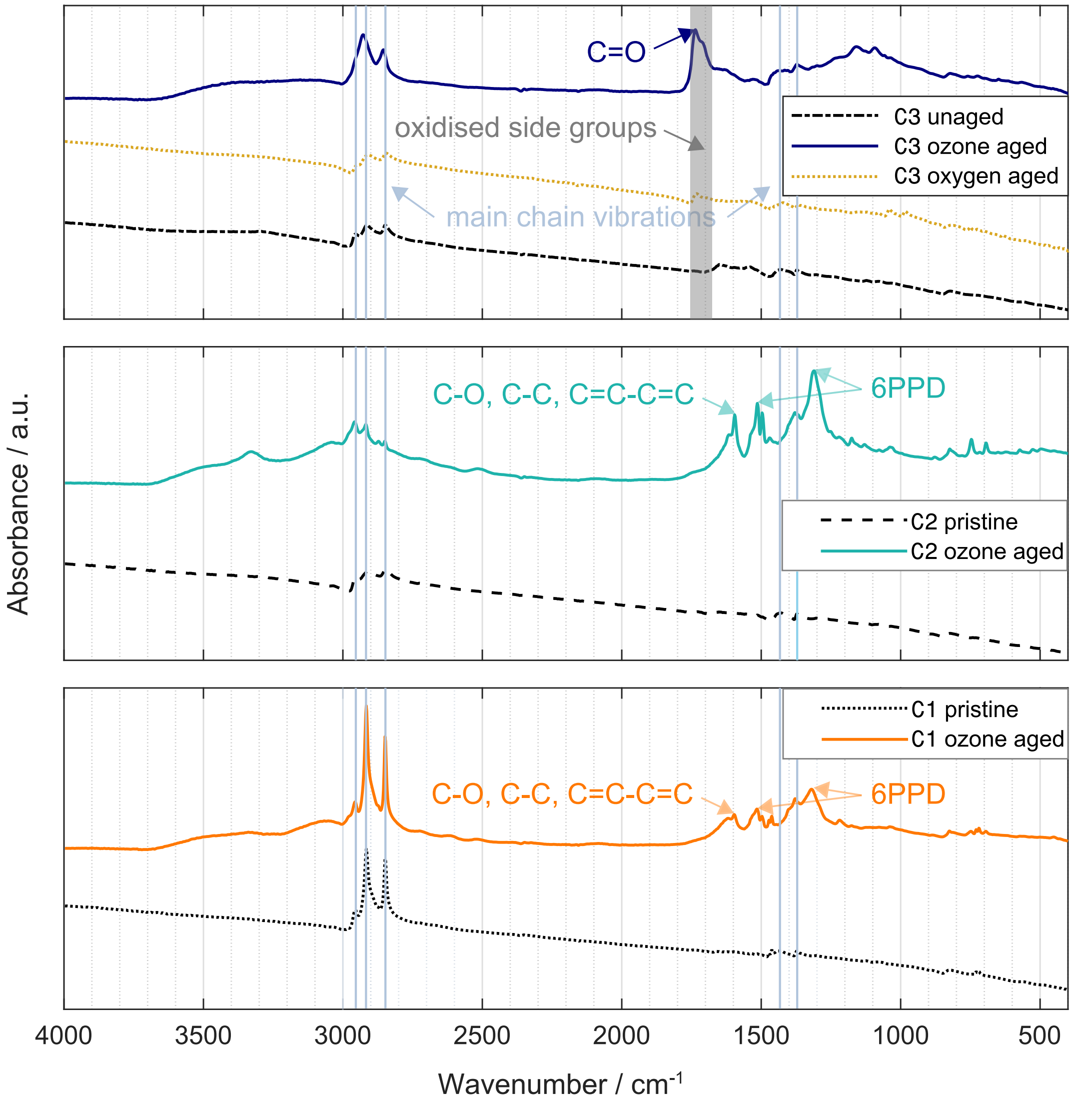

Figure 3.4 Normalized spectra of the surface of all 3 compounds before and after ageing for 48 h at 15 ppm.

Since Colin *et al.* [54] indicated that oxidative ageing forces a change towards carbonyl groups on the molecular level, IR spectra of thermo-oxidatively aged samples of the same material batch are generated. Aligning with the strongest final ozone ageing, they are aged at 40 °C for 111 h. Since the strongest impact is expected for `C3`, the spectra of pristine NR, artificial thermo-oxidative, and ozone exposured NR are provided in Figure 3.4. In an overall view, the different slope of the ozone-aged sample compared to the thermo-oxidative and unaged ones is visible. A peak at 1740 cm^{-1} appears in the thermo-oxidatively aged sample corresponding to carbonyl groups according to Hummel [118]. However, it is

Table 3.1 Wavenumbers ascribed to stretching vibrations of polymer branches as stated by [118].

Wavenumber	Polymer branch
$2962\,cm^{-1}$	$\nu_a CH_3$
$2920\,cm^{-1}$	$\nu_a CH_2$, CH
$2850\,cm^{-1}$	$\nu_s CH_2$, CH
$1370\,cm^{-1}$ and $1435\,cm^{-1}$	$\delta_a CH_3$, $\delta_s CH_3$
$825\,cm^{-1}$	$\delta{=}CH_2$
$1660 - 1740\,cm^{-1}$	Oxidized sidegroups
$1740\,cm^{-1}$	C=O [1]
$1600\,cm^{-1}$	C−C, C−O, C=C−C=C [2]
$1518\,cm^{-1}$, $1500\,cm^{-1}$ and $1320\,cm^{-1}$	6PPD

[1] Stated in addition by [29, 34]
[2] Stated by [34]

more pronounced for ozone ageing in `C3`. In addition, the thermo-oxidatively aged sample exhibits two peaks in the vicinity of $1000\,cm^{-1}$ that are not present for the ozone-aged sample. While the influence of oxidation at the temperature of 40 °C cannot completely be excluded, its influence on the spectra is distinguishable from the ozone ageing.

Cross-section

Bandwidths of interest are detected in the surface spectra in ozone-aged samples. To eliminate differences in intensity in the single spectra caused by the measurement method the following procedure is applied. The main chain wavelengths are present in all ageing states for all compounds, so the area of evolving peaks is related to theirs within each spectra. Thus, a relative change in the ageing-dependent peaks is calculated at each measurement point, as depicted in the line plot in Figure 3.5.

Concerning `C3`, the area of carbonyl groups $1710 - 1760\,cm^{-1}$ is divided by the peak area in the wavelength range of $2830 - 2980\,cm^{-1}$, while the surface edge of the sample is detected by the drop in all vibration peak areas.

The results for the relative peak at $1710 - 1760\,cm^{-1}$ over the whole mapping field are shown in the heat maps in Figure 3.5 for different ageing times and ozone concentrations. On the left edge of the heat maps, the sample surface adjacent to the clamping system is to be found that is defined by the onset of the rag rug of colours due to measurement noise. The intensity of the relative area of C=O

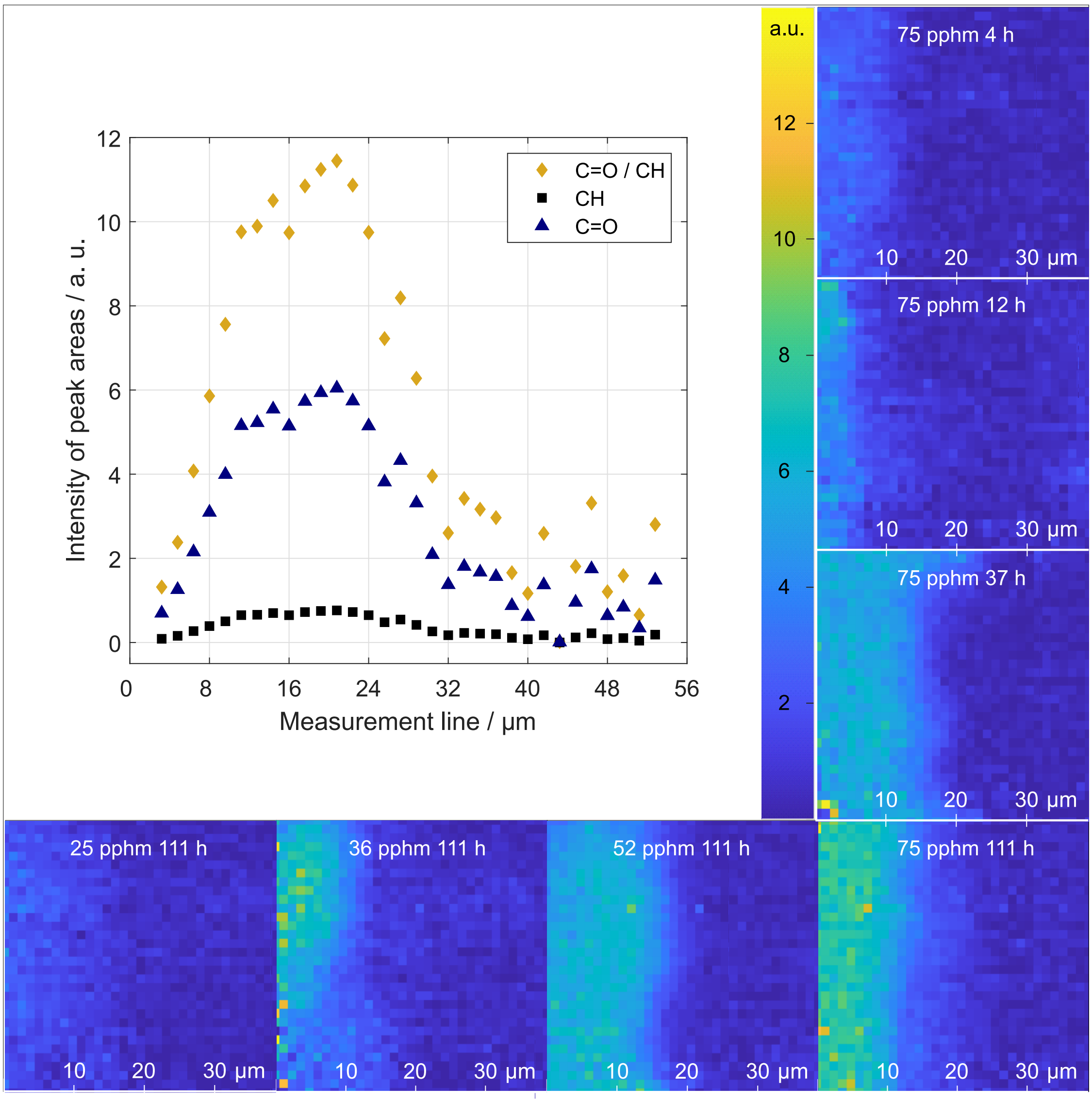

Figure 3.5 Relation of the areas under the carbonyl group 1710 – 1760 cm^{-1} and main chain 2830 – 2980 cm^{-1} vibration in the IR spectra after ageing over the sample's cross-section of `C3`.

peaks regarding the main chains is depicted by the colour bar from blue to yellow.

Regarding the smoothness of the ageing front, it is more or less parallel to the surface. The ageing time, increasing downwards in Figure 3.5, seems to impact the depth of change towards the sample core. A minimum of 10 µm after 4 h of exposure is measured up to approximately 20 µm after 111 h. Changing the ozone concentration at constant ageing time results in a similar depth but different intensity of the relative carbonyl peaks.

Figure 3.6 shows the relative carbonyl peak size in one line of the cross-section for samples of `C3` aged at 75 pphm ozone for different ageing times and

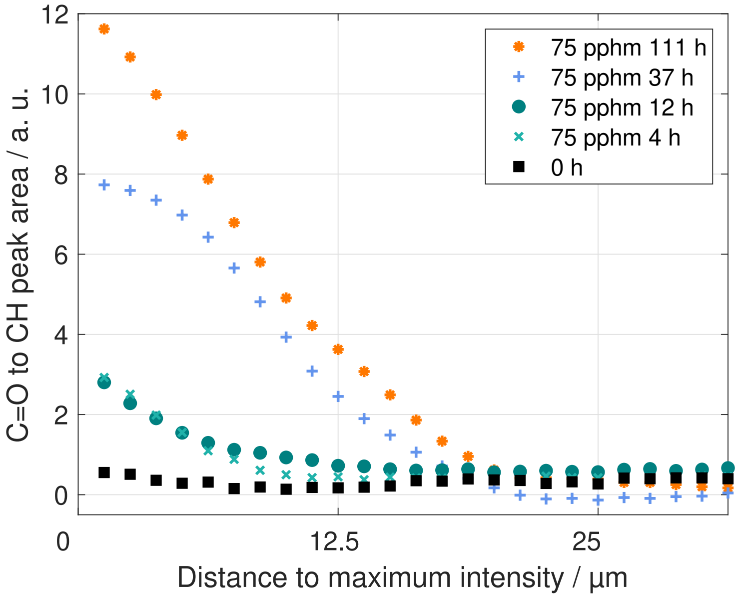

Figure 3.6 Relative carbonyl peak after 75 pphm ozone exposure for different ageing times in `C3`.

an unaged sample. Apart from an increase in ageing depth, a rise in intensity is also detected. The roughly 20 µm-deep change in carbonyl groups is confirmed for the longest ageing time.

`C1` and `C2` did not show enough change over the cross-section to demonstrate an ageing gradient at the wavelengths 1560 – 1640 cm^{-1} detected in the surface analysis. The measurement noise due to carbon black may cover changes induced by the ageing, or else the protective layer successfully hinders migration of ozone to deeper layers towards the core.

3.2.2 DSC

Method

The differential scanning calorimetry (DSC) is used to identify thermal transitions and the corresponding temperatures as indicated by Bergström [119]. Generally, transitions release absorbed energy while heating up but they can also consume energy. In the case of NR, T_g and c_p are mostly relevant.

The basic principle consists of a chamber in which a reference pan and a test specimen pan are placed on a platform to be heated at a predefined rate $\Delta T/\Delta t$, as shown in Figure 3.7. The differential heat flow $Q(P)$ is measured, which is necessary to keep the specimen at the same temperature as the reference pan according to the defined heat rate. Instabilities in the device and changes over time are excluded by the measurement of a baseline heat flow $Q(B)$ with both pans but without any samples inserted, thereby revealing system-based differences.

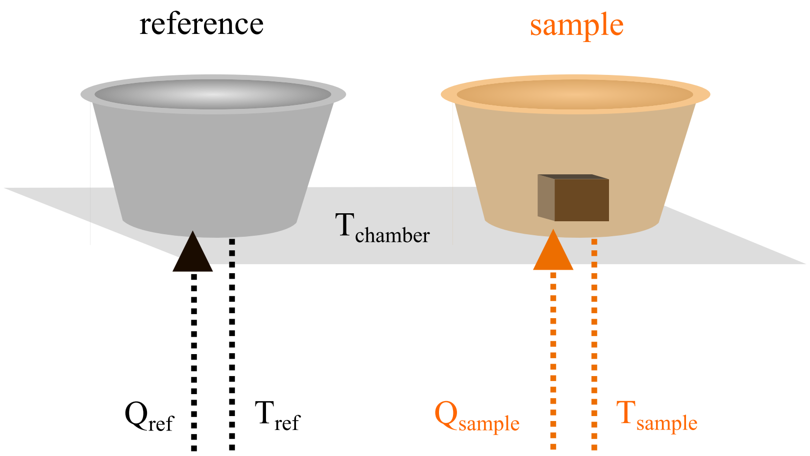

Figure 3.7 Principal sketch of the DSC chamber with sample pans.

With the sample mass m_P, the specific heat capacity c_p can be calculated. Since heat measurements are very sensitive to changes in the laboratory conditions such as the ambient temperature or humidity, a sapphire sample m_s is measured in the same device directly before the sample is evaluated. The data for the $c_{p\text{-datasheet}}$ of sapphire is independent of the temperature rate and given by the device provider. Thus, the relation of sapphire literature values to the measurement in the specific device can be used as a correction factor for the NR sample measurement. A precise measurement of the weights of the samples is crucial, as it directly transfers to the final result.

The equation to best evaluate c_p from the heat signal is given by the following expression:

$$c_p = \frac{Q(P-B)}{m_\mathrm{P} \cdot \Delta T \frac{Q(S-B)}{m_\mathrm{s} \cdot \Delta T \cdot c_{p\text{-datasheet}}}} \tag{3.1}$$

The sample sizes are small, and weigh approximately 10 – 20 µg. In the small volume, no strong temperature gradient can evolve and the assumption of a homogeneous sample temperature is appropriate. Concerning the sample temperature, the contact to the bottom of the sample pan is also important to obtain valuable results. On account of this and to obtain a better ratio of aged surface layer to sample volume in a second ageing batch, the samples are aged in

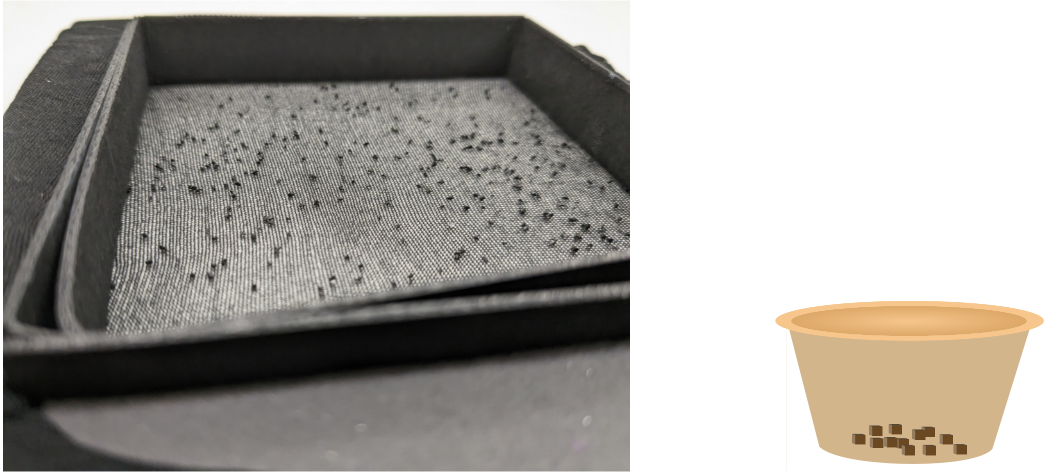

(**a**) Pieces of NR on tight tissue for ageing process.

(**b**) Sample pieces in pan.

Figure 3.8 Sample pieces to increase the surface area for the DSC measurement.

small bits of sample mass below 1 µg (see Figure 3.8). The results of the unaged small bits are compared to those for one bulk piece in Figure 3.9. Similar results are obtained, and thus the difference in sample geometry is concluded to be negligible for the resulting value. The measurement process starts with a heating step to erase possible reversible physical ageing. Then, 3 cycles from −75 to 65 °C are carried out at a temperature rate of $10\,\mathrm{K\,min^{-1}}$. No changes between the cycles were observed but a reproducible result in the differential heat flow was obtained. The measurement accuracy of c_p for the device used is given at ±3 %.

Results

Qualitative changes take place in the specific heat capacity of ozone-aged NR compared to unaged NR of `C3`, see Figure 3.9. The specific heat is lower after the ageing process regarding the pieces with sufficient aged surface area to volume. Between 15 – 40 °C, the specific heat of the aged material climbs to higher values to match the pristine value again, as shown in Figure 3.9. The results for aged bulk material appear to indicate a slight increase, although the difference to pristine material is not marked. No significant change in the glass transition temperature T_G was measurable. Though, Forrest [21] correlates a change of T_G to cross-linking differences between unaged and oxidised samples with especially good results for diene-type rubbers. The T_G measured for pristine and aged material is approximately −60 °C.

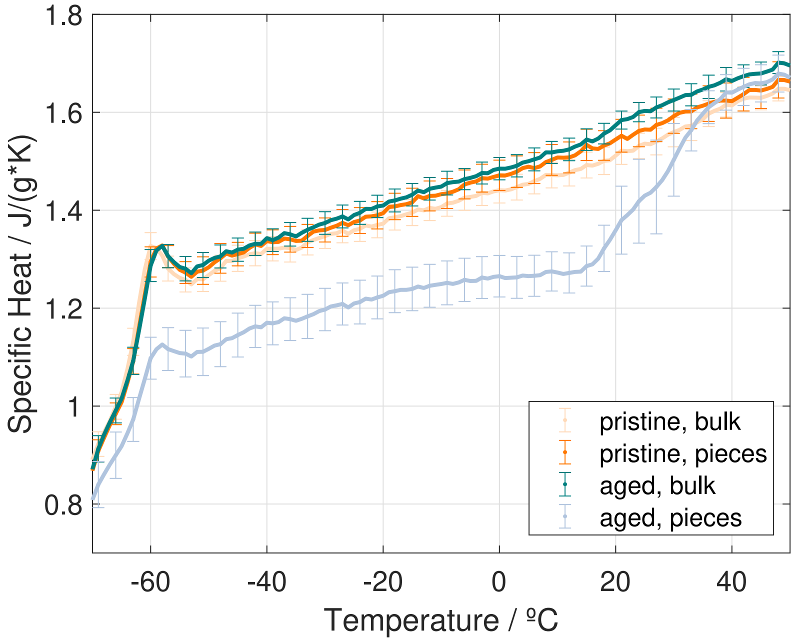

Figure 3.9 Specific heat capacity calculation in DSC measurements of pristine vs aged samples as bulk and pieces of `C3`.

3.2.3 HotDisk®

Method

The *HotDisk*®transient plane source measurement method is based on Gustafsson [120]. The specific heat capacity c_p, thermal conductivity λ_τ, and thermal diffusivity can be assessed. The measurement principle is based on the evolution of the temperature field generated by a single heat source in a sphere or hemisphere. Consequently, a bulk specimen is necessary that matches the assumption of a sphere around the heat source being placed in between two sample parts, as depicted in Figure 3.10. This heat source is simultaneously a resistance sensor measuring the temperature rate defined by the measurement time and heating power. When these process parameters are set correctly, the spherical heat field does not hit any outer sample surface. Using the precise power input, the thermal conductivity and the thermal diffusivity are measured, with the latter being defined by iteration.

The specific heat capacity is assessed by the comparison of an empty container reference and a sample measurement in the same container and the known heating power is used to calculate the specific heat capacity. Since the device's manual considers a thermal conductivity of at least $1\,\mathrm{W\,m^{-1}\,K^{-1}}$ as being preferable, the results should be viewed with caution, as a lower thermal conductivity was

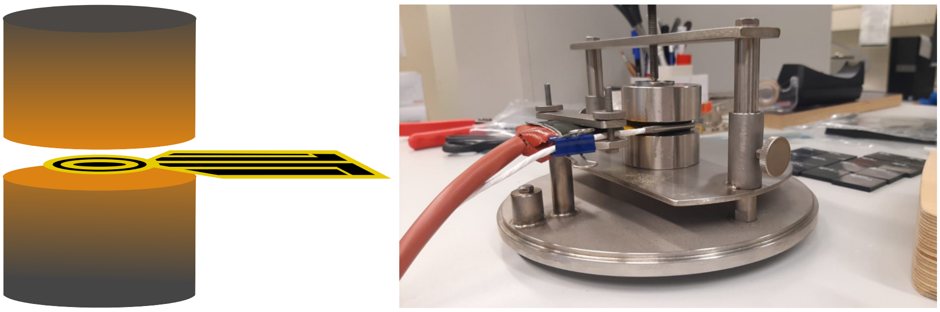

Figure 3.10 Sensor placement in a HotDisk ® measurement for the bulk sample.

measured, as shown in Table 3.2.

The reproducibility accuracy is noted to be ±3 % for the specific heat capacity, ±2 % for the thermal conductivity, and ±5 % regarding the thermal diffusivity.

Results

The results of the *HotDisk*®measurements are listed in Table 3.2. The measured specific heat capacity is transformed to the unit $\mathrm{kJ\,kg^{-1}\,K^{-1}}$ obtained in the DSC experiment with the density measured by a gas pycnometer in Section 3.2.4.

Table 3.2 Results from the bulk measurements with a *HotDisk* ® *Sensor 7854* at 100 mW for 320 s.

Specimen	k, $\mathrm{W\,m^{-1}\,K^{-1}}$	α, $\mathrm{MJ\,m^{-3}\,K^{-1}}$	c_p, $\mathrm{MJ\,m^{-3}\,K^{-1}}$	c_p, $\mathrm{J\,g^{-1}\,K^{-1}}$
1	0.2855	0.1760	1.622	1.506
2	0.3272	0.1855	1.764	1.638
3	0.3379	0.1969	1.716	1.593
4	0.3392	0.2179	1.557	1.446
5	0.3462	0.2110	1.641	1.524
6	0.3451	0.2121	1.627	1.511
7	0.2649	0.2649	1.788	1.660
8	0.3024	0.3024	1.688	1.567
9	0.3109	0.3109	1.647	1.529
10	0.3128	0.3128	1.650	1.532
11	0.3114	0.3114	1.646	1.528
12	0.3138	0.3138	1.705	1.583
13	0.3140	0.3140	1.611	1.496
14	0.3153	0.3153	1.605	1.490
Average	**0.316**	**0.260**	**1.662**	**1.543**

Since the sample thickness is limited to a minimum of 1.5 mm, the aged samples displayed no differences as expected. The influence of an aged surface layer is thus too small to be detected. Nevertheless, the specific heat capacity matches the results of the DSC measurements for pristine material for the testing at ambient room temperature of approximately 20 °C.

3.2.4 Gas Pycnometer

Since the change of measured characteristics might occur due to chain scissions, cross-linking, or volatile parts, the density was tested.

A gas pycnometer filled with helium: *Ultrapyc 5000 by Anton-paar* is employed to qualitatively compare aged to unaged samples. To obtain the maximum aged volume ratio, thin layers are aged at 75 pphm ozone for 96 h, thereby minimising the influence of the sample core underneath the aged surface. Several approximately 200 µm-thick layers aged without strain are stapled in the device to meet the required total volume. Only a difference of 2 % is detected to unaged material, compare Table 3.3. Thus, molecular changes such as chain scissions or cross-linkings seem to compensate each other, resulting in the similar density in the aged state. Since the change in density is not prominent, measurements of an ageing gradient by micro computer tomography (MCT) were not possible, as conducted by Herzig [52] for thermo-oxidative ageing in NR.

Table 3.3 Results from gas-pyknometer with helium.

	Specimen		**Variance**, %	**Density**, g cm^{-3}
	Mass, g	Volume, cm^3		
Unaged	0.2310	0.214	0.2671	1.0769
75/96	0.2245	0.204	0.1685	1.1000

3.3 Mechanical Experiments

Considering the chemical and thermal experiments, the surface needed to be homogeneous, without cracking. Thus, only ageing states without strain were analysed. In the next section, mechanical experiments conducted on both states, i.e. with and without cracks, are analysed. A gradual change in tensile strength throughout the cross-section is considered as stated for thermo-oxidative ageing, e.g. Herzig [52]. Therefore, the layers are split to conduct tension tests and the microhardness is measured within the cross-section towards the aged surface. Further, the crack characteristics are analysed in the surface and the cross-section via uniaxial tension tests and optical microscopy. Influencing parameters are detected and the evolution of measurement results is documented.

3.3.1 Uniaxial Tension: Layers

Method

Aged bone-shaped tension bars of series `Z` with the centre part having a rectangular cross-section of 4 × 2 mm are split into layers of approximately 300 µm, as outlined in Section 2.4. Subsequently, they are deformed at a 0.0167 s^{-1} deformation rate of up to 600 %. Sandpaper is used to cover the clamps and ensure enough friction to prevent the sample from slipping.

Results

Regarding `C2` and `C3`, the surface showed cracks all over the sample after the ageing procedure, including a deformation of 20 % during ageing. This is in contrast to `C1`, where no cracks are visible. When the outermost layer is tensioned, it immediately opens existing cracks in `C2` and `C3`. The cross-section is reduced, which explains a strong stiffness drop and reduced elongation at break from above 600 % to below 150 % for cracked outer layers. Summing up the measured stresses for complete samples, `C1` and even `C2` including cracks show an increased stiffness compared with the unaged sample. In `C3`, the unaged material is equally stiff to the aged one, except for the fact that the outer layers are severely cracked. Concerning the antidegradants, `C1` and `C2` seem to behave like `C3` in the unaged state and the core of the sample from where the antidegradants migrated to the surface under ozone attack.

3.3.2 Microhardness Test

Method

The dog bone-shaped specimens of series `Z` were prepared by the metallographic approach proposed by Clough and Gillen [59] and successfully applied by Musil [44] on NBR. First, the specimen is perpendicularly cut before being embedded in the slow hardening epoxy resin set *EpoFix* by *Struers*. It takes 12 h to complete hardening and was chosen for its low heat dissipation to limit influence on the specimen. The stabilised specimen is polished to reveal and smooth the cross-section surface. Optimal results were achieved by sandpaper discs consecutively used from 320, 500, to 1200 grit size combined with a maximal contact pressure of 5 N and 150 rpm (rounds per minute) plus water to cool while grinding with a polishing machine by *Struers*. When analysed using a LSM, the samples showed a surface roughness below 5 µm.

The indentation modulus is measured with a micro indenter equipped with the Vickers Diamond Pyramid by *Fischer® GmbH*. The values are reproducible in a range of the peak force from 20 mN up to 80 mN. Thus, 50 mN was chosen, resulting in an indentation depth of about 40 – 65 µm. Compared to the surface roughness below 5 µm, the indentation depth is sufficient.

To observe a change in the indentation modulus within the prepared cross-section, a line of discrete measurement points is analysed, as shown in Figure 3.11(right). In between these measurement points for metal, a distance is chosen whereby the indentation diameters of two consecutive points do not touch as they leave imprints behind. However, in the case of NR, overlapping indentations did not influence the resulting values. A marked increase in the measured indentation modulus is detected approaching the hardened epoxy resin, as shown in Figure 3.11(left). This hinders any separation of hardening effects in the surface area from the influence of the proximity of epoxy resin on the measurement point.

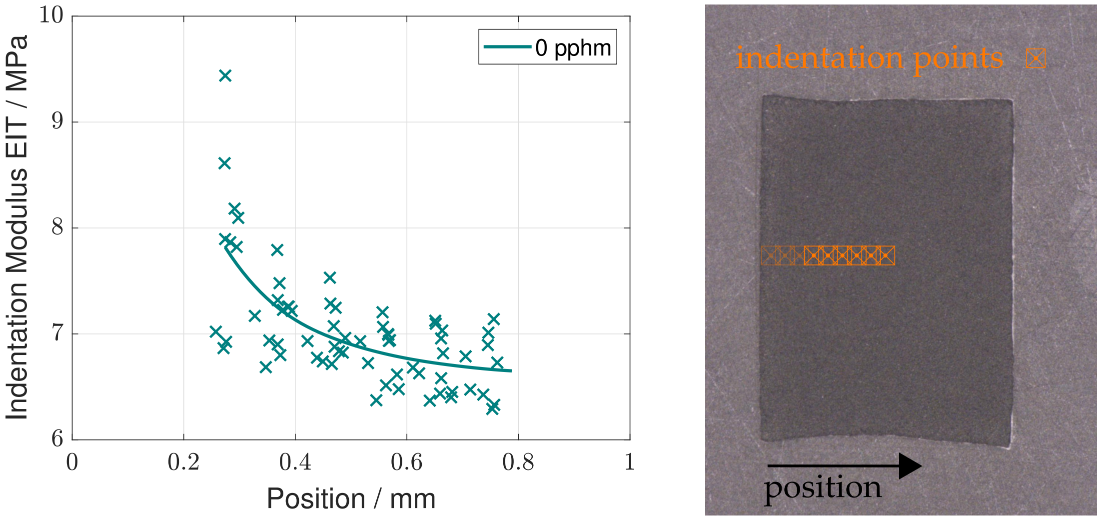

Figure 3.11 Indentation modulus of unaged samples embedded in epoxy resin including trend line.

Therefore, a sandwich structure is prepared from 2 pieces of cross-section of the sample with the surface facing each other to obtain a measurement line over the sample edges without the epoxy resin being in close proximity, as shown in the image in Figure 3.12.

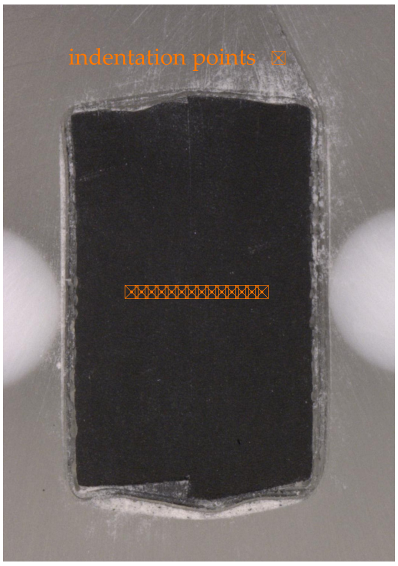

Figure 3.12 Embedded sandwich of 2 samples with a polished cross-section.

(**a**) `C2`. (**b**) `C2`. (**c**) `C3`.

Figure 3.13 Cross-section after preparation for microhardness of `C2` and `C3` after 96 h at 75 pphm ozone and 20 % strain.

Results

Samples strained to 20 % during ageing from series `Z` have cracks after the ageing process. When preparing them to conduct microhardness tests, no even surface roughness could be achieved over the whole sample. A surface close layer rubs off during the polishing process, depicted in Figure 3.13, except for `C1` with 6PPD and wax. Analysing the surface under a microscope reveals height differences of approximately 100 µm on the edge towards the surface for `C2` and `C3`. The centre part of all samples had a surface roughness below 5 µm, like that of the unstrained aged samples. Not even by indenting with higher forces to gain a deeper penetration could reproducible results be achieved in microhardness tests due to the uneven surface.

The difference in topology is present in a distinct layer width towards the sample centre. In this context, `C2` displays the highest homogeneity of the boundary layer, whereas `C3` has an irregular, patchy surface layer extending up to 358 µm

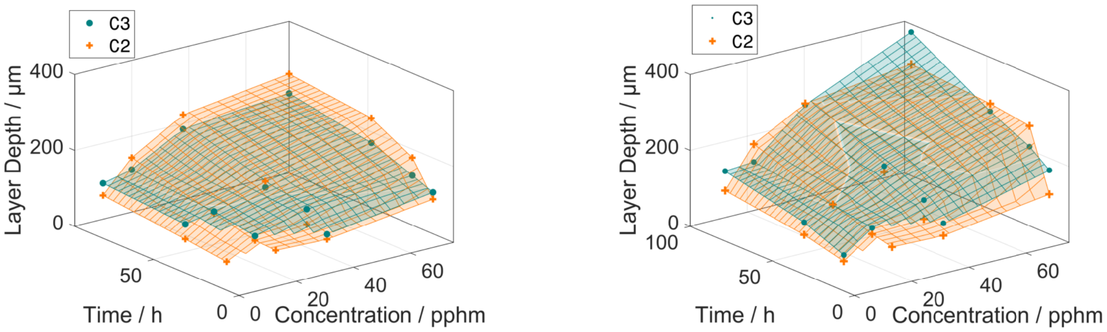

Figure 3.14 Surface layer depth measured by optical microscopy in the cross-section of microhardness samples of series `Z` comparing `C2` and `C3`. **Left**: average; **right**: maximum.

Figures 3.13a and 3.13c. The more even depth of the ruptured layer in `C2` is most probably due to the antiozonant 6PPD. Its migration is forced by a concentration gradient after depletion at the surface, and thus where it is consumed most, 6PPD migrates toward. In contrast, the irregular layer in `C3` is enhanced by ozone taking the path of least resistance in the NR, which chemically is not a perfect isotropic material due to e.g. filler dispersion.

The layer depth detected is pictured in Figure 3.14, and grows with ageing time and ozone concentration. The left plot shows the average of measured depths and the right plot the maximum measured depth. The average layer depth seems to settle at a maximum of about 300 µm, with `C2` at a higher level than `C3`. Considering both compounds, two aspects limiting further progress were identified:

1. The network might relax with ageing time, reducing the present stress and the chain scissions.
2. Reaction products on the surface might hinder diffusion and cover possible double bonds to react with.

The maximum values in the right plot of Figure 3.14 seem not to stagnate for `C3` as they do for `C2`. Coherent with Figure 3.13, the average and maximum layer depths are wider in `C3` especially for less intense ageing states, i.e. short ageing times and low concentrations. The average depth and even the maximal depth for some ageing states of `C2` surpasses the depth in `C3`. Consequently, the use of 6PPD must be precisely adapted to the loads a component faces to ensure beneficial protection.

Embedded sandwich samples could be polished to gain a smooth surface in unstrained aged samples of series `U`. The measured indentation moduli show a hardness increase towards the sample surface placed at the position 1 mm in the sandwich centre, as indicated in Figure 3.15. However, the absolute values scatter, making a correlation to a specific ageing state impossible. Nevertheless, the qualitative sharp and intense hardening over a few 100 µm or less after ozone ageing can be shown by the increase in the normalised indentation modulus (EIT) in 3 samples of `C2` for each 25 and 52 pphm.

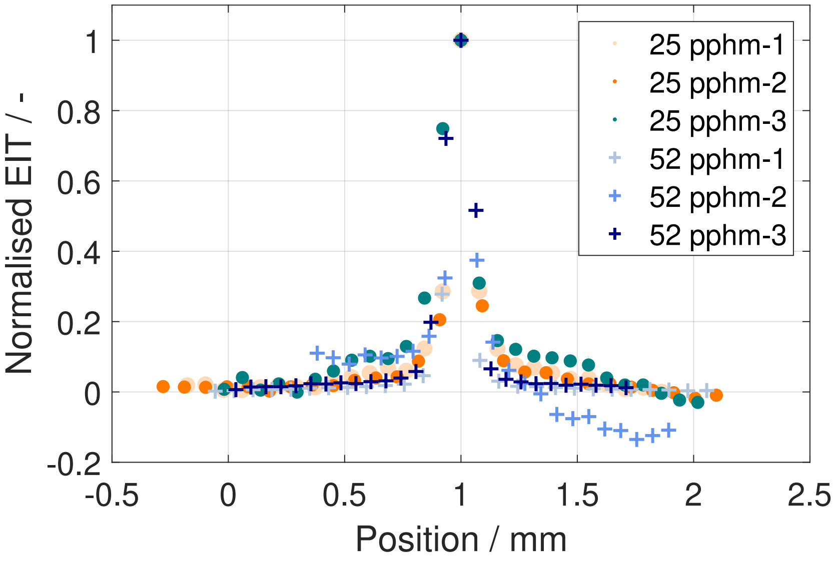

Figure 3.15 Normalised EIT of 3 sample sandwiches of `C2` after 111 h at two ozone concentrations.

The hardening without strain being present during ageing is possibly a result of recombination of scissioned chains with ambient available reactants.

3.3.3 Fatigue Test

Method

Hourglass-shaped buffers are typically used to apply cyclic loads until failure on elastomer samples, as shown by Cam [121] and reported by Gehling *et al.* [1]. First, a double axial geometry has no edge apart from the vulcanising rim from the manufacturing process that represents a slight flaw. Second, the maximal stress is ensured in the middle part, correlating to the most probable position of failure. The hourglass-shaped specimen used differs from all other compounds used by a 10 % proportion of BR next to the NR, as described in Section 2.1. A possible shortening in lifetime due to crack initiation and growth by the ozone ageing process is analysed in the following.

The motivation for fatigue tests is based on the dynamic loading of numerous rubber components. A given component either faces ozone loading before or during mechanical loading. Thus, different types of mechanical load during artificial ageing are realised:

1. No mechanical load
2. Static deformation 30 %
3. Cyclic deformation 0 – 30 %

Afterwards, all samples are tested by a force-controlled cyclic deformation around the unstressed state up to ±120 N. Compressive load had no measurable influence on the increasing deformation during cyclic loading until rupture, as indicated by [53, 73]. Thus, only the tensile deformation part is extracted to apply a failure criterion. A total deformation increase to 120 % relative to the steady state after 1000 cycles is chosen, as recommended by Neuhaus [53]. The steady state is influenced by the time necessary to regulate a smooth oscillation of the mechanical load. The *Mullins Effect* need to pass, dissipative heating must stabilise, and visco-elastic take place. To limit the heat build-up [72] a load frequency of 4 Hz was chosen (following Flamm *et al.* [71]) that was observed to reach a steady state at approximately 40 °C after 400 load cycles independent of the ageing state. After the steady state of total deformation is reached, a slow increase is observed until abrupt fast crack growth leads to the failure criterion or complete rupture. The process is similar for unaged and aged samples, whereby in the case of severe cracks being present after pre-ageing, a shorter phase of the steady-state deformation range is observed.

Regarding the cyclic deformation, up to 400 000 cycles pass during the ageing process and must be taken into account. According to Flamm *et al.* [71] and Harbour *et al.* [73], the so-called *Miner's Rule* [122, 123] of linear crack accumulation is valid for constant load amplitudes, deviating up to a factor of 2 if long block signals are part of the damage sum. During the ageing process, 0 – 30 % cyclic deformation is applied, which correlates to a maximal tensile force of 85 N in the hourglass samples. A *Wöhler Curve* [124] for pristine material is generated for 100, 120, and 150 N amplitude and used to extrapolate the load cycles at failure for 85 N (N_{85N}). Following *Miner's Rule*, the equivalent share $D_{\text{cyclic;ageing}}$ of the failure is calculated by relating the actual cycles during ageing (n_{85N}) to the number of cycles to failure (N_{85N}) for the present loading,

$$D_{\text{cyclic;ageing}} = \frac{n_{85\,\text{N}}}{N_{85\,\text{N}}} \tag{3.2}$$

With the cyclic load after ageing, the total failure comprises the part during and after ageing,

$$D_{\text{failure}} = 1 = \frac{n_{85\,\text{N}}}{N_{85\,\text{N}}} + \frac{n_{120\,\text{N}}}{N_{120\,\text{N}}} \rightarrow N_{120\,\text{N}} = \frac{n_{120\,\text{N}}}{1 - \frac{n_{85\,\text{N}}}{N_{85\,\text{N}}}} \tag{3.3}$$

Consequently, the failure cycles at 120 N excluding fatigue damage from the artificial ageing process are more than the measured $\mathrm{n}_{120\,\mathrm{N}}$. The unknown total cycles $\mathrm{N}_{120\,\mathrm{N}}$ till failure are calculated and depicted in the results for the cyclic deformation cases.

Results

Measurement Deviation Significant deviation in cycles until failure is expected in the experimental data, as a factor of 3 is indicated for the scatter in crack growth rates by Harbour *et al.* [73]. In the case of the experimental lifetime data for pristine material, a maximal deviation factor of 1.7 of the cycles until failure is obtained. In general, more intense ageing leads to larger ranges of cycles until failure if strain is present in the artificial ageing. Only the most intense ageing states tested with static (150 pphm and 111 h) and cyclic (75 pphm and 111 hours) strain during ageing exceeded a scatter factor of 3 relating the range of scatter to average values, as shown in Table A.1 in the appendix.

Crack Initiation The ageing process changes the surface structure and consequently the flaws that might lead to crack initiation or crack growth in the consecutive fatigue loading [72]. Figure 3.16 exemplarily portrays a pristine sample that is compared with two ageing states: 30 % static strain at 25 pphm and at 150 pphm ozone for 111 hours. Both aged samples show open cracks under the strain applied, which are apparently of markedly different sizes as for Figure 3.16b they are not visible by eye.

Usually, the crack initiation is located at the vulcanising rim due to the mould parting line, as cited by several authors, e.g. [53, 71, 73]. However, for ozone-aged samples, such as the one in Figure 3.16b, major cracks leading to failure have also been observed to evolve at different locations, as shown by the crack evolution during intermittent fatigue loads in Figure 3.17. After a sufficiently strong ageing, the flaws initiated by the regular cracking pattern dominate the vulcanizing rim flaw. In some ageing states, even under static strain, major cracks occurred directly after the ageing process, as depicted in Figure 3.18.

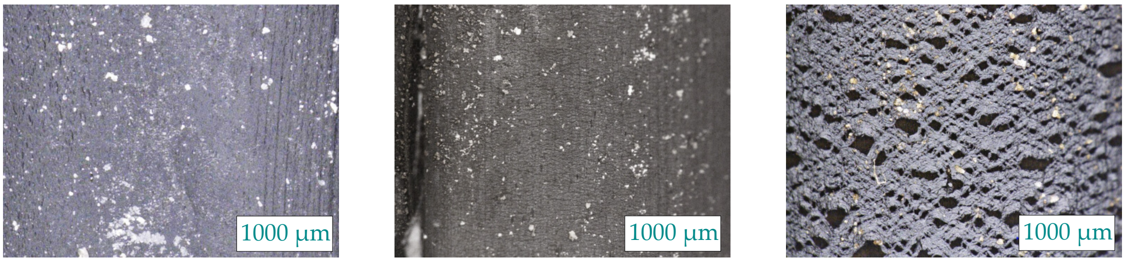

(**a**) Unaged.

(**b**) Aged at 25 pphm ozone for 111 h under 30 % static strain.

(**c**) Aged at 150 pphm ozone for 111 h under 30 % static strain.

Figure 3.16 Optical change in surface after artificial ageing process.

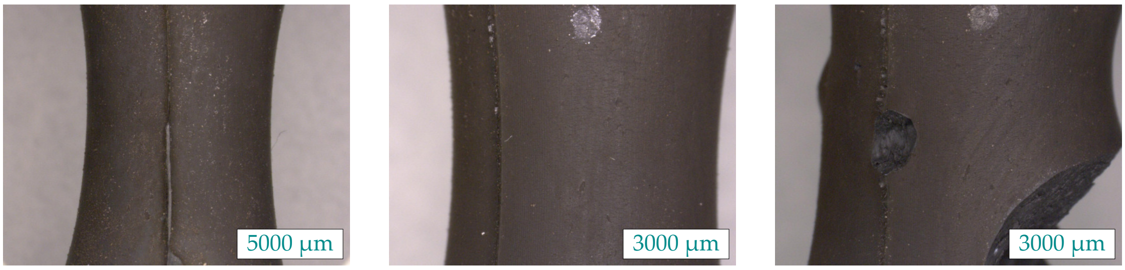

(**a**) Sample without visible cracks after ageing.

(**b**) Surface after 50 000 loadcycles.

(**c**) Major crack opening after 250 000 loadcycles at lower right part.

Figure 3.17 Sample aged at 25 pphm ozone for 74 hours under 30 % static strain.

Lifetime Reduction Figures 3.19 and 3.20 compare the lifetime reduction as the reduction in cycles until the failure criterion was reached due to ozone ageing before the fatigue tests. Figure 3.19a shows the reduced cycles endured in regard to increasing ageing times for static strain being applied at different ozone concentrations. All ozone concentrations lead to a reduction in the lifetime, even though the range of scatter in the measurement data allows no differentiation below 52 pphm ozone concentration. However, all concentrations tested show a minimal lifetime that seems to not be increased after approximately 40 h of ageing time. In contrast, Figure 3.19b depicts the reduced cycles endured in regard to rising ageing times for cyclic strain being applied at different ozone concentrations. The linear damage accumulation theory is employed to correct the damage generated during the ageing process. It is evident that for cyclic strain during ageing, 25 pphm are sufficient to lead to a severe reduction in the number of cycles endured. In addition, the lifetime is further reduced at ageing times above 40 h.

Comparing the strain type in Figure 3.20 for the ageing state after 111 h at

Figure 3.18 Visible cracks in hourglass sample after ageing 55 h at 150 pphm ozone concentration at 30 % strain.

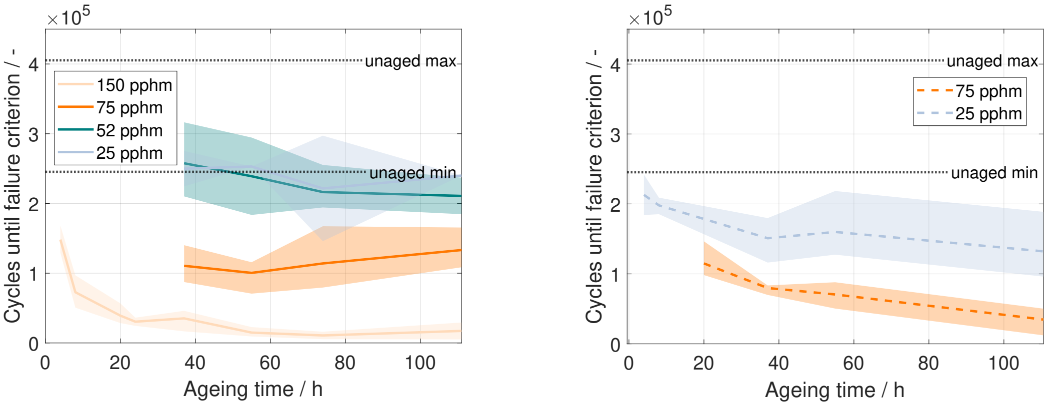

(**a**) 30 % static strain during ageing with scatter bands.

(**b**) 0 – 30 % cyclic strain during ageing with scatter bands; linear damage accumulation during ageing process taken into account.

Figure 3.19 Load cycles until failure criterion.

75 pphm ozone concentration, an apparent reduction in cycles until failure is incidental with static and even more with cyclic strain during ageing.

This leads to the assumption that the depths of cracks present after ageing are causing the reduction in cycles endured as depicted in Figures 3.19 and 3.20, since the cross-section faces the same force amplitude of 120 N. Consequently, a larger tensile deformation at the steady state after 1000 cycles is expected. However, increasing the ageing time does not lead to higher tensile deformation amplitudes in the steady state, as shown in Figure 3.21a. Regarding Figure 3.21b, the type of deformation seems to correlate with the steady state tensile deformation

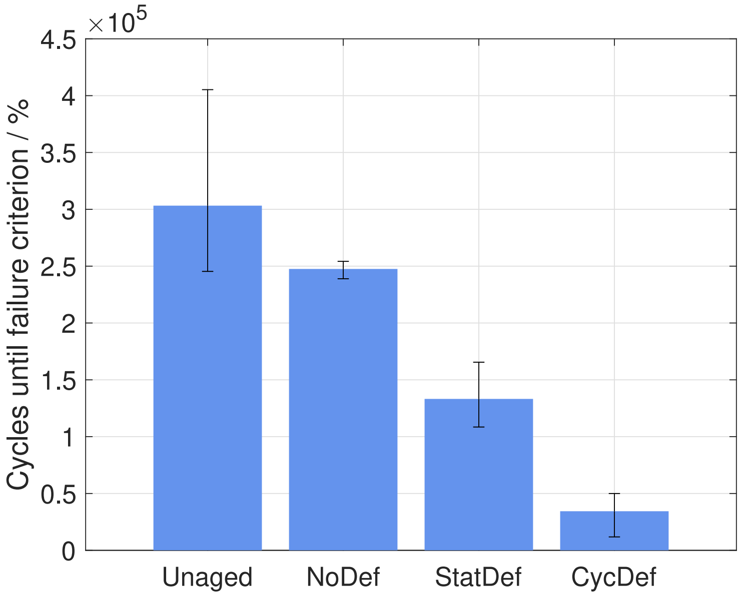

Figure 3.20 Comparison of load cycles until failure criterion for different types of mechanical strain during ageing for 75 pphm ozone after 111 h.

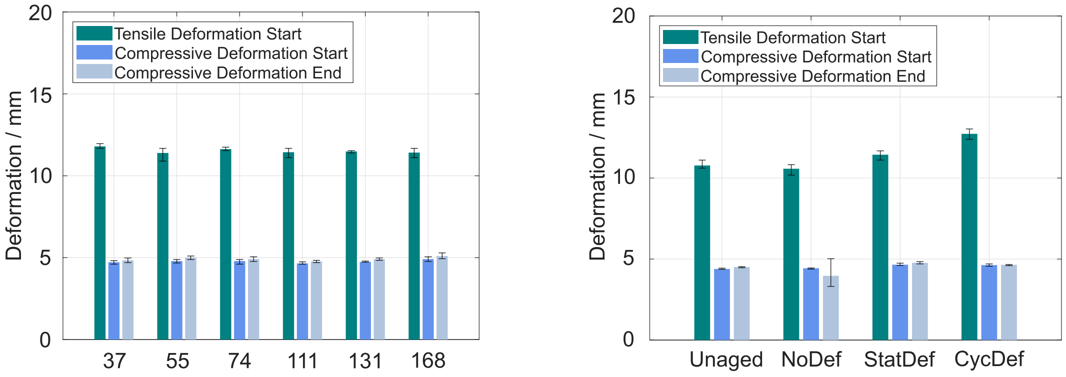

(**a**) Ageing state: 30 % static strain for 37 – 168 h at 75 pphm ozone concentration.

(**b**) Comparison of strain modes during ageing after 111 h at 75 pphm ozone concentration.

Figure 3.21 Deformation amplitudes at steady state (Start) and compressive part at failure criterion (End) at load amplitude of 120 N.

amplitude. However, for the cyclic loading during an ageing time of 111 h, slightly more than 3000 cycles passed and thus a mixed damage of ozone ageing and mechanical damage is observed. The differences in the remaining three states are not as prominent.

Since the crack depth changes with ageing time and deformation mode, only the increased SIC in the crack tip resulting in local heating due to friction and higher strains [72] is considered to cause the stable tensile deformation amplitude.

Even though the ageing temperature of 40 °C is one of the melting peaks of the antiozonant wax applied, it does not prevent the premature failure of aged samples, as indicated in Figure 3.20. In addition, samples with dynamic strain during ageing show earlier failure compared to static strain, which calls the the benefit of movement on the migration behaviour of the wax into question.

3.3.4 Uniaxial Tension: Bars

As [26, 27, 34] report, the FT-IR and the microhardness measurement suggest that a thin layer on the surface changes its characteristics after ozone ageing without simultaneous mechanical strain. The stress-strain curve depicted in Section 2.3, Figure 2.4 shows no severe change after strong ozone ageing without strain being present. Thus, samples of series `U` and `D` aged at simultaneous mechanical strain that display cracks are analysed to determine their degree of degradation via uniaxial tension tests.

Method

The bar-shaped samples punched from the aged plates of series `U` and `D` have a width of 7 mm and a thickness ranging from 0.9 – 2.6 mm. They are tightened with a torque moment of 0.55 Nm in clamps as described in Section 2.5. An aspect ratio of 5 is ensured for the clamping length to sample width before a pre-load of 0.5 N straightens the sample after clamping.

The NR compound contains carbon black fillers (see Section 2.1), therefore the *Mullins Effect* is present [125]. In general, irreversible clusters of filler particles dissolve and break off the polymer chain as indicated by Marckmann and Verron [126], and the effect is visible as a softening in the stress-strain curve in the first loading cycles, as shown in Figure 3.22a. Ten cycles of up to 120 % strain are driven considering only load paths 6 to 10 after the hysteresis stabilised at the driven strain rate of 100 % min^{-1}. The dissipation is caused by the visco-elastic material behaviour. A possible correlation between the ageing and the visco-elasticity is considered by taking the basic elasticity into account. Thus, after the cyclic loading and a holding time of 7200 s, a stepwise relaxation test is performed (see Figure 3.22b). In steps of 10 %, the strain is increased up to 110 % and back to 0 % with holding times of 3600 s between the steps and 7200 s prior to the reverse strain direction. The midpoints of the strain levels held are taken as the basic elasticity curve as drawn in the exemplary Figure 3.22b.

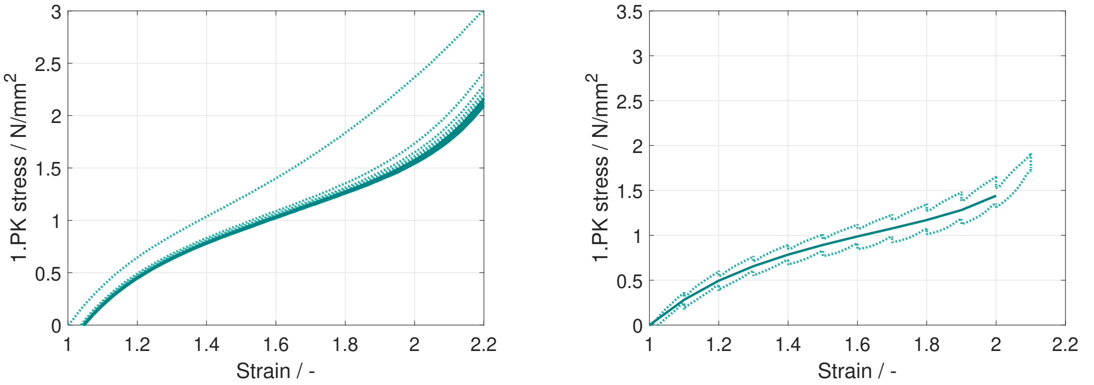

(**a**) Loading paths including stress softening *Mullins Effect* from 10 cycles.

(**b**) Stepwise loading and calculated basic elasticity.

Figure 3.22 Stress softening and basic elasticity by stepwise loading for pristine material.

Pristine Material The NR specimens are vulcanised in plates and they differ from the targeted thickness. Thus, for the uniaxial tests, pristine samples of different thicknesses are compared to exclude differences in the results originating from the measurement setup and the material. The vulcanised plates were sliced to obtain plates of different thickness directly prior of the measurement. Surface layers are excluded to ensure no accidental ageing due to exposure to temperature, light, or oxygen is included. To compare the samples, the cyclic loading part is depicted in Figure 3.23, considering the average of cycles 6 to 10. The range of thicknesses tested covers all tested specimens' thickness of series `U` and `D`.

No correlation could be observed concerning the thickness range and the stress result. A maximum deviation of approximately 0.2 N mm^{-2} is present at a deformation of 200 %.

Oxidative Ageing at 40 °C During the ozone ageing process, a temperature of 40 °C is maintained. Thus, the question arises how the thermo-oxidative ageing processes might change the stiffness in the uniaxial test within the maximum ageing time of 111 h. In the context of deciding on ageing parameters in Section 2.3, Figure 2.3 shows measurements of thermo-oxidatively aged versus pristine material. The range of measurements overlaps greatly, even with a wider spread in the pristine state. The factorial difference between thermo-oxidatively aged and unaged average stress-strain plot counts 11 %. A linear approach is selected to model the stiffening by thermal ageing at 40 °C up to an ageing time of 111 h and subtract if from the results of ozone ageing at that temperature.

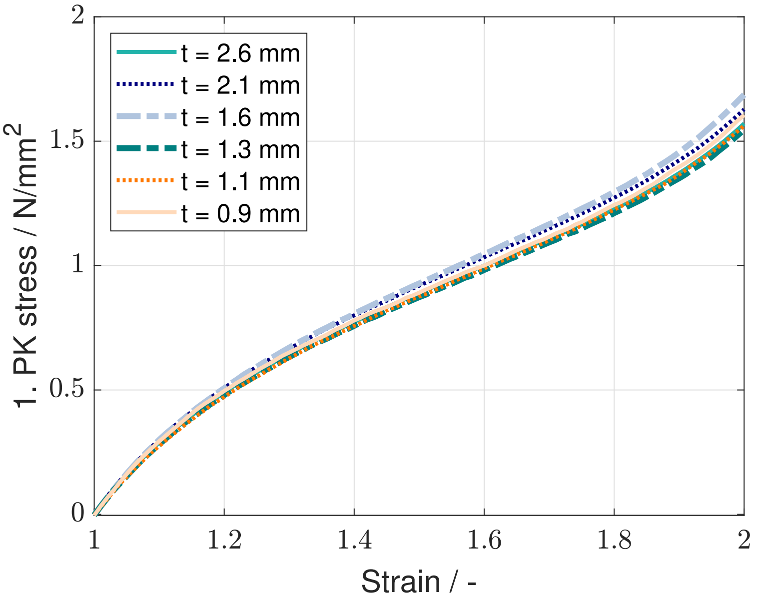

Figure 3.23 Pristine samples' stress-strain curves for varying thicknesses h ranging from 0.9 – 2.6 mm.

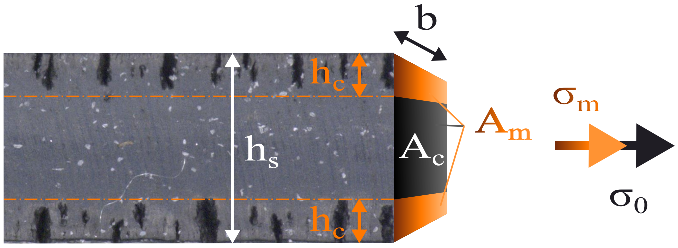

Figure 3.24 Reduction of cross-section due to maximum crack depth h_c with true and measured cross-section.

Stress Reduction Due to Cracks Cracking occurs in ozone-aged samples as some strain is applied during ageing, while the remaining cross-section A_t is reduced, as depicted in Figure 3.24.

The enveloping cross-section A_m is measured before every tension test, including any cracks that are present. The cracked part $h_c \cdot b$ will not transfer forces, and thus at a given strain in the tension test, a cracked sample appears weaker. Calculating the 1.PK stress regarding A_m, it is reduced correlating to the crack depth respectively the ageing state compared to the stress in a pristine sample σ_0. The measured stress σ_m is exemplarily depicted in Figure 3.25 for samples aged at 30 % strain for 111 h at different ozone concentrations.

To calculate the crack depth, some assumptions are made:

- The maximum crack depth is present on both sample sides.
- The cracks are equally deep over the sample width.

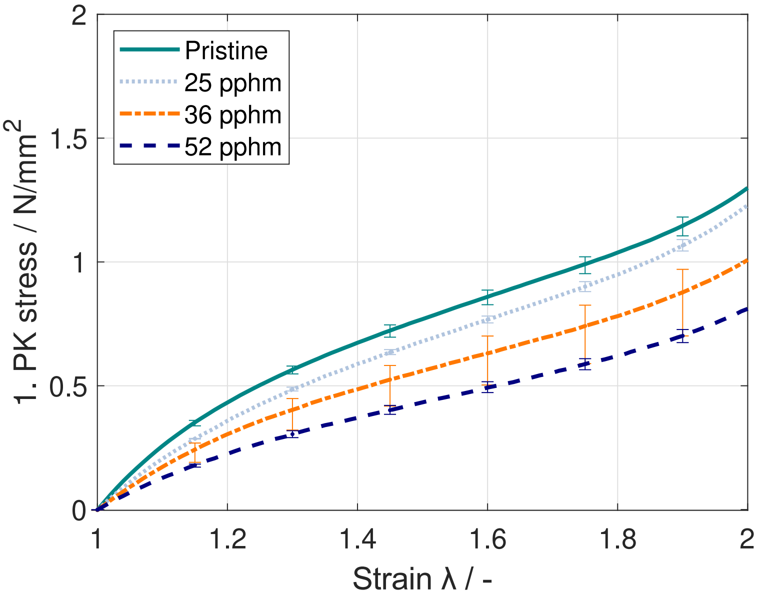

Figure 3.25 Stress reduction after ageing under 30 % strain for 111 h at different ozone concentrations.

- The remaining cross-section contains a stress level similar to that of the pristine material $\sigma_{\mathrm{r},0}$.
- The shallow ageing layer that appears without strain as described in the literature e.g. refs. [26, 27, 47] and Section 3.2.1 causes a negligible change in material characteristics.

Regarding the assumptions, the crack depth is calculated as follows:

$$\begin{aligned} A_{\mathrm{m}} &= b \cdot h_{\mathrm{s}} \\ \sigma_{\mathrm{r,m}} &= \frac{F_{\mathrm{m}}}{A_{\mathrm{m}}} \\ A_h &= b \cdot (h_{\mathrm{s}} - h_{\mathrm{c}}) \\ \sigma_{\mathrm{r},0} &= \frac{F_{\mathrm{m}}}{A_h} \\ h_c &= \frac{\sigma_{\mathrm{r},0} - \sigma_{\mathrm{r,m}}}{2 \cdot \sigma_{\mathrm{r},0}} \cdot h_{\mathrm{s}}\,, \end{aligned} \tag{3.4}$$

where F_{m} is the measured force in the tension test, A_{m} the measured cross-section, b the samples' width, h_{s} the sample thickness, A_h the cross-section excluding cracked area, h_c the maximum crack depth, $\sigma_{\mathrm{r},0}$ the stress level of unaged samples, and $\sigma_{\mathrm{r,m}}$ the calculated stress level for the cross-section including cracks.

Eq. (3.4) can be evaluated at every strain level. However, the strain range used to calculate the crack depth hardly affects the calculated crack depth as a maximum

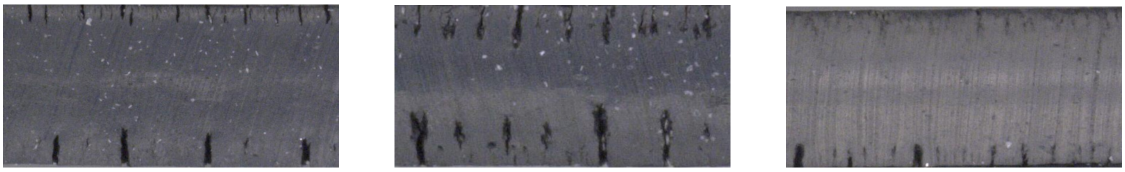

Figure 3.26 Samples with uneven cracking between the exposed surfaces.

change of 10 μm is possible when varying the strain range taken into account. The evaluated strain level is thus selected at 15 % for both methods: stepwise loading evaluating the basic elasticity (basic) and considering the load paths (cyclic).

The assumptions inherit the possible inaccuracies of the method since not all of the samples display a similar crack depth on both sides, as depicted in Figure 3.26. Therefore, the crack depth calculated is an average of both sides. In addition, if the cracks are widespread and not opposite to each other, the cross-section is not reduced by twice the crack depth but only one crack. In this case, the calculated crack depth is only half that of the real one. In contrast, in previous publications such as Treib and Johlitz [80], the crack was assumed to appear at different heights, thereby overestimating the real crack in the case of equal cracking from both sides. The factor of overestimation varies for different samples and ageing states by up to 1.7.

The difference between the two sides might have several experimental causes. Firstly, the ozonized air flow in the environmental chamber might be irregular due to the clamping setup. Secondly, an imperfect clamping could influence the true tension on the sample sides.

Results

Comparing the Cyclic and Basic Approaches Almost identical crack depths are calculated for the basic elasticity and the loading path, as shown in Figure 3.27. This indicates that the viscous effects present at the deformation rate of 100 % min^{-1} do not influence the results of the crack calculation. However, it is evident that the strain level does not seem to linearly influence the crack depth, as the 20 % strain level leads to deeper cracks than 30 % strain, which yields results that are close to the crack depth calculated after 40 % strain being present during ageing.

Impact of the Sample Thickness on the Crack Calculation Since the sample thickness might influence the crack depth, samples of equal ageing state of series `U` and `D` are compared that differ in thickness (see Figure 3.28). Even though the cal-

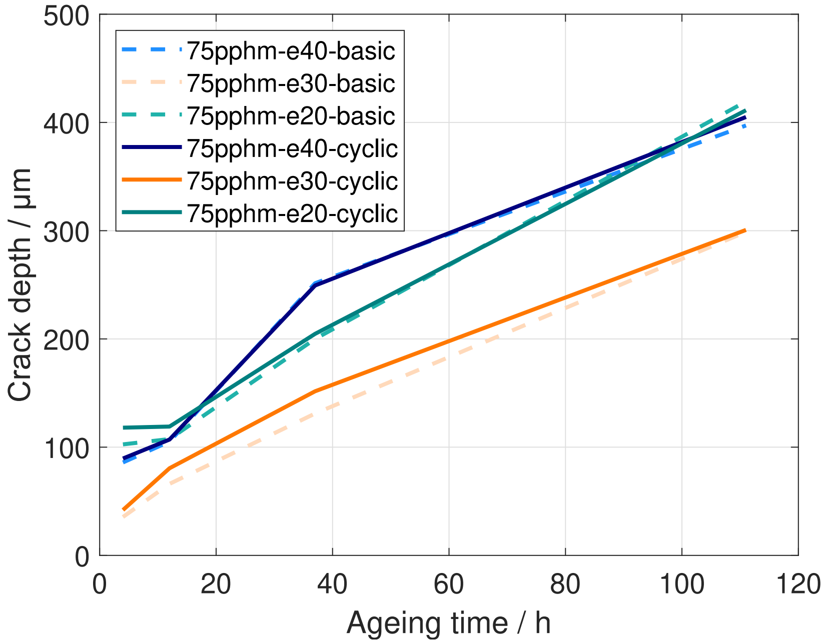

Figure 3.27 Comparison of the crack depth calculated on the basis of the cyclic load path or the basic elasticity from the stepwise loading.

culated crack depth varies, no clear influence of the sample thickness is observed.

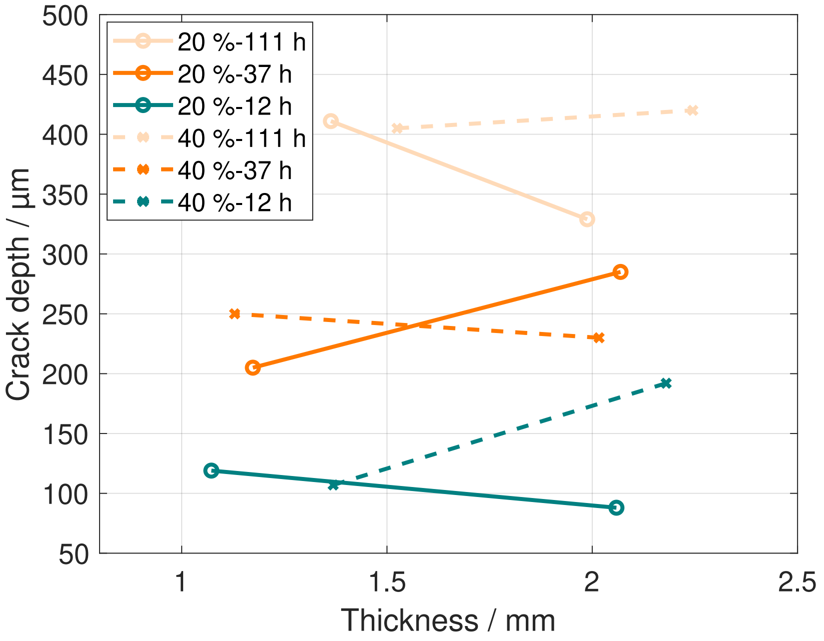

Figure 3.28 Calculated crack depths for samples aged at 75 pphm ozone under static strain ($\epsilon - t_{\mathrm{a}}$) each for two different sample thicknesses.

Influence of Strain During Ageing The ageing time, as opposed to the static strain level, seems to markedly influence the crack depth as shown in Figure 3.28. The crack depth increases by approximately a factor of three between 12 and 111 ageing hours. A comparison of the strain levels for all ageing times and concentrations is presented in Figure 3.29. As mentioned, the static strain level in a range of 20 – 40 % is not clearly correlated to the calculated crack depth.

Considering a wider range of strain levels of series `D` in Figure 3.30, despite the uneven crack evolution it is evident that the ageing time is more important than the strain level above a threshold level of about 10 %. Especially with additional values of the same ageing state of series `U` included, the crack depth seems to hardly increase above 20 % strain during ageing. Considering the ageing times of 12 and 37 h, the cracks are not even significantly higher at 80 % strain compared to 10 % strain.

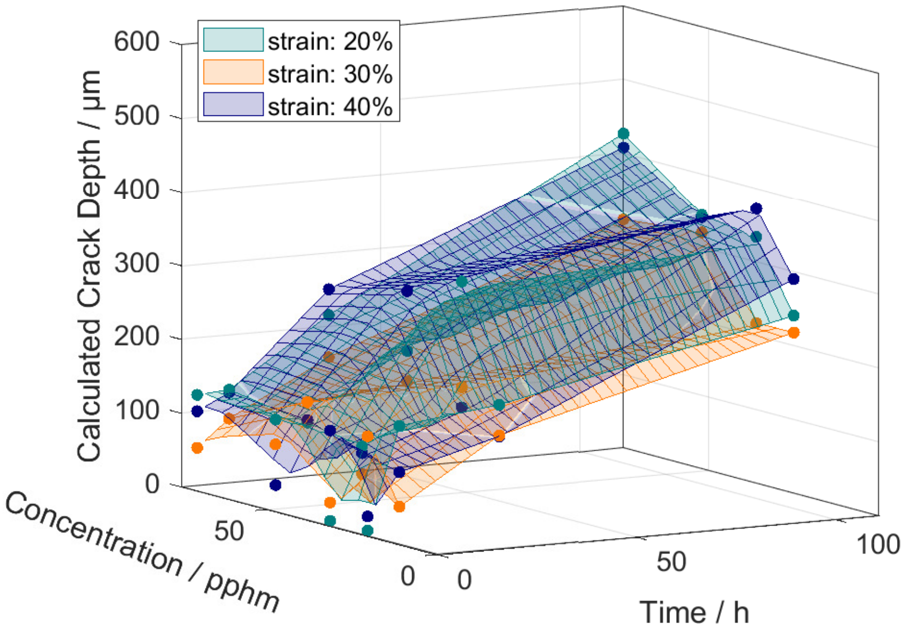

Figure 3.29 Calculated crack depth for 20, 30, and 40 % static strain during ageing.

Two ageing states of `D` had no visible cracks: 0 and 2 % strain after 111 h at 75 pphm ozone. Even for 6 %, strain cracks were only visible for the highest ozone concentration of 75 pphm. At 10 % and higher strains, cracks opened for all ozone concentrations tested.

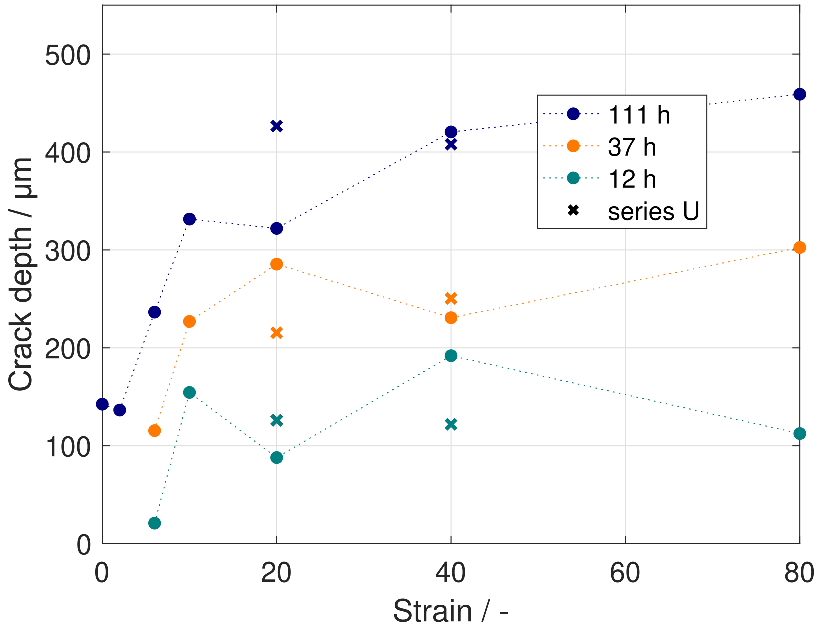

Figure 3.30 Calculated crack depth over strain levels for different ageing times of series `D` at 75 pphm ozone with additional values of the same ageing state of series `U`.

3.3.5 Optical Microscopy

Method

After the ageing process, samples are visually analysed to measure the cracks present on the surface and in the cross-section. A digital microscope *VHX-2000* by *KEYENCE* is used. The magnification levels span from 20 – 200 × at a resolution of 1200(V) × 1600(H)pixel. Thus, depending on the magnification, a ratio of 9.5 µm/pixel to 0.9 µm/pixel is possible, thereby facilitating a quantitative analysis. The minimal magnification factor to measure cracks was 50 times with a ratio of 3.8 µm/pixel. A scale is calibrated and optionally plotted in the figures derived.

NR is an elastomeric material that contracts after deformation so that the cracks are hardly visible in a relaxed state. They are opened by applying about 10 % strain during the analysis under the microscope, as shown in Figure 3.31. To capture the cross-section, it first needs to be revealed. Thus, slim stripes are punched out of the aged specimen as described in Section 2.5. Then, they are turned sideways and clamped to apply some strain to open the cracks.

A high contrast between surface and cracks is achieved with the halogen lamp of the microscope, whereby automated processing of the pixel data is possible. The surface cracks are analysed with the software *ImageJ* using the ratio of µm/pixel.

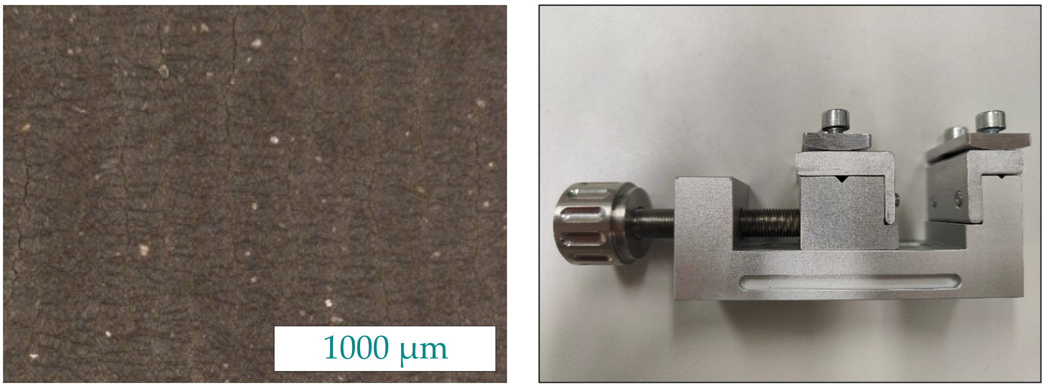

(**a**) Closed cracks in the relaxed state. (**b**) Stretching tool.

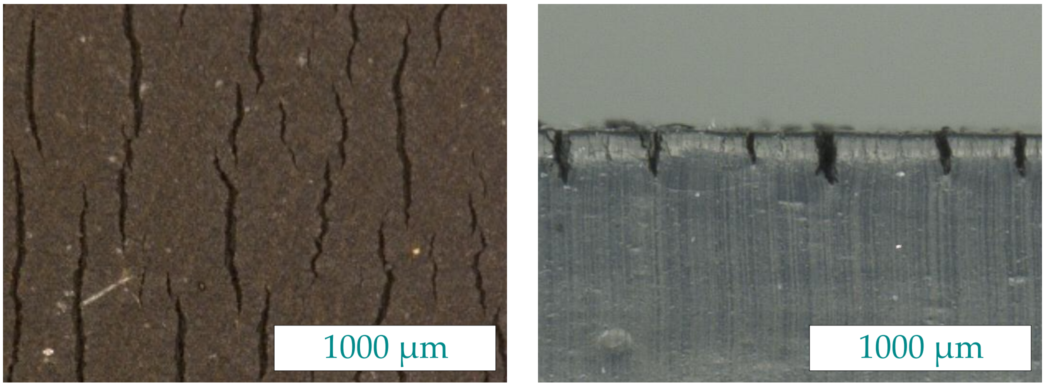

(**c**) Opened cracks in the surface. (**d**) Opened cracks in cross-section.

Figure 3.31 Images taken with the digital microscope on the surface and in the cross-section of ozone-aged samples.

Since the edge is not automatically detected, the crack depth in the cross-section is measured manually by the microscopy software. Apart from the strong scatter in the crack depth, the manual measurement implies some inaccuracy. 100 measurements were taken of a homogeneous ageing front of 286.7 µm in the same manner as all other measurements of the crack depth. A total range of 53 µm was obtained with a standard deviation of 12.4 µm at an interquartile range of 14 µm. A large range of crack depths is obtained, as exemplarily plotted in Figure 3.32. The distribution of crack depths for each ageing parameter set does not show any correlating pattern—not even between the compounds.

Pristine Material In Figure 3.33 pristine material is depicted on the surface and in the cross-section for comparison. No flaws or cracks are visible in the surface or cross-section apart from the lines of the razor blade from punching the sample in the cross-section.

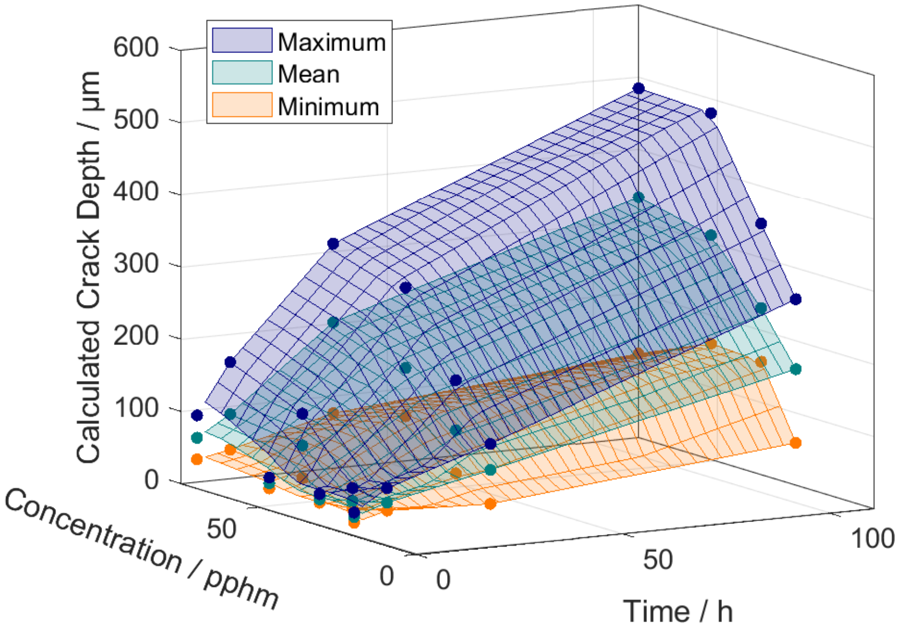

Figure 3.32 Range of measured crack depths in optically analysed samples of series `U` and 40 % static strain during ageing.

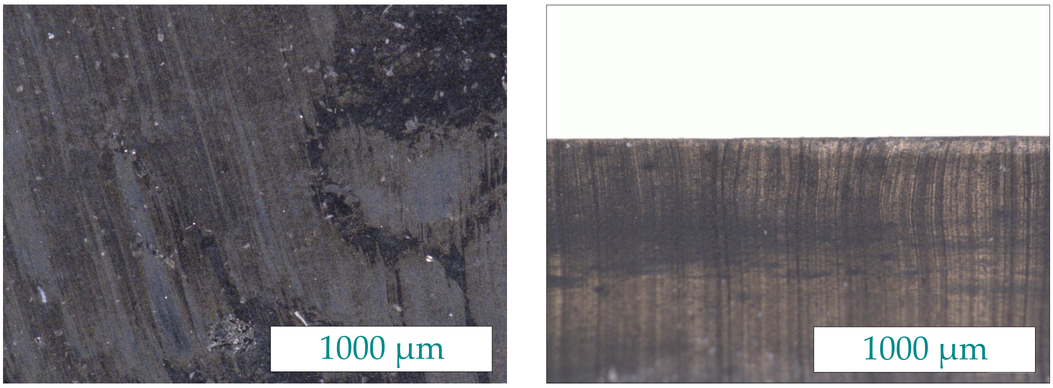

Figure 3.33 Images taken with the digital microscope on the surface and in the cross-section of pristine samples.

Oxidative Ageing at 40 °C The cracks due to thermo-oxidative ageing and ozone ageing differ after an exposure for 111 h to 40 °C at 20, 40, and 80 % strain and air respectively 75 pphm ozone concentration, as shown in Figures 3.34 and 3.39. The difference is significant: thermo-oxidatively aged samples show flaws the size of a few microns that are not correlated to the strain direction, are irregularly spread, and which do not appear throughout the sample. However, the flaws become more numerous at the highest strain level of 80 %, as depicted in Figures 3.34a, 3.34b, and 3.34c. Regarding the cross-section, not even under the highest magnification could any cracks be observed, as shown in Figure 3.34d. On the contrary, the ozone attack leads to cracks measuring to above a millimetre length being clearly perpendicular to the strain direction (see Figure 3.39). The cracks due to ozone loading are markedly different in terms of their orientation, size, and depth. Thus, the flaws initiated by thermo-oxidative ageing at 40 °C are considered negligible regarding the optical analysis of cracks induced by ozone loading.

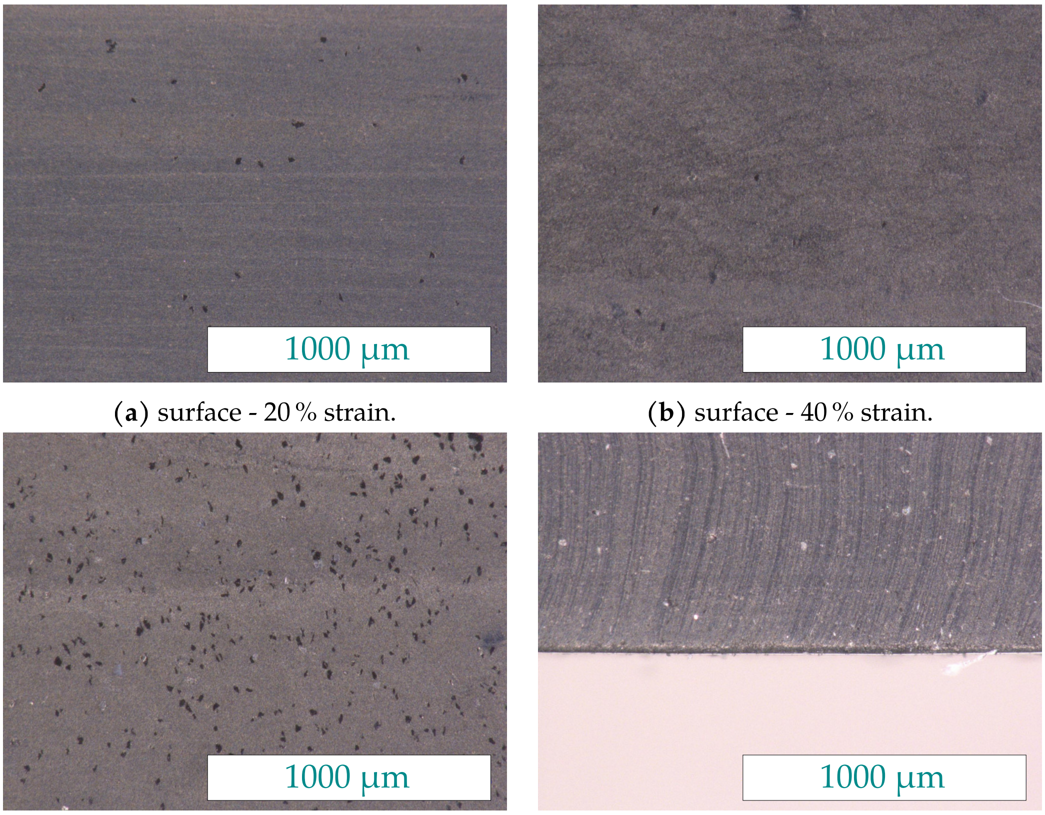

(**a**) surface - 20 % strain. (**b**) surface - 40 % strain.

(**c**) surface - 80 % strain. (**d**) cross-section - 80 % strain.

Figure 3.34 Cracks due to oxygen at 40 °C for 111 h at different strain levels.

Results

Crack Characteristics Depending on Ageing Protection Depending on the antiozonants and the ageing parameters applied, the surface has a different visual appearance in the unaged state (see Figure 3.35). The surface glossiness is dependent on the antiozonants: 6PPD slightly reduces the shine, whereas wax causes a completely dull surface. The shine remains similar after ageing, although `C2` and `C3` become somewhat sticky.

Cracks evolve to different extents and in varied manners. Comparing the surfaces before and after ageing in Figure 3.36 for static deformation during ageing, hardly any cracks are visible in `C1` whereas some evolve in `C2` and `C3`.

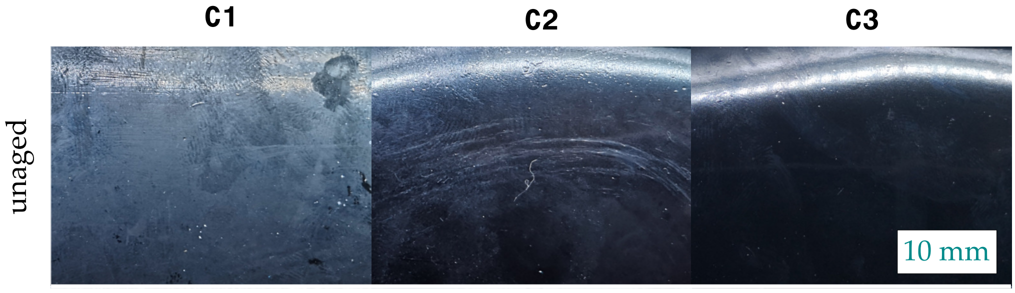

Figure 3.35 Pristine surfaces of `C1`, `C2`, and `C3`.

All cracks are clearly oriented laterally in the strain direction. `C2` with chemical protectant 6PPD has homogeneous crack edges whereas, without antiozonants, the cracks display unsteady edge lines. Some samples of `C1` show migrated wax on the surface clumped together depending on the migration history during ageing, storage, and transportation. The material `C4` used in the fatigue tests contains wax, like `C1`, although clearly visible cracks appear in response to static strain, as shown in Figure 3.18. This demonstrates the strong dependence of the efficiency of the wax on a given mechanical load and temperature during ageing.

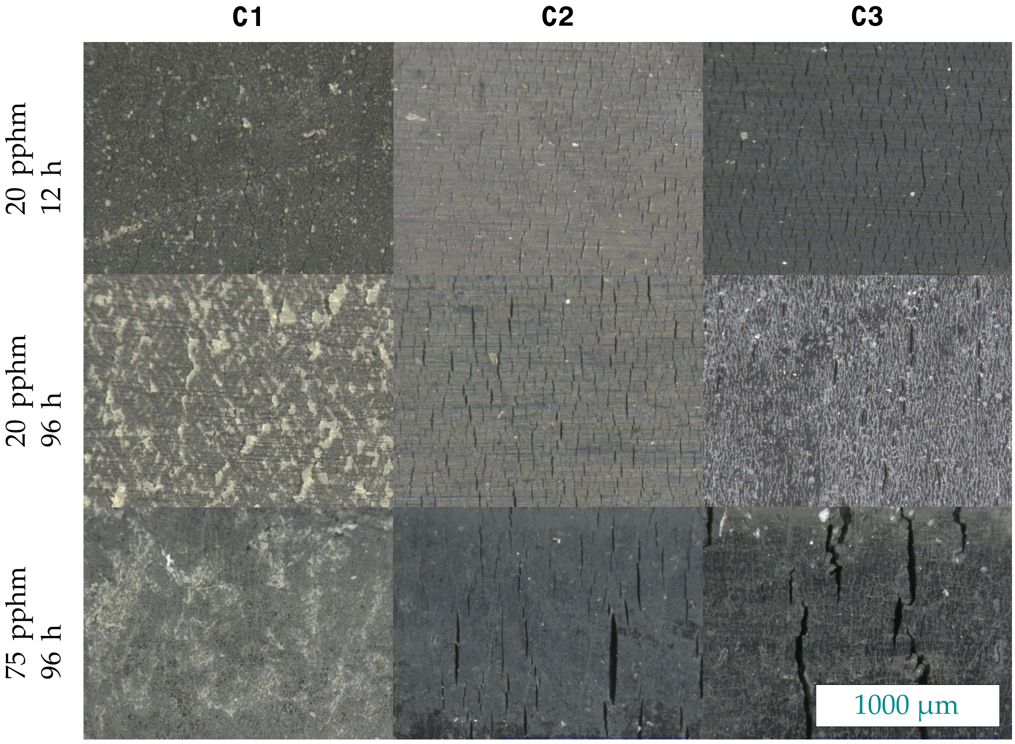

Figure 3.36 Surfaces of `C1`, `C2`, and `C3` aged under 20 % strain of samples of series `Z`.

When dynamic strain is present during ozone loading, no ageing protectant works satisfactorily as they do not prevent cracking of the surface. However, it seems to lead to longer and, considering the static strain during ageing, less branched crack geometries, as shown in Figure 3.37.

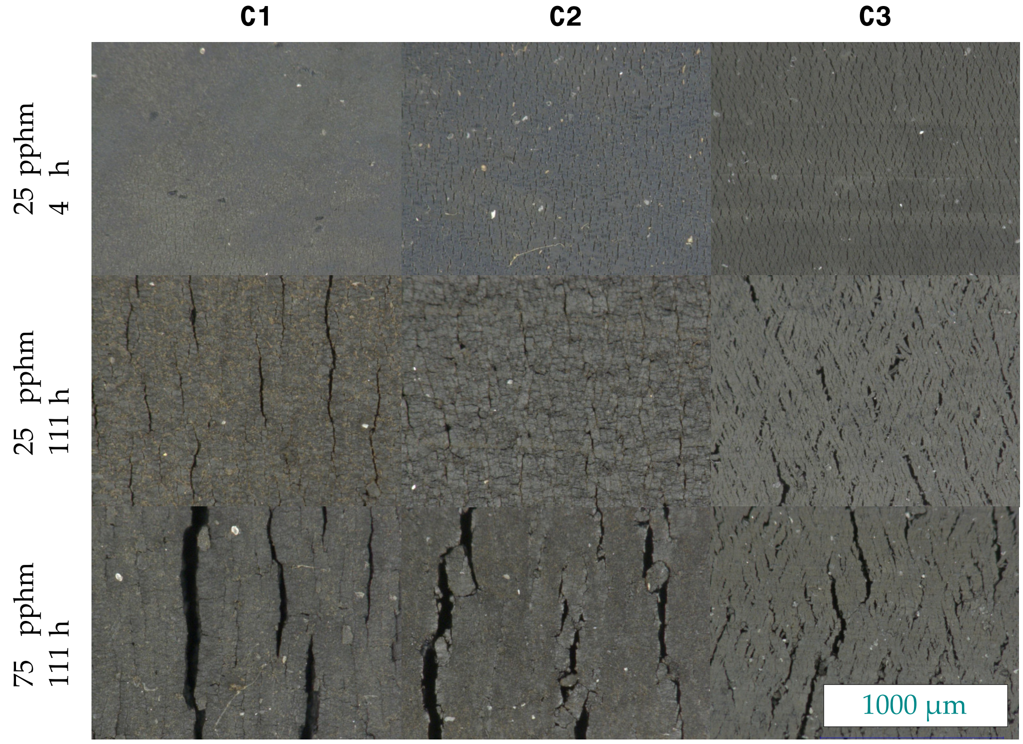

Figure 3.37 Surfaces of `C1`, `C2`, and `C3` aged under 30 % static strain and 10 % strain amplitude.

The cracks on the surface are visible in the cross-section. Regarding Figure 3.38, some samples of `C3` show cracks that are hidden in the surface. The phenomenon is not present in all samples of one ageing state and it could not be overcome by applying more strain when viewing the sample under the microscope. None of the samples of `C1` and `C2` display a similar behaviour, regardless of which type of strain or ageing state is observed. The subsurface cracks are attributed to the stronger branching behaviour in `C3`, which is possibly based on a stronger crack growth resistance without the antiozonants.

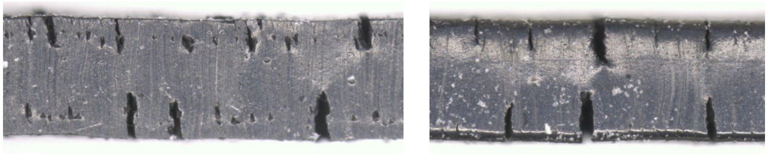

Figure 3.38 Comparison of two samples' cross-sections after 52 pphm for 111 h.

Surface Cracks As Figure 3.30 in Section 3.3.4 depicts for the uniaxial tests performed, the crack depth stagnates with increasing strain. Similarly, the surface crack images approach a final type, depicted in Figure 3.39, for strain levels from 2 – 80 % after 75 pphm for 111 h. A threshold strain is necessary, as indicated in Section 1.3.4 since 2 % strain is not sufficient for cracks to evolve, whereas between 6 – 10 % strain, the difference is apparent in the crack shape. Both strain levels show irregular patterns compared to the higher strains, although the crack geometry looks similar from 10 % on.

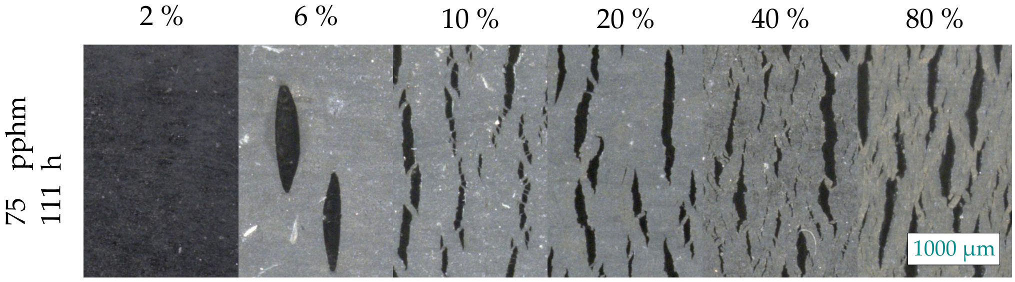

Figure 3.39 Surfaces of `C3` after ageing at 75 pphm for 111 h at different static strain levels.

The crack distance is analysed laterally to the strain direction during artificial ageing (Figure 3.40). As shown in Figure 3.39 portraying the surface, little change was observed in the distribution of the crack distances above a strain during ageing of 10 % for the ageing time of 111 hours (see Figure 3.40(c)). Considering the ageing times of 12 and 37 h plotted in Figures 3.40 (a) and 3.40 (b) at 6 %, the strain level is insufficient for enough cracks or none are present at all. Nevertheless, even at shorter ageing times, the distribution of crack spacings is similar for all higher strain states.

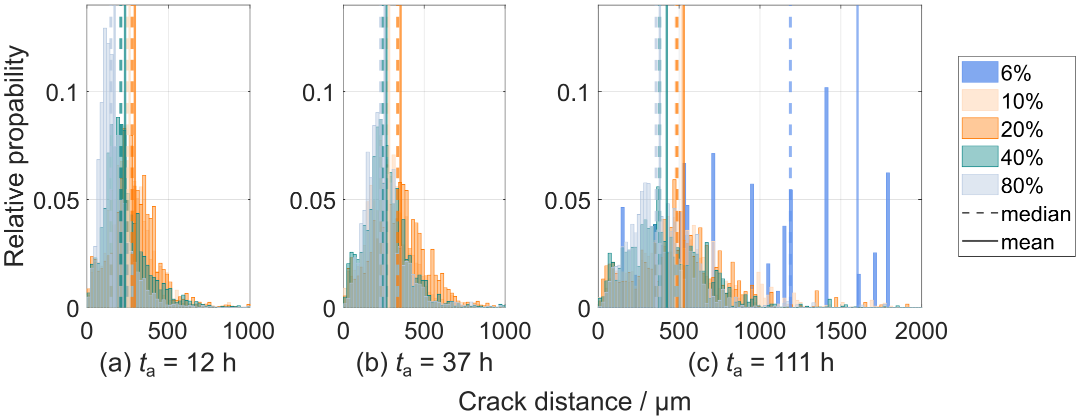

Figure 3.40 Normalised distribution of crack distances after 75 pphm ozone at different strain levels during ageing times of 12 h, 37 h and 111 h.

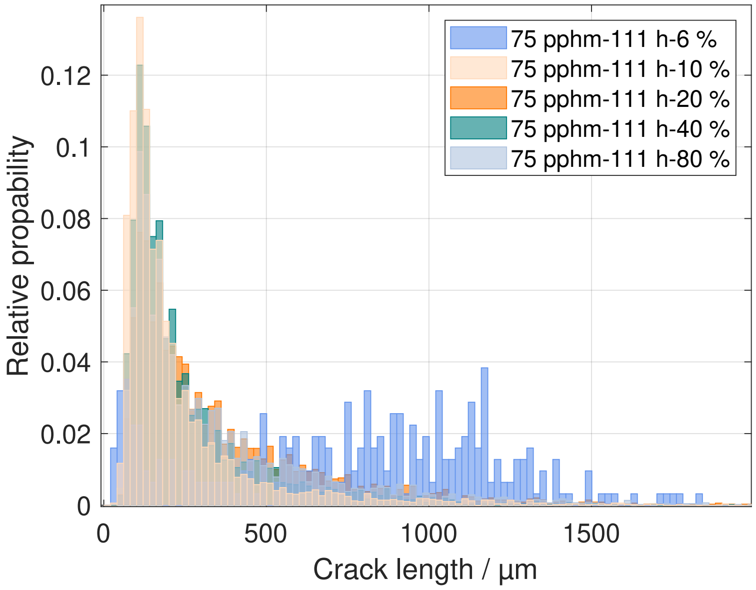

Figure 3.41 Normalised distribution of crack lengths for different ageing states ($c_{oz} - t_{\mathrm{a}} - \epsilon$).

Like the crack distance, the distribution of crack length stays similar above a level of 10 % tensile strain during ageing, as depicted in Figure 3.41 for 75 pphm. Only at the 6 % strain level, which has the least cracks in total, fewer, longer cracks are present compared to higher strain levels.

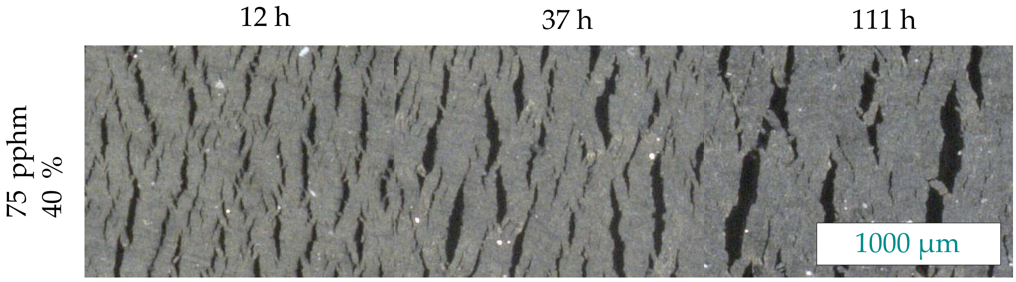

Figure 3.42 Surfaces of `C3` after ageing at 75 pphm under 40 % strain for different ageing times.

Regarding the evolution over time, an increase in crack intensity is observed (see Figure 3.42). Smaller cracks seem to vanish with ageing time or might stick closed as deeper cracks open in the vicinity. Another possible damage mechanism described by Charvet *et al.* [127] is the merging and growth of crazes to cracks. The absolute values of the crack distances also show an increase with ageing time, as depicted in Figure 3.43. This confirms the optical impression of the magnified surface images in Figure 3.42.

The images are also analysed regarding the cracked area, cracks per image,

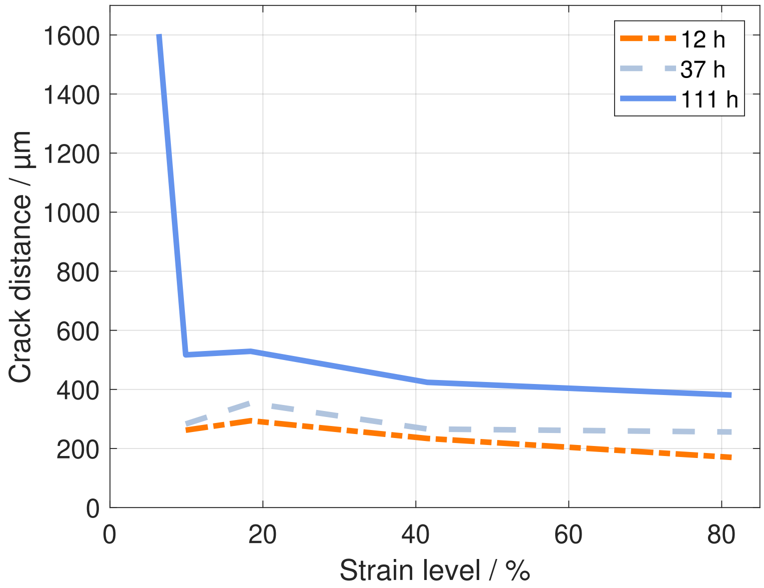

Figure 3.43 Mean crack distance for different strain levels and ageing times at 75 pphm ozone concentration.

and maximum crack length, as outlined in Table 3.4. However, the only parameter showing a trend with the strain is the cracked area per image that saturates at a level of about 11 % for the strain during ageing above 10 %. The maximum crack length and cracks per image do not correlate to the strain state.

Table 3.4 Change in the crack parameters with the strain level for 75 pphm ozone loading.

Strain / %	**6**	**10**	**20**	**40**	**80**
Cracked area / %	5.4	9.4	10.1	10.9	11.1
Cracks per image / -	17	189	349	246	
Maximum crack length / µm	2241	2313	2745	2075	2904

Comparison of Cracks Due to Fatigue Load and Ozone Load Regarding the crack surface and geometric propagation of cracks, fatigue cracks as reported in Beurrot *et al.* [74] show similarities to ozone-induced cracks. Compared to other elastomers, e.g. SBR, the heterogeneity of the microstructure of NR seems to be related to its SIC and strong crack growth resistance behaviour [1, 74], with both being special characteristics of NR as described in Section 1.3.1. Several features of the cracks are named by Beurrot *et al.* [74] and Flamm *et al.* [71]:

- Diamond-shaped zones
- Ligaments
- Branching and secondary cracks
- Zigzag crack growth for high dynamic strains

Figure 3.44 Crack tip structure after pre-ageing at 150 pphm ozone for 111 h under 30 % static strain.

Regarding the open crack tip as shown in Figure 3.44 for a buffer sample aged under static strain and ozone, ligaments and diamond shaped zones in the crack tip are visible. The unsteady fracture surface is also similar to the observations of Beurrot *et al.* [74]. Figure 3.45 shows the unsteady fracture surface in the cross-section of tensile samples of series `U` and `D` including branching. Even for short ageing times such as 4 h, branching starts to occur, regardless of the mode of strain. Numerous secondary cracks evolve next to the major crack after longer ageing times. Without dynamic loading during ageing, the crack geometry after ozone ageing seems to be similar to low dynamic strains in fatigue loading, as described by Beurrot *et al.* [74]. Even though the dynamic strains applied are large, the zigzag crack growth highlighted by Flamm *et al.* [71] only occurred in some cracks as shown in Figure 3.45b.

Crack Depth A minimum strain is necessary for cracks to evolve (see Figure 3.39) and thus the crack depth assessed by optical microscopy is analysed for static strain in ageing series `Z`, `U`, and `D` and dynamic strain in series `C`.

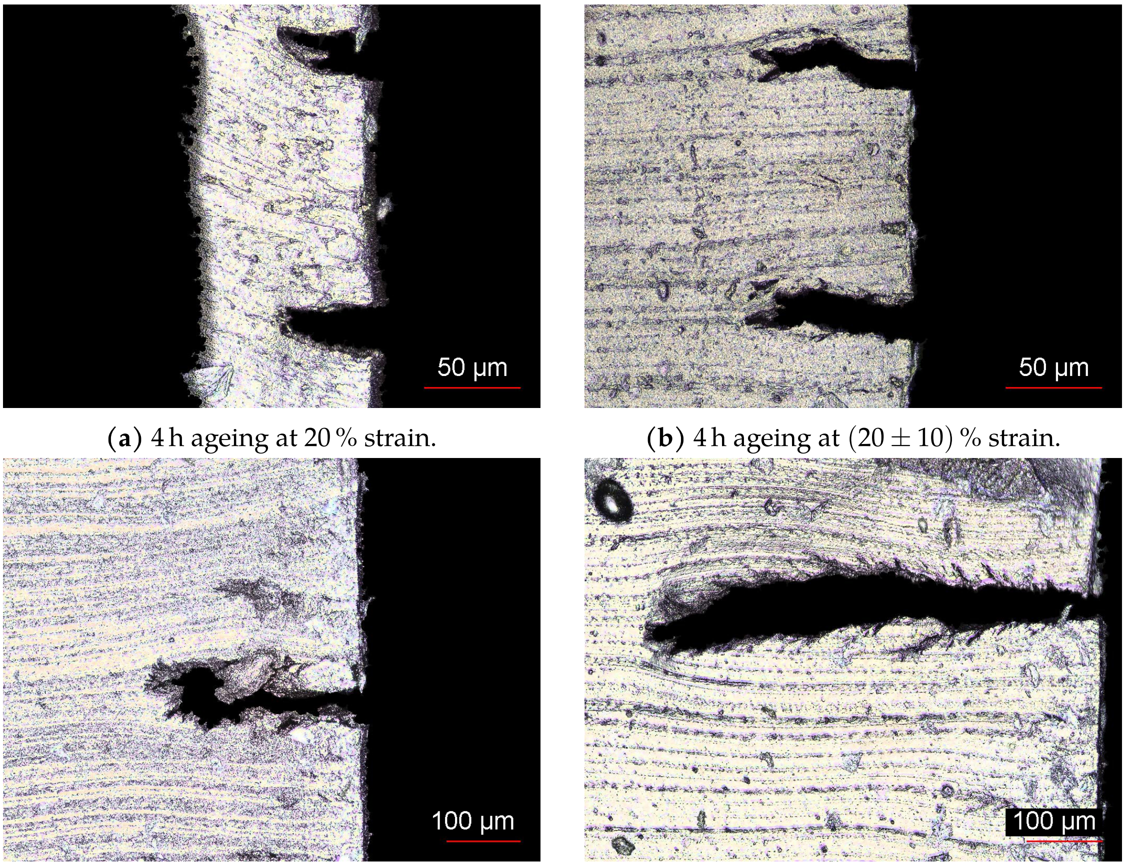

(**a**) 4 h ageing at 20 % strain. (**b**) 4 h ageing at (20 ± 10) % strain.

(**c**) 111 h ageing at 20 % strain. (**d**) 111 h ageing at (20 ± 10) % strain.

Figure 3.45 Branching of cracks at 75 pphm ozone concentration in tension bar samples.

Impact of Sample Thickness on Crack Depth Detection

Similar to the uniaxial tension tests, the impact of sample thickness on the crack depth result is analysed. Samples are tested in the range of 0.94 – 2.31 mm thickness in series `U` and `D`, as shown in Section 2.5. To check if the thickness has a significant influence on the crack depth measured by optical microscopy, samples of the two series are compared in Figure 3.46. The ageing states are all at 75 pphm ozone concentration, aged under 20 resp. 40 % strain for 12, 37, or 111 h. To avoid outliers, the average of the 10 maximal crack depths detected by microscopy is compared. Almost all samples show a crack depth that is independent of the thickness and the static deformation during ageing but dependent on the ageing time as in Figure 3.28. A slightly deeper crack is measured for the slimmer sample at the ageing state of 111 h at 75 pphm ozone, albeit only for 20 % strain.

Static Strain During Ageing

The number of cracks visible in the cross-section is small when close to the threshold strain for cracking, as observed for the surface cracks shown in

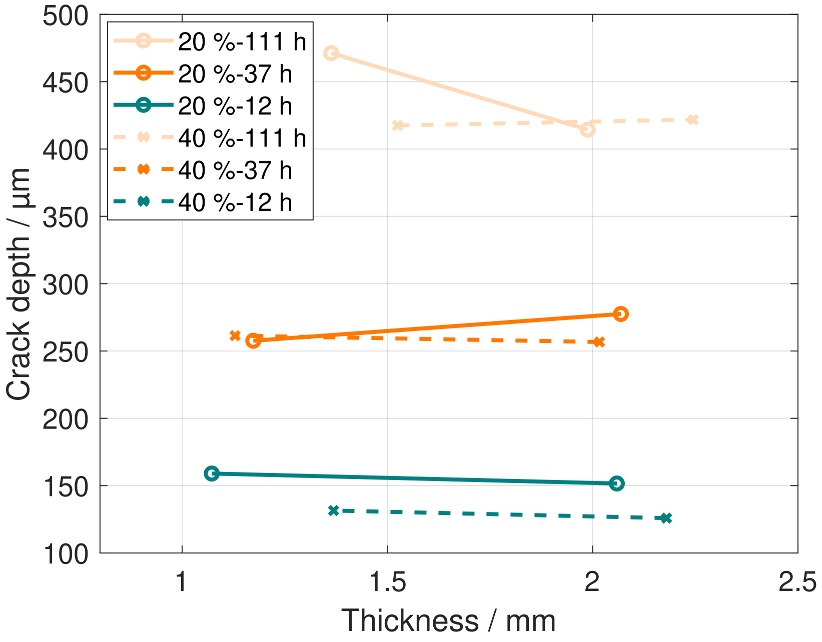

Figure 3.46 Average of the 10 largest crack depths measured by microscopy for samples aged at 75 pphm ozone under static strain ($\epsilon - t_\mathrm{a}$) each for two different sample thicknesses.

Figure 3.39 and Table 3.4. Regarding the maximum detected crack depths, the differences between 20 – 40 % strain are not consistent with the strain level, depicted in Figure 3.47, as indicated in Section 3.3.4 and Figure 3.29. Moreover, the average of the cracks measured shows no correlation to the strain levels. The maximum crack measured within 20 – 40 % strain, see Figure 3.47, is compared to the average of the three strain states by relating the total absolute difference to the average (values are provided in Table 3.5).

Table 3.5 Relative deviation in % of the maximum crack measured within 20 – 40 % strain to the mean.

		Ozone concentration / pphm			
		25	**36**	**52**	**75**
Ageing time / h	**4**	65	62	35	32
	12	28	40	25	6
	37	22	12	18	9
	111	10	15	13	11

Especially for short ageing times and low ozone concentrations, the relative deviation of the maximum to the mean is large. Concluding within this range, the height of static strain does not affect the crack depth. A decreasing crack

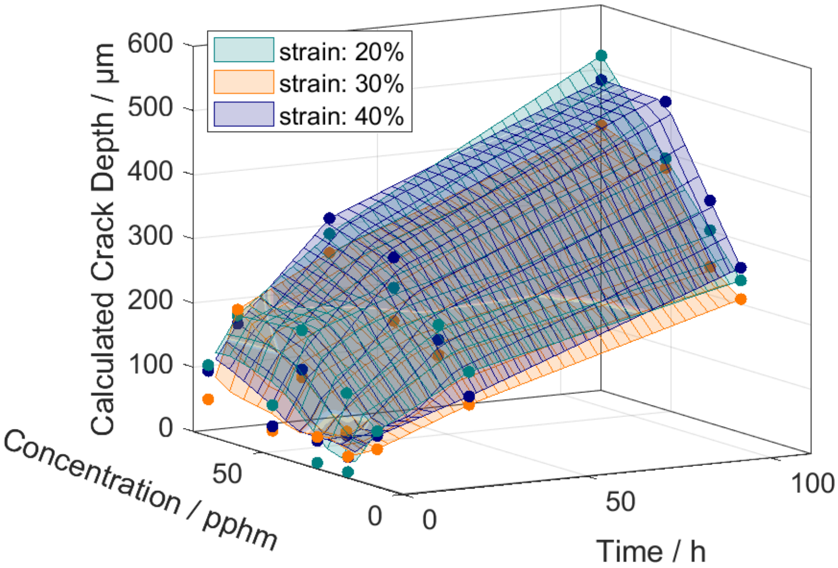

Figure 3.47 Measured crack depth for 20, 30, and 40 % static strain during ageing.

growth rate is observed with increasing ageing time and ozone concentration, as indicated in Section 3.3.4.

The maximal crack depths that are measured in different ageing batches are depicted in Figure 3.48. Apart from series `Z`, 2 sets of samples were aged in series `U` under 20 % strain with the different clamps described in Section 2.5. The clamping system does not impact the result markedly as the results of series `U` are similar. However, the large difference between the 2 series is unexpected. It might originate in the precision of the ozone control of the different climate simulator devices. In addition to the different devices employed, dog bone-shaped tension bars were used in series `Z` that were clamped in the shoulder section. Series `U` is conducted with bars of the same width over the height. Thus, the actual strain achieved in series `Z` might have been lower at the centre. However, considering Figure 3.50, even a reduction to 10 % strain should not result in such a difference in crack depth. Hence, the deviation of series `Z` and `U` seems to have originated in the different devices applied to conduct the artificial ageing.

To analyse the increase of crack depth with ageing time, Figure 3.49 considers two longer ageing times for the series `U` aged at UniBw with the ozone climate simulator by *Anseros*® at 25 pphm. The crack depth increases further after ageing times of 111 h and seems to settle after about 300 h at a maximum crack depth. Recalling Figure 3.47, the evolution with time seems to be consistent for all tested ozone concentrations.

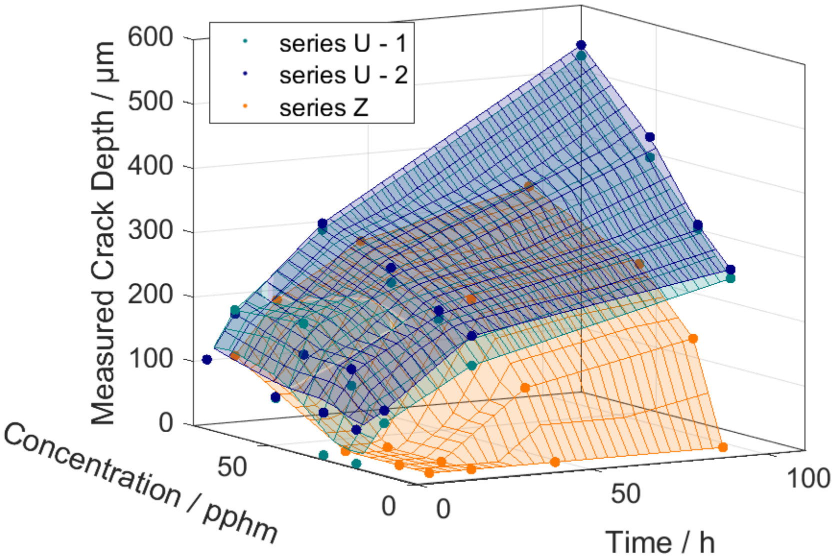

Figure 3.48 Comparison of different ageing batches at 20 % static strain during ageing.

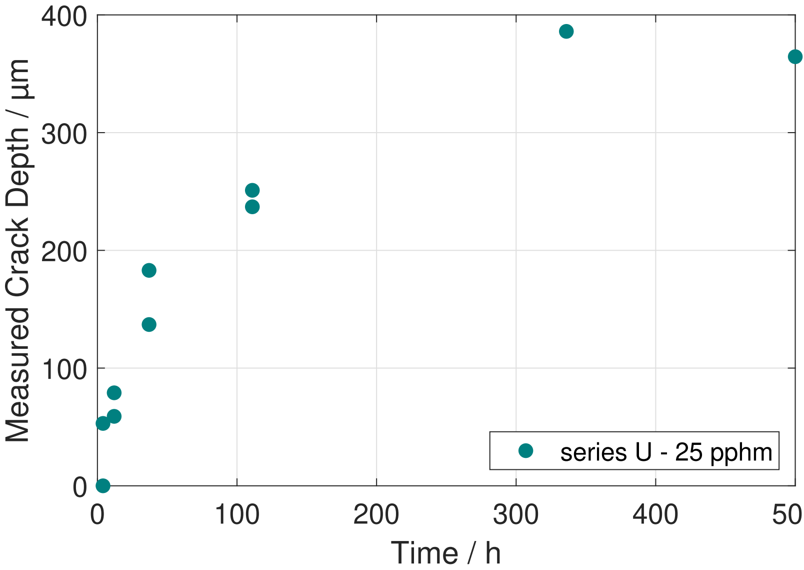

Figure 3.49 Measured crack depth for longer ageing times of series `U` at 25 pphm ozone with 20 % static strain during ageing.

Comparing a wider range of strain during ageing in series `D` and analysing the crack depth, a minimal necessary strain is detected, as shown in Figure 3.50. In contrast to Section 3.3.4 and Figure 3.30, no cracks are visible in the cross-section for the samples aged at 75 pphm below 6 % strain. The uniaxial tension tests showed a reduction in stress compared to the unaged sample, even for 0 % and 2 % at 75 pphm.

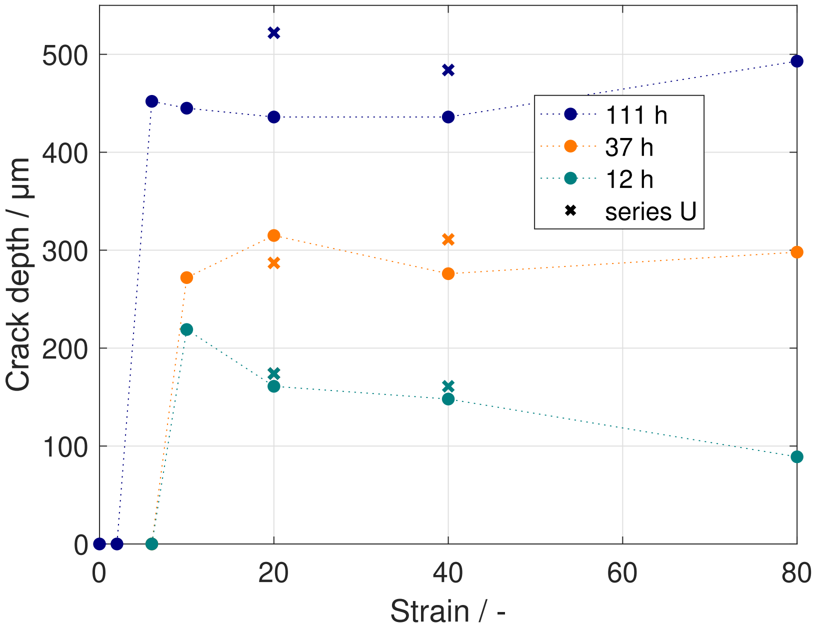

Figure 3.50 Measured crack depth over strain levels for different ageing times of series `D` at 75 pphm ozone with additional values of the same ageing state of series `U`.

Cyclic Strain During Ageing

In series `C`, cyclic strain was applied and the measured crack depth is depicted in Figure 3.51. In addition, the static 20 % and 30 % strain level is plotted to compare the influence of strain amplitudes to static strain. The strain amplitude of ± 10 % does not change the crack depth significantly. Whereas the amplitude of ± 20 % including a full deloading of the samples more than doubles the crack depth measured. The evolution of crack depth with time and with ozone concentration stays similar to that of static strain.

Comparison of Crack Evolution of `C1` and `C2` with `C3`

Since the formation of cracks could not be prevented by the regular antiozonants 6PPD and wax, the evolution of cracks including these additives is addressed. Regarding 20 % static strain, no cracks were observed for `C1` in series `Z` or `U`. Concerning most of the artificially aged samples, the measured cracks are deeper if the material contains 6PPD, as depicted in Figures 3.52 and 3.53. Regarding both series, for each only one single measurement state has a lower crack depth for `C2`. This finding indicates that adding 6PPD is not beneficial to prevent cracking or to reduce the crack depth under static strain.

Concerning cyclic loading, not even wax is sufficient to prevent cracking. However, Figure 3.54 shows a reduced crack size for the application of wax and 6PPD

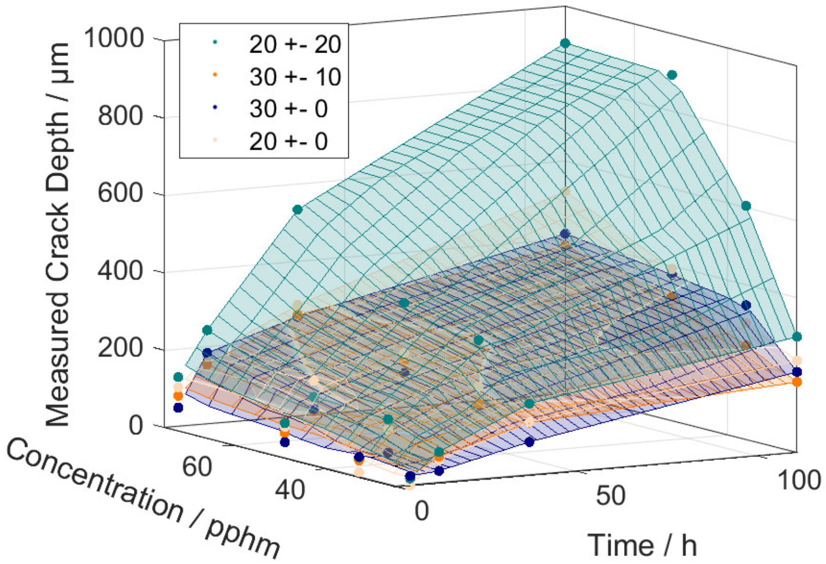

Figure 3.51 Measured crack depth for different strains and amplitudes of `C3`.

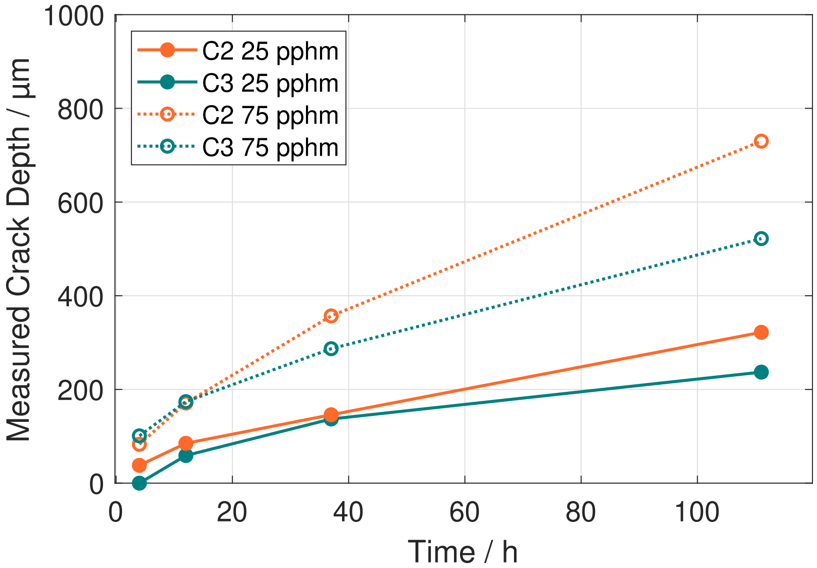

Figure 3.52 Measured crack depth for different material compounds in series `U` at 20 % strain.

below 45 h regarding 75 pphm and 110 h at 25 pphm. No cracks were observed at 25 pphm for about 40 h when applying wax and 6PPD. Nevertheless, for long ageing times, samples only protected by 6PPD show less deep cracks compared to the additional employment of wax. When speeding up the ozonolysis by increased concentration of 75 pphm after an ageing time of about 65 h, the unprotected NR has the shallowest cracks. This is expected to be similar for 25 pphm at very long exposure times. Even though cracks are completely prevented for short ageing times up to 40 h, at long ageing times both proctectants lead to a poorer crack growth rate under cyclic strain.

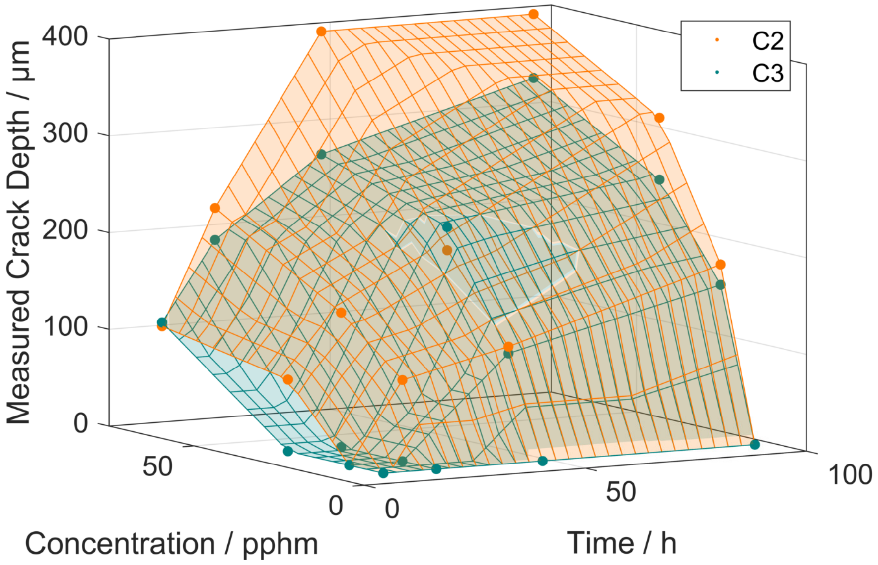

Figure 3.53 Measured crack depth for material `C2` and `C3` in series `Z`.

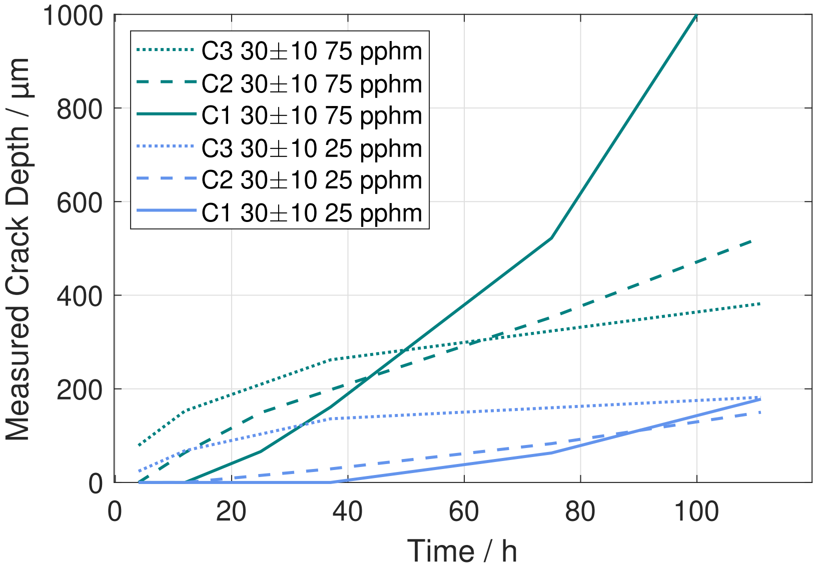

Figure 3.54 Measured crack depth for different material compounds in series `C`.

3.4 Discussion and Conclusions of Experiments

3.4.1 Light Ageing States and Different Ageing Devices

In general, for samples with short ageing times or at low ozone concentrations, the results display large deviations, and in some instances the change due to ageing is not visible at all. In chemical and thermal experiments, the change is not sufficiently apparent for the FT-IR and HotDisk®methods to detect it for the light ageing states. Regarding the mechanical experiments, the cracks observed are less numerous and less deep. In addition, the accuracy of the ozone climate simulator deviates by an absolute value of ±5 pphm resulting in a relative deviation factor of 0.5 to 1.5 at 10 pphm ozone concentration. Moreover, most ageing states are achieved in one ageing run of the ozone chamber and only few were conducted twice. Consequently, if a deviation occurs in the process it is present in all samples aged in the run. Three runs of samples of `C3` are aged under 20 % strain, of which two are conducted in the climate chamber by *Anseros*® and one in the chamber by *Gibitre*® (see Section 2.5). Between the crack depth of different samples in the *Anseros*® chamber, the deviation is only strong for short ageing times and low ozone concentrations, whereby even for intense ageing states the cracks measured after ageing in the *Gibitre*® device are approximately 1/3 smaller (see Figure 3.48). Consequently, the results from different devices are not comparable but it is recommended to strictly control the reliability of the ozone concentration achieved in measurement devices.

3.4.2 Ageing Without Deformation

Without strain during the ageing process, neither of the compounds, i.e. those with or without antiozonants, show visible cracks. Nevertheless, the experiments reveal changes after ozone ageing and FT-IR measurements directly resolve the change in the surface close layer. Regarding DSC and fatigue tests, changes in the thermal characteristics are measurable in the overall results of the aged specimens.

In FT-IR measurements (Section 3.2.1) on the surface, the spectra of all compounds changes after artificial ageing. However, only in `C3` does the carbonyl groups C=O, typical for oxidation processes, evolve. Related to the main chain vibrations, the carbonyl group is more pronounced due to ozone ageing compared to oxidative ageing at the same temperature of 40 °C. The literature-based assumption of a slow oxidative process in NR due to ambient air at 40 °C is confirmed.

Only slight differences are observed between the surface spectra of `C2` and

`C1`. However, both compounds show an increase of vibrations correlating to 6PPD on the aged surface. Even though no change of 6PPD content could be resolved in the cross-section, migration to the surface as shown by Lake and Mente [106] and others [4, 81] takes place.

In the cross-section, only for `C3` was the change in carbonyl groups relative to the main chain vibration deep enough to be detected. With 6PPD, the diffusion of ozone towards the core seems to be blocked completely as was the case for the compound with 6PPD and wax. The core of all samples showed no change after ozone exposure, suggesting that no ageing takes place at some diffusion-resistant depth depending on the antiozonant. In `C3`, the front line of carbonyl detected grows to the sample core with ageing time, already reaching the maximum depth at 37 h. With ageing time and with ozone concentration, the intensity of the relative carbonyl peak increases. Concerning the ageing states up to 111 h at 75 pphm ozone concentration, a maximum depth of 20 µm was measured. That penetration depth that was already reached for 75 pphm and 37 h and 52 pphm and 111 h. After the ageing time of 37 h, the fatigue tests also showed no decrease in the lifetime of samples statically deformed during the ageing process. This confirms the lifetime being not only dependent on the crack existing after the artifical ageing before the fatigue test. Both experimental results enhance the current understanding of the ageing process as being diffusion limited, and facing a maximal depth of change resp. crack dependent on the ageing duration.

DSC and *HotDisk*®measurements were employed to detect changes in the thermal characteristics on unstrained aged samples. Only the first measurement method was successful for `C3`. No significant changes are observed in `C1` and `C2` as the ageing depth seems too slight to gain a sufficient part of aged volume. Regarding `C3`, the specific heat capacity reduced for sufficient aged surface to volume ratio. Regarding the results of the FT-IR measurements, the surface close change is expected to span about 20 µm in depth. Even in `C3`, no change could be detected for bulk specimens with less surface to volume ratio. In conclusion, isolated aged material most probably changes to even lower specific heat capacities. Consequently, changes in the self-heating characteristics are expected although fatigue tests showed no differences in the temperature evolution between unaged and aged samples. Hence, either the aged surface layer or the change in thermal characteristics is smaller than the resolution of the temperature evolution measurement. However, even without strain during ageing, the average lifetime in fatigue tests is reduced. Overlapping with the span of measured lifetimes for pristine samples, the number of cycles endured in aged ones settles at the lower end of the range of pristine ones. The surface might homogenise due to the ozone loading so that more regular flaws initiate the fatigue crack leading to the more regular failure.

When viewing the surface under an optical microscope, after the ageing process a glossy sticky surface layer evolves in `C2` and `C3`. Containing wax, the matt surface stays similar before and after ageing in `C1`. Shallow cracks of a few µm depth evolve if deformation is applied after the unstrained ageing process, as shown by LSM measurements in Section 2.5. It is assumed that they correlate to a hardened surface layer. This aligns with the slight increase in density measured in Section 3.2.4.

3.4.3 Cracks – the Major Phenomenon Due to Ozone Ageing

In several experimental methods, the cracks after artificial ageing under strain are evident. The surface and cross-sections show visible cracks when magnified by an optical microscope. In addition to optical microscopy, tension tests show a decrease in stiffness with the ageing state that can be correlated to the missing cross-section due to the present crack depth. In comparison, the approach via optical microscopy delivers a smoother evolution of crack depth, although there is a limit to the number of cracks that can be detected via this method. If the cracks are too small to be measured with the microscope, a decrease in stiffness can still be measured in uniaxial tension tests.

Uniaxial tension tests on layers of aged samples (Section 3.3.4) and microhardness tests are consistent with two conclusions. First, `C3` shows diverging behaviour compared to unaged samples up to a limit of approximately 300 µm for series `Z`. Second, the sample centre is not influenced by the artificial ozone ageing under static strain. In addition, only `C2` and `C3` crack under static strain during ageing whereas `C1` does not show any cracking for the static strain applied during ageing.

Surface

The cracked area and distribution of crack lengths and distance in the surface stagnates with a strain level above 10 %, as shown in Figures 3.39, 3.40, 3.41 and 3.43. In contrast, with the ageing time the crack distance increases (Figure 3.40) like the crack depth does (Figure 3.46). As Flamm *et al.* [71] describes for fatigue cracks, the crack opening relaxes the region above and below it, which might also explain the increased distance between cracks with ageing time. As cracks grow deeper, straining the cracked sample during ageing or viewing under the microscope, deep cracks open which subsequently relax the more shallow ones that might stay closed, as indicated in Figure 3.42.

Thickness of Samples

To conclude the analysis via both approaches to detect the crack depth shown in Section 3.3.5, Figure 3.46, and Section 3.3.4, Figure 3.28, no significant influence of the sample thickness on the crack depth could be observed. The microscopic approach (Figure 3.46) considering the 10 largest cracks observed, shows even less of a difference than the calculated crack depth by uniaxial tension tests.

Crack Detection Methods

Two methods are employed to analyse the crack depth, namely tension tests on bars (Section 3.3.4) and optical microscopy in the cross-section (Section 3.3.5).

The range of crack depths measured with the microscope covers approximately 300 μm. An inhomogeneous cracking front is present, reflecting the inhomogeneous surface crack pattern and the irregular ripped off surface layer during sample preparation for microhardness. In contrast, the crack depth analysed via tension tests finds one crack depth per sample as it assumes a constant crack depth. The cracks in the two sample sides are approximated as being homogeneous in the tension test approach, whereby the maximum crack depth detected is higher for the microscopic approach.

Regarding little static strain during ageing, a more than 100 μm difference separates the two approaches in Figure 3.29, and 3.47. However, with increasing static strain levels (see Figure 3.30, and 3.50), the overall maximum crack depth detected is similar in both methods.

As an example, the crack depth over ageing time at 75 pphm in Figure 3.55 shows the gap between the detected crack depth value via microscopy versus via cross-section reduction in uniaxial tension tests. Nevertheless, the evolution over ageing time and concentration of ozone is alike in both methods.

Cracks Below Surface

In many samples’ cross-sections, below-surface-cracks appear in between deep cracks as depicted in Figures 3.56 and 3.57. When the crack depth is measured like the ageing time, the appearance of these below-surface-cracks becomes more prominent, which could be due to several reasons. Firstly, a given crack might grow sideways at the tip below the surface but in contact to the ambient air.

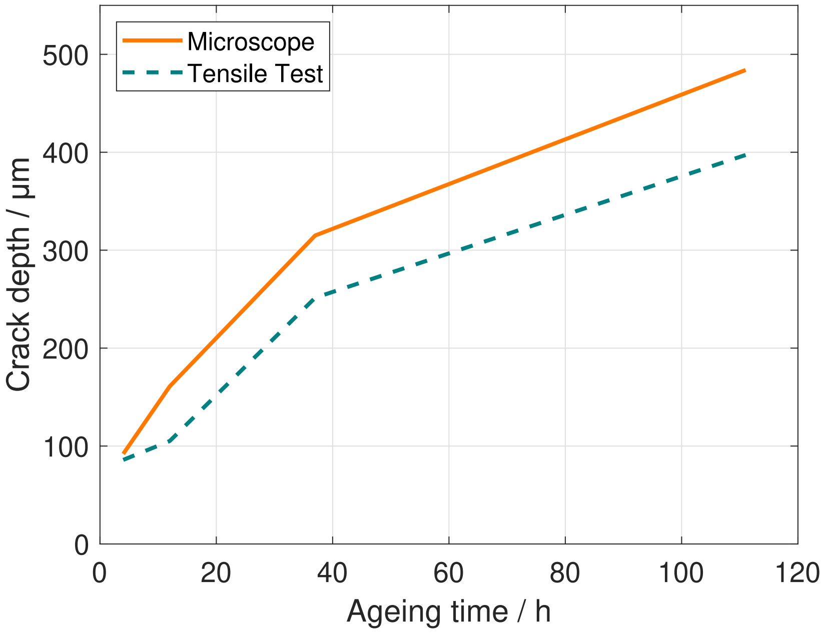

Figure 3.55 Crack depth calculated via tension tests and measured by microscopy after ageing at 75 pphm and 40 % static strain.

Secondly, strain is applied to open the cracks to be visible under the microscope, consequently relaxing the surface in between. The adhesion of crack surfaces of in-between cracks might be strong enough to keep them closed at the surface. In concordance to the surface of `C3` appearing sticky after ageing, the adhesion of crack surfaces under strain is more pronounced than for `C1` and `C2`. Thus, the second assumption seems to be more probable.

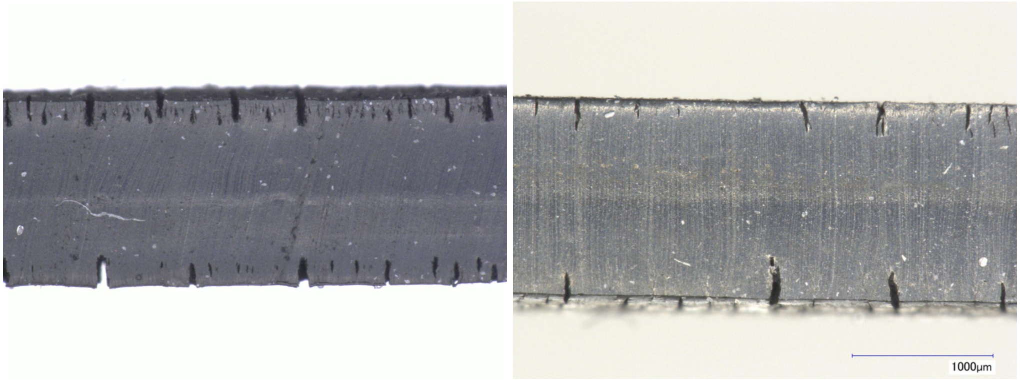

Figure 3.56 Cracks below surface, static strain during ageing of 20 % strain, 25 pphm for 111 h; **Left**: `C3`; **right**: `C2`.

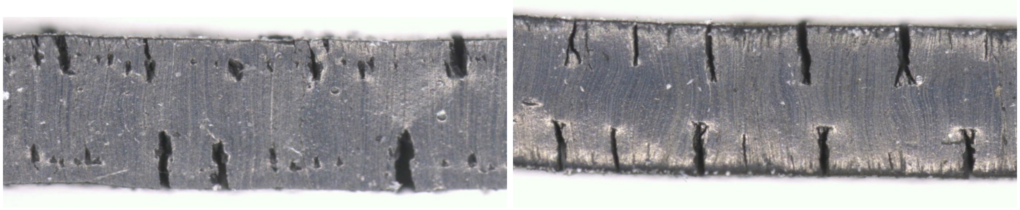

Figure 3.57 Cracks below surface after dynamic strain during ageing of 12 ± 5% strain, 52 pphm ozone for 111 h; **Left**: `C3`; **right**: `C2`.

Static Strain During Ageing

Strain during ageing forces rubber to crack fast under ozone loading. A threshold strain is necessary for cracks to evolve, although higher strain levels do not clearly emphasise the crack depth (see Figure 3.39, and 3.50). In series `U` with between 20 and 40 % strain, no correlation between strain level and crack depth is detected. The wider range in series `D` of up to 80 % strain similarly does not give reason to see a dependence of the crack depth on strain as long as a critical minimum strain is given. Depending on the ageing time, the critical minimum strain lies between 2 and 10 % of static strain. As vulcanised rubber consists of twisted, entangled, and interconnected molecules, scissions in the main chain lead to contraction of the remaining parts. If strain is present, more energy is available for contraction and new, pristine surface is exposed for further electrophilic addition of ozone. In contrast, without strain, the products of the scissioning block further attacks physically, corresponding to the layer of limited depth measured by FT-IR in Section 3.2.1. The hypothesis is illustrated in Figure 3.58.

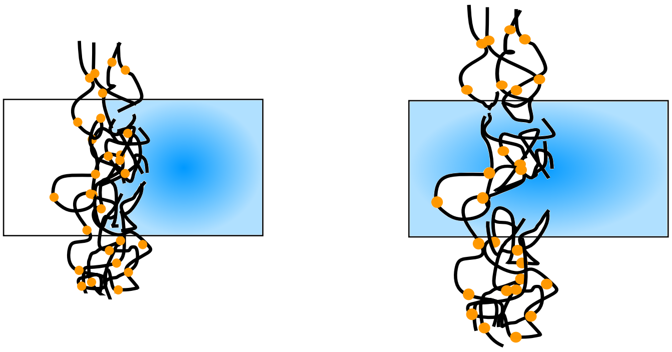

Figure 3.58 Schematic scission and exposition of new surface with double bonds (orange dot) in the unstrained (left) and strained (right) state.

In conclusion, the cracks are strongly dependent on the presence of strain during ageing, whereas the strain level loses importance once the threshold level is passed.

Influence of Ageing Time and Ozone Concentration

The evolution of the crack depth measured by means of optical microscopy for series `U` is plotted in Figure 3.59 over time and in Figure 3.61 over ozone. As no correlation between crack depth and static strain has been derived, the strain levels are not separated here.

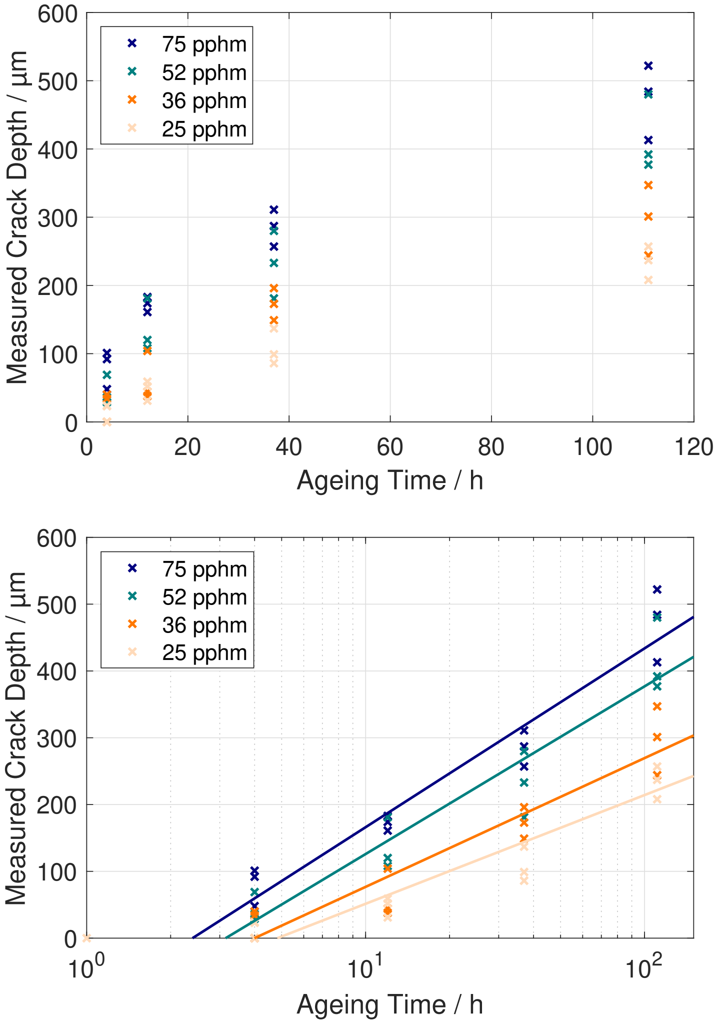

Figure 3.59 Evolution of crack depth for series `U` with time.

In Figure 3.59, the crack data of series `U` is plotted on a logarithmic scale confirming an approximately linear, logarithmic dependence on ageing times as suspected based on literature alike Ehrenstein and Pongratz [86]. Even for the additional ageing times of 336 h and 500 h at 25 pphm under 20 % strain, shown in Figure 3.60, the linear, logarithmic correlation between the crack depth and ageing time is a good approximation. A limited crack depth seems to be approached for each ozone concentration viewing the linear time scale in Figure 3.59, although it is not reached after 111 h. With rising ozone concentrations, the onset of cracking starts earlier.

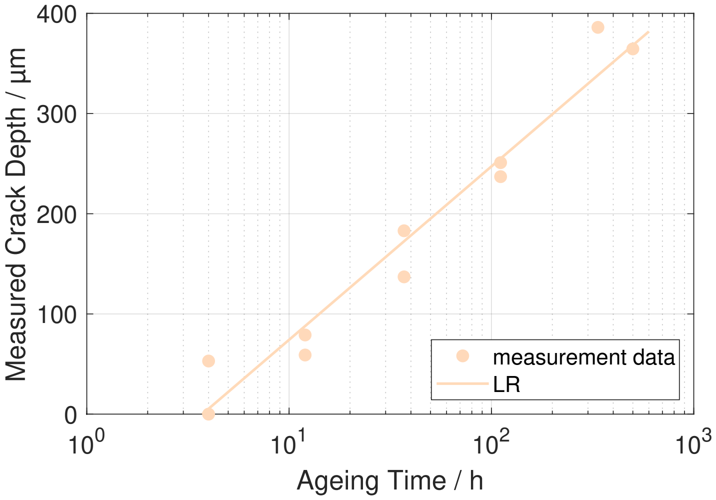

Figure 3.60 Evolution of crack depth for series `U` under 20 % strain with additional times tested at 25 pphm.

The evolution of cracks with increasing ozone concentrations of up to 52 pphm seems to be linear, albeit on linear scale as stated by Braden and Gent [65] and Gent [20] (see Figure 3.61). Concerning 75 pphm, the rate of crack growth with ozone concentration slows down and does not follow a linear path anymore.

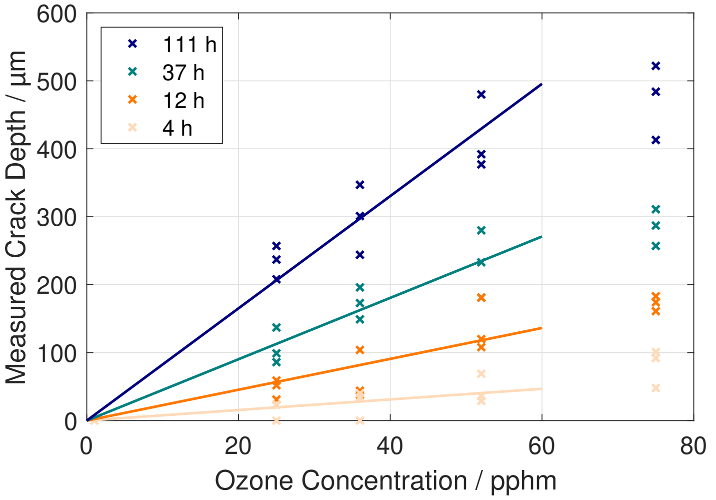

Figure 3.61 Evolution of crack depth for series `U` with ozone concentration.

Application of Antidegradants

Without strain, both antiozonants prevented chemical changes in the cross-section as the FT-IR measurements have shown. However, the degradation depth is limited even without the application of these antiozonants.

No cracks occurred for static strain if wax is part of the compound. However, this was not observed when applying cyclic strains during ozone exposure, as shown in Figure 3.54. The protective layer of migrated wax is ruptured due to the mechanical loading leading to higher cracks than the compounds without wax for long ageing times. The compound with only 6PPD as protectant also shows deeper cracks than the unprotected compound for both static and cyclic strain at longer ageing times, as shown in Figure 3.52, and 3.53. Even if the maximum cracks for long ageing times exceed the levels of unprotected rubber, Figure 3.54 shows the benefit of the antiozonants at low ozone concentrations and cyclic strain during ageing. The antiozonants delay the onset of cracking and slow the evolution of cracks up to the break-even point with `C3` at longer ageing times. At ground level, the ozone concentration is usually below 15 pphm which is especially beneficial for the ageing time until the break-even point is reached. In addition, if no cracks are tolerated, the time until the first cracks appear will be prolonged by the application of wax and 6PPD together.

Another result of adding antiozonants to the compound is a homogenisation of cracks, revealed in the cross-section of samples prepared for microhardness, Figure 3.13, and the microscopic image of the crack depths in the cross-section shown in Figure 3.56, and 3.57.

Hence, if cracks are tolerable but should reach a maximum level, no additives should be employed. To reduce the cracks at the beginning of the ageing process up to a limit in time, the combination of both antiozonants is advisable. When only static strain is expected in application, wax might prevent cracking if suited to the application conditions.

Lifetime under Fatigue Load

The degradation due to ozone ageing reduces the lifetime under fatigue load tested for material `C4`, including 6PPD and wax. Pristine samples fail at flaws induced in the production of the buffer and the range of achieved lifetimes covers 80 – 130 % of their average lifetime. After ageing, the early failure seems to be correlated to the degradation, i.e. the crack status after the ageing process.

The average lifetime of unstrained aged samples is at the lower end of the range of the pristine samples' lifetimes. The surface flaws seem to homogenise due to the ageing process, resulting in little spread in the measurement data.

Straining the samples during ozone ageing to 40 % reduces the lifetime by half. The crack initiation also starts at different flaws than the production seam. Hence, some cracks present a more severe flaw in the surface than the production seam. In comparison to series `C`, cracks are visible in the surface, see Figure 3.16, even though wax is part of the compound.

Ultimately, the application of cyclic strain of up to 30 % leads to a failure at 1/6 of the lifetime of a pristine sample. The cracks that are present after ageing must be deeper than the tensile deformation at the start of the fatigue measurement, see Figure 3.21, which is higher than for static strain.

After a 40 h ageing time, the maximal reduction for static strain seems to be reached for all tested ozone concentrations. The tensile deformation at the start of fatigue loading also stays constant with increasing ageing time. With increasing ozone concentration, the lifetime does not reach a minimum within the parameters tested. Even though a simple correlation between lifetime reduction and crack depth seems to be present regarding ageing times, this cannot be stated for increasing ozone concentrations.

Cyclic Strain During Ageing

Samples exposed to cyclic strain during ageing show a strong dependence on the different strain amplitudes applied, in contrast to the static strain. Cyclic loading between 0 – 40 % strain during ageing results in maximum crack depths that are more than double the value compared to the cyclic load between 20 – 40 %. The latter is close to static load levels of 20 % or 30 % strain (compare Figure 3.51). Aside from the higher amplitude, the relaxation to the initial state might lead to less energy being necessary for the tearing process, detected by Lindley [96] in case of unaged NR. In fatigue tests, the cyclic load during ageing between 0 – 30 % resulted in more than a halving of the lifetime compared to static strain. No purely mechanical crack growth is expected by the cyclic loadings, since the crack depth for the 20 – 40 % cyclic strain is not increased compared to that of the static strain. However, in both experiments, the amplitudes including the initially unstrained state lead to the most severe degradation. Applying the amplitude to the strained state and not allowing relaxation seems to capture positive effects such as SIC, thereby slowing the crack growth process [96].

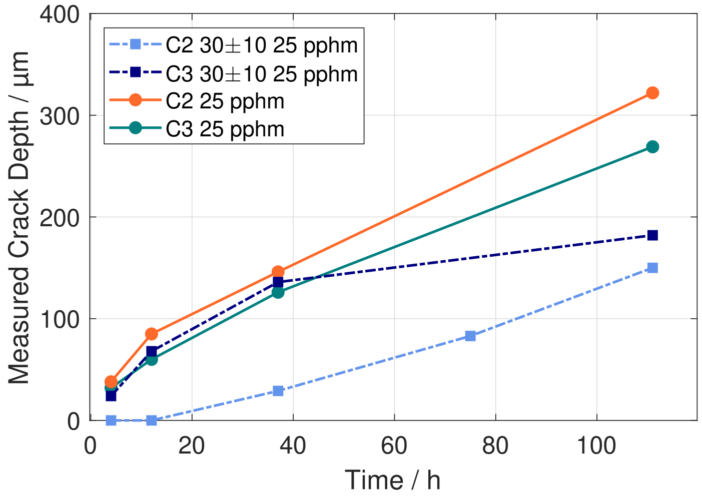

Figure 3.62 Crack depth in `C2` and `C3` under static strain and cyclic strain between 20 – 40 %.

Comparing the crack depth after static and cyclic strain, see Figure 3.62, in `C2` the cyclic loading helps the migration of 6PPD and leads to a reduction of crack growth until it is consumed. However, even in `C3`, the application of the amplitude not reaching the initial unstrained state leads to shallower cracks than static strain does.

3.4.4 Types of Damage Due to Ozone

In conclusion, regarding the damage evolution two types are observed as stated in Section 1.3.6:

- Change of outer layer without strain during ageing
- Cracking from the surface towards the centre given a threshold strain is exceeded

The methods applied for detecting a changed layer are FT-IR (Section 3.2.1), DSC (Section 3.2.2), HotDisk® (Section 3.2.3), gas pycnometer (Section 3.2.4), and microhardness (Section 3.3.2). None of the methods is able to detect an evolution of changed layer depth with the resolutions achieved. Thus, the second damage type of cracking is selected to develop the evolution of a damage parameter for ozone-aged NR. Besides tension tests on bars (Section 3.3.4) optical microscopy of the cross-section (Section 3.3.5) revealed and evolution of crack depth.

Das Leben muss nicht einfach sein, vorausgesetzt, es ist nicht leer.

Life need not be easy, provided only that it is not empty.

— Lise Meitner

4

Evolution Equation for the Crack Depth

Contents

4.1 Motivation and Analysis of Ageing Parameters

Regarding the process of ozone attack as a closed system to be phenonomenologically described, cracks appear due to double bonds being split under strain. As indicated in the conclusions in the experimental part (Section 3.4), several parameters influence the crack evolution, particularly the ageing time and ozone concentration. In contrast, the static strain during ageing is essential for cracks to evolve but after passing a threshold level, its influence is limited and can be considered together. The measured crack depths vary greatly with cyclic strain during ageing reaching the unstrained state, and thus they will be viewed separately from static strains. Additionally, antiozonants lead to different evolutions of crack depths for `C2` and `C1`. The databases that were considered separately in the following are named in Table 4.1.

Table 4.1 Databases for separate evolution equations.

Database	Strain	Compound	Series
`C3stat`	static	`C3`	`U`
`C3cyc30`	$30 \pm 10\,\%$	`C3`	`C`
`C3cyc20`	$20 \pm 20\,\%$	`C3`	`C`
`C2stat`	static	`C2`	`U`
`C2cyc30`	$30 \pm 10\,\%$	`C2`	`C`
`C1cyc30`	$30 \pm 10\,\%$	`C1`	`C`

To motivate a simulation for the evolution, the kinetics of a monomolecular reaction are analysed. Subsequently, the evolution over ageing time and over ozone concentration are viewed separately. Further, an initial time to cracking and possible influences of changing diffusion characteristics for consecutive ageing sequences are taken into account.

4.1.1 Kinetics of a Monomolecular Reaction

Some authors [23, 90] assume a monomolecular function as a basis for the evolution of ageing with time, and the kinetics of such a reaction is derived in the following.

It should be noted that this is not representative of the actual reaction of ozonolysis of NR. Nevertheless, one phenomenological description of the correlation between ozone ageing and the growth of crack depth is motivated by a monomolecular reaction:

$$\mathrm{A} + \mathrm{B} \rightarrow \mathrm{C} \tag{4.1}$$

The double bonds in the NR are correlated to the first reactant A and their scissions are considered proportional to the crack depth. Murphy and Orr [23] and Dakin [90] simulated scissions in molecule chains leading to macroscopic damage with monomolecular reactions, as mentioned in Section 1.3.6. The attacking ozone is considered to be reactant B, with the reaction resulting in product C. Intermediate steps of the ozonolysis are neglected and the same stoichiometric coefficients are assumed. Based on Latscha and Kazmaier [128] and Baerns *et al.* [129], in a first-order reaction of two reactants to one product, the concentration c in mol/m^3 of the reactants changes with reaction time t in min and thus leads to a differential equation for the reaction velocity v in mol/m^{3}min, depending on a factor k in min^{-1} and the change in concentration of reactant A.

$$v = -\frac{dc_{\mathrm{A}}(t)}{dt} = \left(-\frac{dc_{\mathrm{B}}(t)}{dt} = +\frac{dc_{\mathrm{C}}(t)}{dt} = \right) k \cdot c_{\mathrm{A}}(t) \tag{4.2}$$

Considering all assumptions, a time-dependent evolution of the concentration of A can be derived, converting Eq. (4.2) to:

$$-\frac{dc_{\mathrm{A}}(t)}{c_{\mathrm{A}}(t)} = k \cdot dt \tag{4.3}$$

Integration of Eq. (4.4) leads to

$$\begin{aligned} -\int_{c_{\mathrm{A0}}}^{c_{\mathrm{A}}(t)} \frac{1}{c_{\mathrm{A}}(t)} dc_{\mathrm{A}}(t) &= k \int_{t_0}^{t} dt \\ -\left[\ln(c_{\mathrm{A}}(t)) - \ln(c_{\mathrm{A0}})\right] &= k \cdot (t - t_0) \\ -\ln(c_{\mathrm{A}}(t)) - \ln(c_{\mathrm{A0}}) &= -k \cdot t \\ \frac{\ln(c_{\mathrm{A}}(t))}{\ln(c_{\mathrm{A0}})} &= -k \cdot t \end{aligned} \tag{4.4}$$

$$c_{\mathrm{A}}(t) = c_{\mathrm{A0}} \cdot e^{-k \cdot t} \tag{4.5}$$

The result is an exponential decay of the concentration of reactant A with c_{A0} being the initial concentration of reactant A, quantitatively depicted in Figure 4.1.

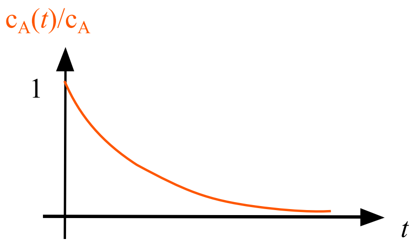

Figure 4.1 Quantitative sketch of the exponential decay of reactant A.

As the concentration of reactant A is correlated to the available double bonds $c_{\mathrm{db}}(t)$, the amount of scissions $c_{\mathrm{sc}}(t)$ is defined as:

$$c_{\mathrm{sc}}(t) = c_{\mathrm{db},0} \cdot (1 - e^{-k \cdot t}) \tag{4.6}$$

and qualitatively depicted in Figure 4.2a with the maximal amount of scissions equal to the total amount of double bonds $c_{db,0}$ exposed to ozone. Assuming an evolution of the crack depth $h_c(t)$ directly correlated to the scissions, one obtains a possible evolution of crack depth over time with a maximum value of $\max(h_c)$, as shown in Figure 4.2.

$$h_c(t) = \max(h_c) \cdot (1 - e^{-k \cdot t}) \tag{4.7}$$

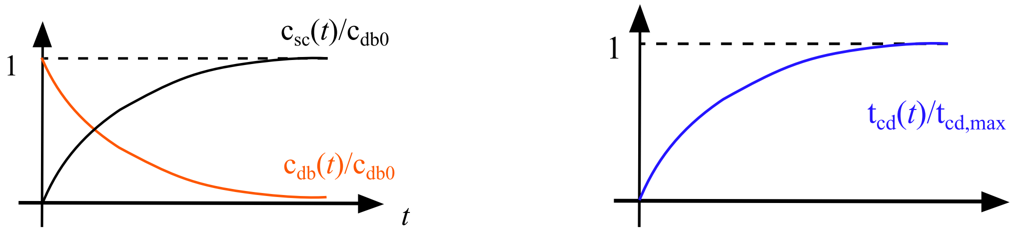

(**a**) of scissioned double bonds. (**b**) of crack depth.

Figure 4.2 Quantitative evolutions.

4.1.2 Weighting Measurement Data

To account for measurement errors, the crack depth data is weighted in all simulations as described in the following. Several factors might cause the scatter in the cracking depth measured:

1. Variance in the raw ***material*** and production accuracy: Regarding series `U`, `D`, and `C` all samples are from the same batch. Differences might be present in the surface homogeneity of each vulcanized plate, flaws, agglomerations in the bulk, and other differences from the natural material and the process to the vulcanized product. Concerning series `Z` and `F` different batches are used, for the latter even a different compound. Nevertheless, these inaccuracies can hardly be quantified and thus are not included in the weighting.

2. Crack depth ***measurement*** under the microscope: As described in Section 3.3.5, the crack depth in the cross-section is measured in the microscope software with a standard deviation of 12.4 µm. In total, a maximal deviation

of ±25 µm was measured. Thus, the cracks are weighted by 25 µm/h_c, with h_c being the crack depth in µm.

3. Regarding the ***ageing time***, artificial ageing in the ozone chamber requires a pre- and post-conditioning phase of 0.5 h for the temperature and humidity to be set, whereas the ozone level is reached within a few minutes. The potential deviation in ageing time is accounted for with 0.5 h/t_a, where t_a is the ageing time in h of the sample.

4. The ozone chambers must monitor the ***ozone*** level rapidly, for which only an accuracy of ±5 pphm is realistic. This markedly affects the crack depth and the weighting is ±5 pphm/c_{oz}, with c_{oz} in pphm being the ozone level of the sample.

To weight the simulations, a weighting function W is formulated:

$$W(t_a, c_{oz}, h_c) = \frac{1}{\frac{0.5}{t_a} + \frac{5}{c_{oz}} + \frac{25}{h_c}} \tag{4.8}$$

The measurement uncertainties are absolute values. The relative scatter in crack depth is thus more intense for low ozone concentrations as for short ageing times. Their importance is reduced in the simulation by the weighting function.

Regarding some repetitions of ageing sets, the measurement accuracy of ozone seems to have the strongest effect on the crack depth. The maximal crack measured varied by 10 % after 52 pphm for both 37 and 111 h ageing time. However, at 36 pphm, the repeated ageing set was 20 % off the first ageing for both ageing times.

4.1.3 Evolution over Time

To test the correlation between ageing time and crack depth, Pearson's and Spearman's correlation coefficients (r_P resp. r_{Sp}) are calculated and their significance levels (p_P resp. p_{Sp}) to evaluate the null hypothesis, which is provided in Table A.2 in the appendix. Pearson's correlation is a measure for the linear relation between the variables [130, 131], whereas Spearman's correlation is based on ranks and therefore able to detect different monotonic relationships [131]. In addition, the cosine similarity (r_{cos}) is given, indicating a general similarity between the correlating datasets of ageing time and crack depth. It is usually used to find similar objects in text analysis or picture analysis but also in biomedical engineering [132]. The range of the cosine similarity is from -1 to 1, as it is calculated by the inner product of two vectors divided by the product of their norms [133]. Thus, if the vectors enclose a small angle due to their similarity, the result is close to 1. When normalising the crack data to the longest ageing time, very high correlations are calculated as shown in Table A.4. The correlation between the ageing time and crack depth is significant, as the p-values are lower than 5 % and the r-values above 70 %. The Spearman's correlation yields higher values than Pearson, whereby the visual impression of a nonlinear but monotonic relation is confirmed.

Regarding the evolution of cracks with ageing time, different models are used to simulate the evolution:

- `EXP`: the exponential decrease of available rubbers based on a monomolecular first-order reaction
- `LIN`: the logarithmic linear approach on the time scale postulated by Ehrenstein and Pongratz [86]
- `LN+`: a modified logarithmic function, and
- `POW`: the power law (when including antiozonant wax)

Matlab by *MathWorks*® is applied to fit the parameters of the four functions to the measured crack data. A linear least-squares algorithm is used with the least absolute residual method including the custom weighting function Eq. (4.8) described above. To compare the fits with each other, the root mean square error (RMSE) is used [130].

No Antiozonants

Static Strain – `C3stat` Without antiozonants, the evolution over time shows a reduction in crack growth rate for all experiments. This observation is in contrast to the constant crack growth velocity postulated by e.g. [2, 51]. A stagnation of crack growth is modelled by the exponential equation (`EXP`, Eq. (4.9)), motivated by the kinetics of a monomolecular reaction. However, comparing simulations for the ozone level of 25 pphm, including and excluding the additionally examined longer ageing times of 336 and 500 h, shows that the final crack depth simulated by parameter $h_{c,\max}$ is dependent on the deepest crack measured. Thus, if the crack depth still grows as it does for 25 pphm with `EXP`, the cracks are underestimated, as shown in Figure 4.3. Therefore, the stated logarithmic linear evolution (`LIN`, Eq. (4.10)), see Section 3.4.3 and a shifted logarithmic function (`LN+`, Eq. (4.11)) are compared in Figure 4.3 to the approach with `EXP` regarding the data of series `U`:

$$\texttt{EXP:} \qquad h_c^{\texttt{EXP}}(t_a) = h_{c,\max} \cdot (1 - \exp(-\mathrm{k} \cdot t_a)) \tag{4.9}$$

$$\texttt{LIN:} \qquad h_c^{\texttt{LIN}}(t_a) = \mathrm{p} \cdot \ln(t_a) + \mathrm{q} \tag{4.10}$$

$$\texttt{LN+:} \qquad h_c^{\texttt{LN+}}(t_a) = \mathrm{m} \cdot \ln(\mathrm{s} \cdot t_a + 1) \tag{4.11}$$

Each equation is dependent on time t and has two parameters to fit, namely the maximal crack depth $h_{c,\max}$ in µm and the reaction velocity k in h^{-1} which are known from Section 4.1.1. In contrast, the other parameters p in $\mu\mathrm{m}\,\mathrm{h}^{-1}$, q in µm, m in µm, and s in h^{-1} do not have a direct physical meaning.

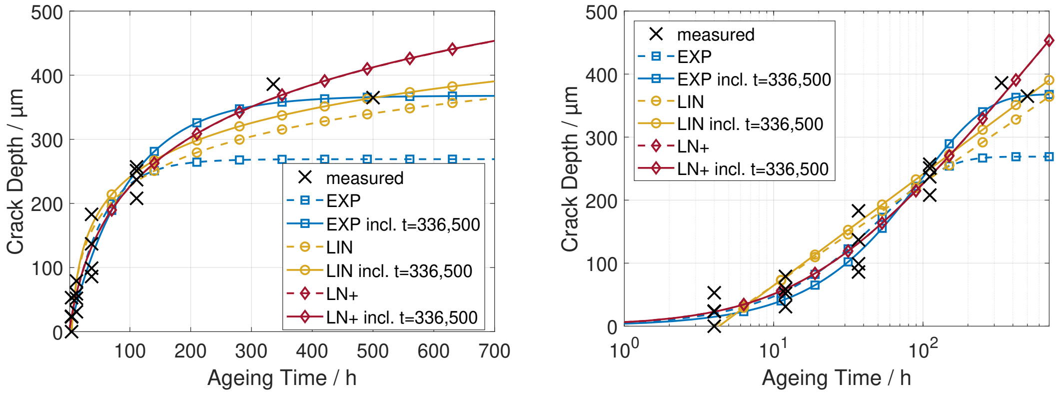

Figure 4.3 Comparison of different evolution equations for the crack depth over time in series `U` for 25 pphm.

Table 4.2 Fit parameters for the evolution of crack depth over time in series `U` for 25 pphm displayed in Figure 4.3.

Simulation	**Long ageing time**			
`EXP`		$\max(h_c)$	k	RMSE
	yes	3.86×10^2	1.03×10^{-2}	59.1
	no	2.69×10^2	1.93×10^{-2}	57.0
`LIN`		p	q	RMSE
	yes	7.67×10^1	-1.12×10^2	82.1
	no	7.05×10^1	-9.77×10^1	74.0
`LN+`		m	s	RMSE
	yes	1.27×10^2	4.94×10^{-2}	59.8
	no	1.27×10^2	4.93×10^{-2}	55.9

Although the logarithmic linear approach could model an initial time until cracking starts, the residual plot reveals a bad simulation as does the plot on a logarithmic timescale (Figure 4.3). Moreover, the RMSE, which is shown in Table 4.2, is similar for `EXP` and `LN+` but worse for `LIN`. Like `EXP`, `LIN` underestimates the crack depth for the additional longer ageing times, even when including them into the simulation. `LN+` and `EXP` show similar evolutions of crack depth for shorter ageing times up to 111 h. A remarkable aspect of `LN+` is the indifference of the simulation to the inclusion of crack data for long ageing times (see Table 4.2). Regarding the benefits and drawbacks of the discussed evolution equations, `LN+` is chosen to simulate the crack depth with time to rather overestimate the long-term crack depth.

Consequently, for the higher ozone concentrations, the simulation with `LN+` is conducted regarding the measurement data available up to 111 h ageing time, as shown in Figure 4.4(right) and Table A.5 in the appendix. Regarding the evolution of the parameters in `LN+` with the ozone concentration in Figure 4.4(left), some changes occur between 52 – 75 pphm for the parameters m and s, which change their trend. When a linear evolution of the simulation parameters is assumed (dashed line in Figure 4.4), the simulated parameters for 52 pphm would result in lower crack values, especially for longer ageing times. However, the difference is below 10 %, even for 111 h.

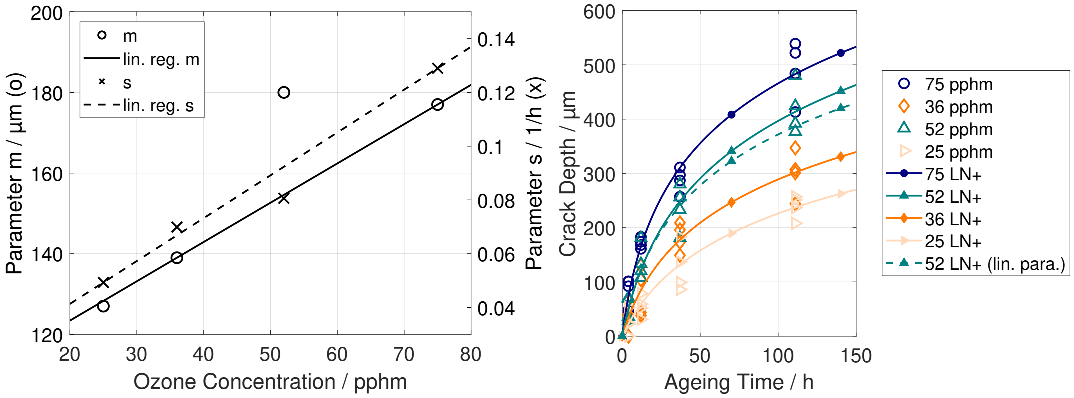

Figure 4.4 Linear evolution of parameters with ozone concentration (left), and for simulation of the crack depth over time for `C3stat` with `LN+` (right) including a simulation of 52 pphm with parameters from the `LR`.

Cyclic Strain – `C3cyc30` and `C3cyc20` Considering the cracks after cyclic loading in series `C`, all three equations: `EXP`, `LIN`, and `LN+` are capable of simulating the measured data `C3cyc30` considering the RMSE, shown in Table A.6 in the appendix. As for the static strained samples, `LN+` enables possible deepening of cracks after the measured 111 h, depicted in Figure 4.5. In addition, the result with `LN+` is closer to the experimental crack data for shorter ageing times compared to simulations with `EXP`. Simulation with `LIN` results in no immediate cracking, although the experimental results show cracks after only 4 h. Regarding `C3cyc20`, the data and hence the simulation for 52 pphm are unexpected. Nevertheless, all three, `EXP`, `LIN`, and `LN+` approximated the evolution well. The simulation with `LN+` is depicted in Figure 4.5 and the parameters for all three are listed in Table A.6 in the appendix.

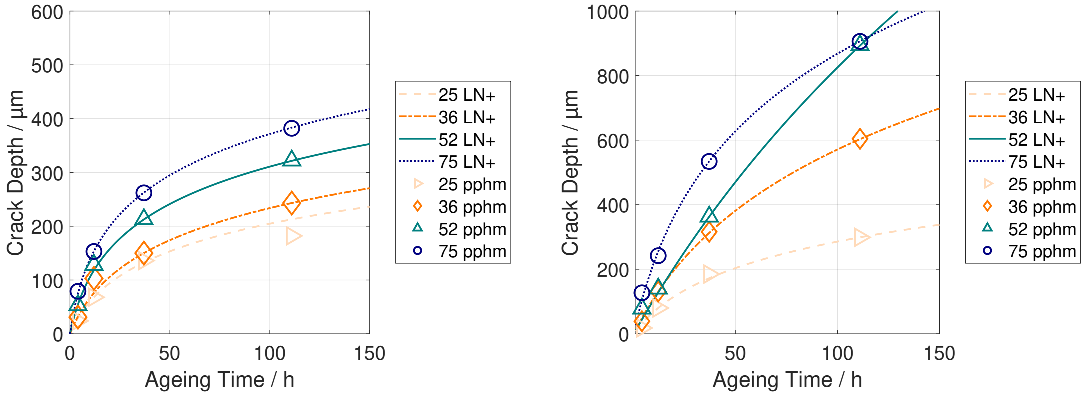

Figure 4.5 Simulation with `LN+` of the crack depth over time for `C3cyc30` (left) and `C3cyc20` (right).

In conclusion, the crack depth of all samples without antiozonants can be simulated with `LN+`.

Including Antiozonants

C2: Static Strain – `C2stat` Including 6PPD, as in `C2`, does not prevent cracks under static strain, not even at 25 pphm. Nevertheless, this ozone concentration is excluded from the simulation lacking sufficient measurement data after a corrupted first ageing run. Equation `LN+` adapts well to the measurement data, especially for short ageing times (see Figure 4.6) despite the simulation with `EXP` showing a similar approximation. The parameters for both are given in Table A.7 in the appendix.

C1 and C2: Cyclic Strain – `C1cyc30` and `C2cyc30` Considering Figure 3.54, the evolution of cracks differs strongly when antiozonants are present and a cyclic load is applied during ageing.

Concerning `C2`, the simulation with `LN+` approximates the evolution well, as shown in Figure 4.7. `LR` slightly overestimates the crack depths for short ageing

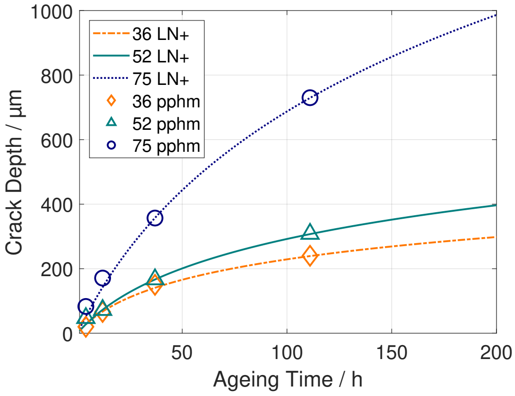

Figure 4.6 Simulation with `LN+` for the crack depth over time for `C2stat`.

times but, as is the case for the other ageing states, it enables the evolution of deeper cracks for longer ageing times for which `EXP` is limited as the parameters provided in the appendix Table A.8 show.

Considering `C1`, the crack evolution is faster than `LN+`, `EXP`, or `LIN` could simulate. Thus, a power law Eq. (4.12), `POW` is analysed,

$$\texttt{POW:} \qquad h_c^{\texttt{POW}}(t_a) = t_a^g \cdot n \tag{4.12}$$

with g without unit and n in $\mu\mathrm{m\,h}^{-1}$ and a satisfying approximation of the cracks measured, depicted in Figure 4.7.

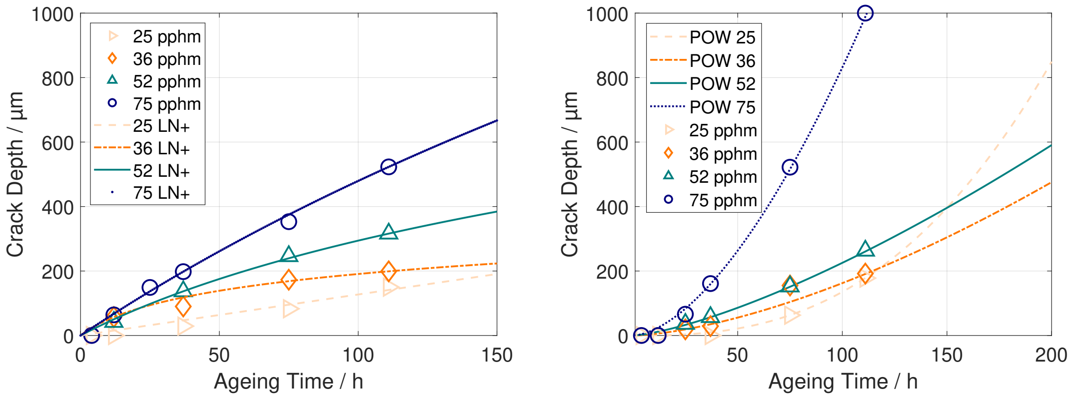

Figure 4.7 Simulation of the crack depth over time for `C2cyc30` with `LN+` (left) and `C1cyc30` with `POW` (right).

Result

In conclusion of the simulation of crack depth over ageing time, neither the exponential function `EXP` motivated by a simple equation nor the linear, logarithmic function `LIN` captures the crack depth for longer ageing times than those given by the conducted database. All strain states during ageing in `C3` and `C2` can be approximated by `LN+`. Therefore, the crack data is normalised to the ageing time of 111 h regarding each strain set and ozone concentration. Despite the large scatter in the measured data, made apparent by the boxplots, `LN+` approximates the crack evolution in the median, as shown in Figure 4.8. A factor m of 4.48×10^{-1} µm and parameter s being $7.48 \times 10^{-2}\ \mathrm{h}^{-1}$ leads to an RMSE of 0.09.

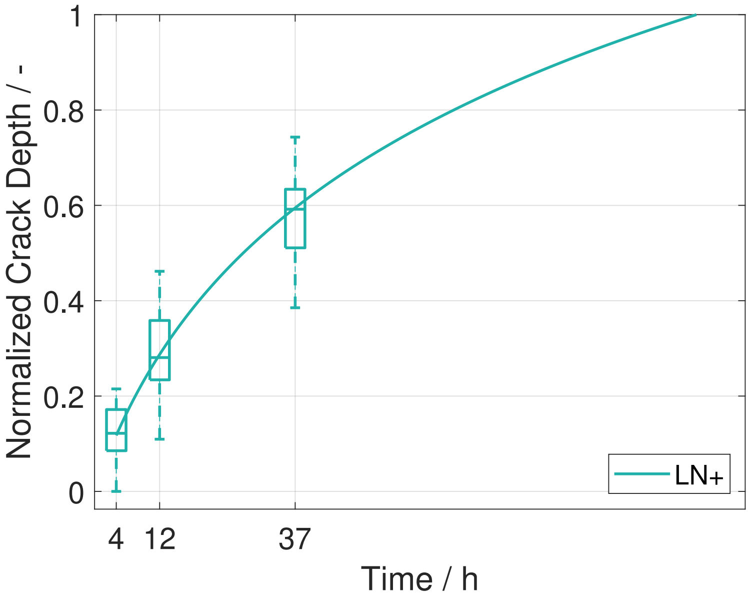

Figure 4.8 Simulation of the normalised crack depth over ageing time for `C3stat`, `C2stat`, `C3cyc30`, `C2cyc30`, and `C3cyc20`.

The cyclic strain in `C1` cannot be simulated by `LN+` but only by `POW`.

4.1.4 Dependence on Ozone Concentration

If the mechanical strain surpasses a threshold value, cracks evolve and their growth is not only dependent on time but also on the ozone concentration.

Concerning the ageing time, the Pearson and Spearman correlations and the cosine similarity between the ozone concentration and crack depth are provided in Table A.3 in the appendix. Although r_P and r_{Sp} are weak a good significance value is achieved. Normalised data leads to a cosine similarity of 0.7 (see Table A.4). Even though statistical parameters do not clearly indicate this, a linear correlation is used, as suggested in the literature described in Section 1.3.4 :

$$\texttt{LR:} \qquad h_c^{\mathrm{LR}}(\mathrm{c_{oz}}) = \mathrm{b} \cdot \mathrm{c_{oz}} - \mathrm{f} \tag{4.13}$$

As cracks were not measured for the short ageing times for all tested series and any crack existing without ozone loading is not reasonable, the parameter f in µm is limited to positive values. Since the crack depth increases with the ozone concentration, b in µm/pphm is also set positive. To evaluate the linear regression (`LR`), the adjusted coefficient of determination r^2 is given in Section A.4, which is the explained sum of squares divided by the sum of squared total deviations adjusted by the number of observations and the number of parameters of the regression function [134].

Any chemical reaction is dependent on the availability of reaction partners. Thus, a higher concentration of ozone leads to a faster reaction until the available double bonds in the NR limit the reaction rate rather than the ozone concentration, as discussed in Section 3.4 for Figure 3.61.

No Antiozonants

Static Strain – `C3stat` A reaction speed limit is assumed to take effect regarding the results of series `U`. Thus, the simulations with `LR` for the crack evolution over ozone concentration exclude the measurement data for 75 pphm (see Figure 4.9 and Table A.9 in the appendix).

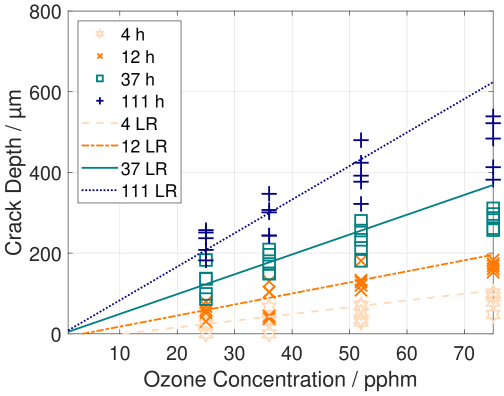

Figure 4.9 Simulation of the crack depth over ozone concentration for `C3stat` with `LR` considering data up to 52 pphm.

Hence, the simulation displays higher crack depths, similar to the measurement data for 75 pphm.

Cyclic Strain – `C3cyc30` and `C3cyc20` Both cyclic strains during ageing in `C3` are simulated with `LR`, as shown in Figure 4.10. Below 75 pphm, the simulation matches the data for `C3cyc30`. The assumed linear correlation between the crack depth and ozone concentration is questionable for `C3cyc20` regarding the coefficient of determination in Table A.10 in the appendix. However, for 4 h and 111 h the simulation is good, as shown in Figure 4.10.

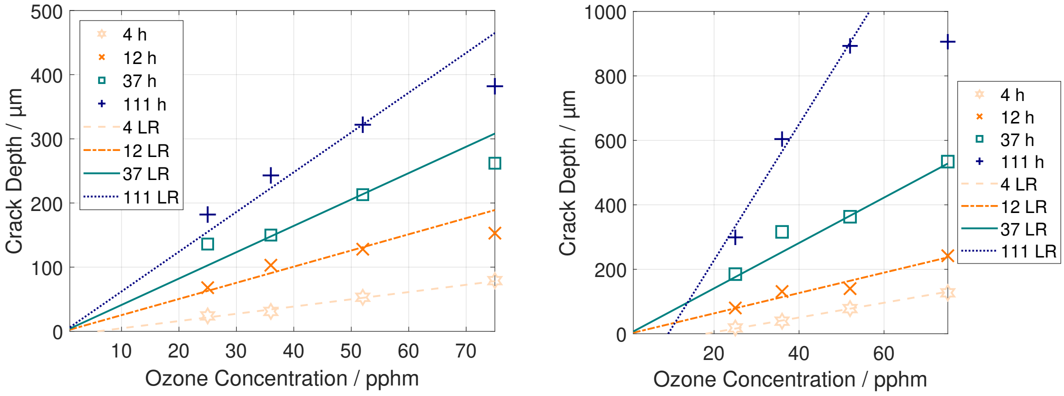

Figure 4.10 Simulation of the crack depth over ozone concentration for `C3cyc30` (left) and `C3cyc20` (right).

Including Antiozonants

C2: Static Strain – `C2stat` Due to the corrupted artificial ageing at 25 pphm, the evolution equation can only be fit to the other three tested concentrations. Since 75 pphm is considered to lead to a nonlinear change in the reaction, no simulation is conducted for the static strain measurements with `C2`.

C1 and C2: Cyclic Strain – `C1cyc30` and `C2cyc30` Regarding `C2`, a linear evolution of crack depth holds up to 52 pphm and depicts the measured late onset of cracks depending on the ozone concentration. Contrary to the measurements in `C3`, the crack depth at 75 pphm is not below or within a linear trend but for 111 h it is above the linear trend. This phenomenon occurs even more strongly for `C1` with the measured crack depth for 75 pphm and 111 h being out of the scale of the plot in Figure 4.11. Concerning all ageing times apart from 25 h, the crack depth at 75 pphm is higher than expected by `LR`. In general, in `C1` the linearity is questionable for most ageing times. The simulations with `LR` are shown in Figure 4.11 and the corresponding data is listed in Table A.11 in the appendix.

Result

All databases discussed above, apart from the `C1cyc30`, clearly show a linear crack evolution with ozone concentration in the range of 25 – 52 pphm. The

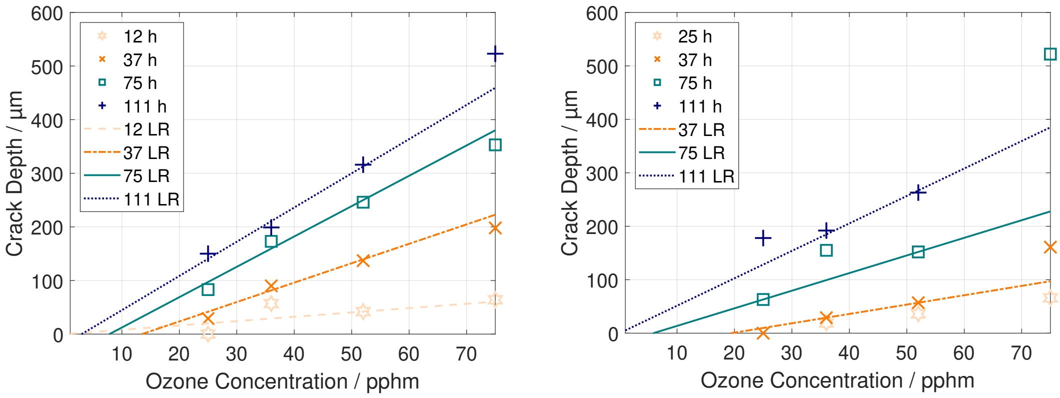

Figure 4.11 Simulation of the crack depth over ozone concentration for `C2cyc30` (left) and `C1cyc30` (right).

correlating crack data, excluding `C1`, is separately normalised to 52 pphm for each ageing time, strain state, and compound. An overall `LR` is fitted resulting in a good approximation considering the data presented in a boxplot, as shown in Figure 4.12. Within 25 pphm and 36 pphm, some outliers are present correlating to the short ageing time of 4 h. In contrast, for 75 pphm the outliers correspond to long ageing times, confirming the change at 75 pphm. However, the median values of the boxplot lead to the assumption of a linear behaviour, including for 75 pphm. In Figure 4.12, the simulation with `LR` on normalised data is plotted, and a slope of 1.92×10^{-2} and start at 0 pphm leads to an adjusted coefficient of determination of 98.7 %. A linear correlation with ozone concentration is assumed in the following combined evolution equation in Section 4.2.1.

4.1.5 Initiation Time

Although the simulation over ageing time neglected a delayed start of cracking with the chosen `LN+` equation, in Section 4.1.4 some series show no cracks for short ageing times and low ozone concentrations. Some initiation times t_i for cracking are provided by Zuev and Pradvednikova [93], Dolezel [94], and Nonnenmacher [95] and are shown to be indirectly proportional to the ozone concentration c_oz and dependent on a material parameter B in h · pphm:

$$t_\mathrm{i}(c_\mathrm{oz}) = \frac{B}{c_\mathrm{oz}} \tag{4.14}$$

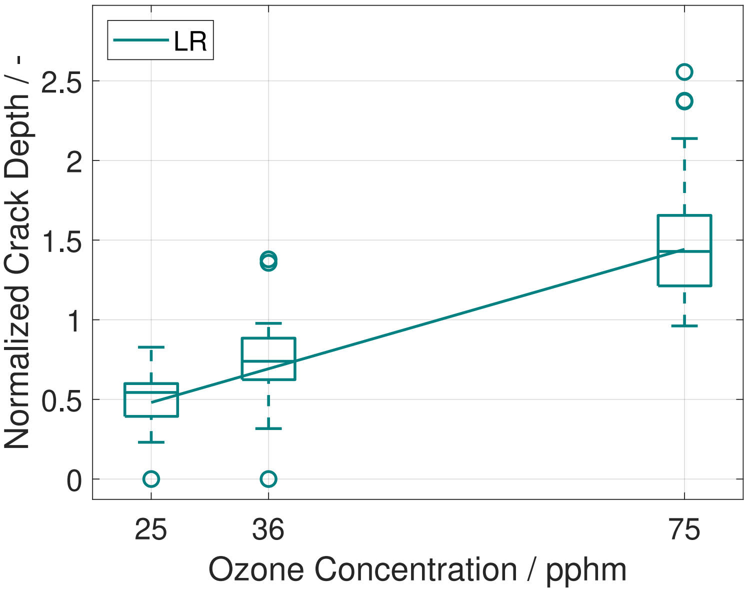

Figure 4.12 Simulation of the normalised crack depth over ozone concentration for `C3stat`, `C2stat`, `C3cyc30`, `C2cyc30`, and `C3cyc20`.

4.1.6 Diffusion Limitation

Without strain during ageing, the degradation depth is limited to a few µm shown by the FT-IR measurements in Section 3.2.1. Even without antiozonants in `C3`, a product layer seems to hinder diffusion of ozone into the sample core. Though cracks evolve, the diffusion characteristics may change due to a product layer. Regarding the ageing of pristine material as discussed so far, any change is intrinsic in the simulated evolution. However, if consecutive to a first ageing set, a different ozone concentration is applied, and the resulting crack depth is not simply superposed. Thus, after each ageing procedure, the subsequent one is considered with a reduction factor to account for the change in diffusion characteristics of prior ageing.

The diffusion limitation by a product layer is described in Baerns *et al.* [129] by the so-called model 3 of a gas-solid reaction. It describes the process of a solid grain reacting with gas, limited by the diffusion through a product layer. The diffusion through the product layer is assumed to be in a quasi-static state.

Assuming an infinite plane instead of a grain, the equation for the diffusion layer depth h_D is adapted (D_{eff} in $\mathrm{m^2\,s^{-1}}$, c_{gas} in pphm $= \frac{1}{10^8}$, t in s):

$$h_D = \sqrt{2D_{eff}c_{gas}t} \tag{4.15}$$

The depth is proportional to the effective gas arriving at the reaction front, assuming a linear dependence with the gas concentration. A limit in crack due to reduced diffusion after prior ageing could be implemented by a factor < 1 applied to the evolution functions for ozone loading on pristine samples.

4.2 Phenomenological Evolution Equation

The databases used are the same as in Section 4.1, and are listed in Table 4.1. The weighting introduced in Section 4.1.2 for isolated simulations is applied likewise for the combined fit for ageing time and ozone concentration.

Fitting Algorithm A genetic algorithm (GA) is applied to find the parameters of the following evolution equations.

GAs are optimisation techniques inspired by the principles of natural selection and genetics. They simulate the process of evolution, representing potential solutions to a problem as individuals in a population. These individuals undergo selection, crossover, and mutation to produce new offspring, gradually improving the solution quality. Therefore, a global optima is approached, where gradient-based methods might get stuck in local optima. Another benefit of the GAs is their robustness towards noise which is present in the crack depth data considered here.

4.2.1 Evolution Equation Depending on Ageing Time and Ozone Concentration

Except for the cyclic strain during ageing in `C1`, an approximation with `LN+` with ageing time and a `LR` with ozone concentration lead to good correlation with the measured crack depths. Thus, `LN+` is multiplied with the ozone concentration to include the linear dependence on the latter, with m (see Eq. (4.11)) and b (see Eq. (4.13)) combined to one factor mb in µm/pphm:

$$h_c(t_a, c_{\mathrm{oz}}) = \mathrm{mb} \cdot c_{\mathrm{oz}} \cdot \ln\left(1 + \mathrm{s} \cdot (t_a)\right) \tag{4.16}$$

Since cracks were not measured for short ageing times in some of the series, an initiation time for cracking can be considered with t_i from Eq. (4.14) instead of a y-intercept alike f in Eq. (4.13):

$$\begin{aligned} h_c(t_a, c_{\mathrm{oz}}, t_i) &= \mathrm{mb} \cdot c_{\mathrm{oz}} \cdot \ln(1 + \mathrm{s} \cdot (t_a - t_{\mathrm{i}})) \\ h_c(t_a, c_{\mathrm{oz}}) &= \mathrm{mb} \cdot c_{\mathrm{oz}} \cdot \ln\left(1 + \mathrm{s} \cdot (t_a - \frac{B}{c_{\mathrm{oz}}})\right) \end{aligned} \tag{4.17}$$

In `C3`, cracks were measured under 25 pphm after 4 h ageing time for all series, and thus Eq. (4.16) is used to simulate the crack depths depicted in Figures 4.13, 4.14 and 4.15. Considering `C2`, Eq. (4.17) enables a delayed start of cracking, as simulated for the evolution solely over the ozone concentration (Section 4.1.4 and Figure 4.11). The simulation results are plotted in Figures 4.16 and 4.17. Concerning `C1`, `POW` is combined with `LR`, thereby reducing n (Eq. (4.12)) and b (Eq. (4.13)) to nb in µm/pphm/h and optionally adding the initation time:

$$h_c(t_a, c_{\mathrm{oz}}) = t_a^g \cdot nb \cdot c_{\mathrm{oz}} \tag{4.18}$$

$$h_c(t_a, c_{\mathrm{oz}}) = (t_a - \frac{B}{c_{\mathrm{oz}}})^g \cdot nb \cdot c_{\mathrm{oz}} \tag{4.19}$$

In Table 4.3, the applied equations for each database are listed in addition to the calculated parameters. Their goodness of fit χ is estimated by the root mean square error (RMSE) and the mean absolute error (MAE) [135], with both being normalised to the number of measured sets. Both errors are of comparable dimension in all simulated databases. Relating the absolute error in each data couple to the crack depth simulated, a mean relative absolute error (MAEr) is obtained which is calculated as,

$$h_c^{\mathrm{MAEr}}() = \frac{\sum |h_c^{\mathrm{calc}} - h_c^{\mathrm{meas}}|}{n_{\mathrm{cd}}}. \tag{4.20}$$

Especially regarding `C3stat` simulated in Figure 4.13, MAE and MAEr are comparably small for the range of measured crack depths of up to 103 µm with h_c^{calc} being the crack depth calculated in simulation, h_c^{meas} the corresponding measured crack depth, and n_{cd} the number of measured cracks in the data set. The introduced measure for the GOF is ignored if no crack is measured for h_c^{meas}.

To gain a visual impression, the absolute error between the simulation and measurement is plotted for each database in Figures 4.13, 4.14, 4.15, 4.16, 4.17 and 4.18. As the weighting in Section 4.1.2 indicates, the error of the fits is largest for short ageing times and low ozone concentrations, thereby correlating with the measurement uncertainties.

Table 4.3 Simulation parameters for the evolution equations Eq. (4.16), Eq. (4.17) and Eq. (4.18) up to 52 pphm

Database	**Evo. Eq.**	**Params**			χ		
		-	**mb**	**s**	**RMSE** / µm	**MAE** / µm	**MAEr** / %
`C3stat`	Eq. (4.16)		3.86	0.0657	31.4	2.29	23
`C3cyc30`	Eq. (4.16)		2.11	0.1840	17.0	4.50	13
`C3cyc20`	Eq. (4.16)		16.1	0.0164	39.8	3.33	15
		B	**mb**	**s**	**RMSE** / µm	**MAE** / µm	**MAEr** / %
`C2stat`	Eq. (4.17)	0.60	4.90	0.022	15.0	4.82	14
`C2cyc30`	Eq. (4.17)	173	4.90	0.022	16.4	3.64	22
		-	**nb**	**g**	**RMSE** / µm	**MAE** / µm	**MAEr** / %
`C1cyc30`	Eq. (4.18)		0.01	1.330	20.9	2.32	20

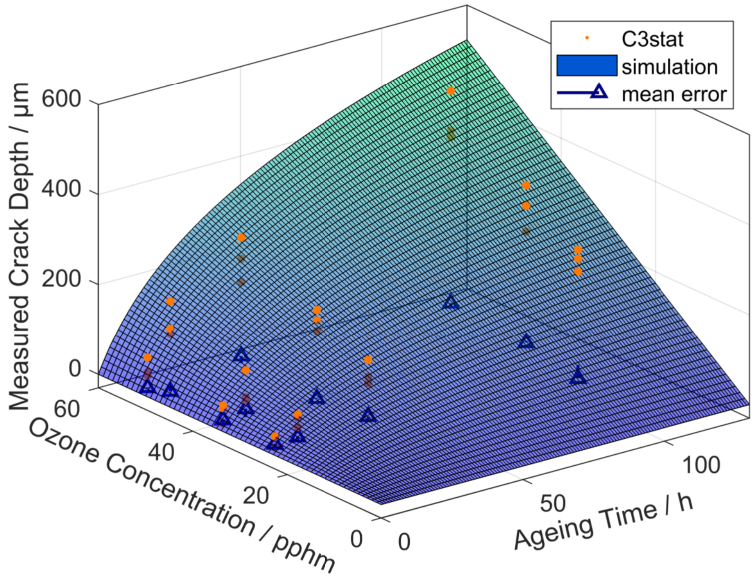

Figure 4.13 Simulation of the crack depth for `C3stat` with Eq. (4.16).

Since the regular measurement data in series `U` for `C2` at 25 pphm is invalid, this simulation uses two additional conducted measurements at 25 pphm for 25 and 74 h, as shown in Figure 4.16. As the simulated parameter B of 6.00×10^{-1} is small compared to the ozone concentrations applied, there is hardly a delay in cracking for the static strain in `C2` and Eq. (4.16) could also be applied while disregarding B. In contrast, under cyclic load, `C2` shows a profound delay in crack evolution.

Since a simulation of `C1cyc30` with Eq. (4.19) yielded B with a value of approximately 0, Eq. (4.18) is used to show the immediate start of cracking in Figure 4.18. This result is contrary to the simulation over the ozone concentration

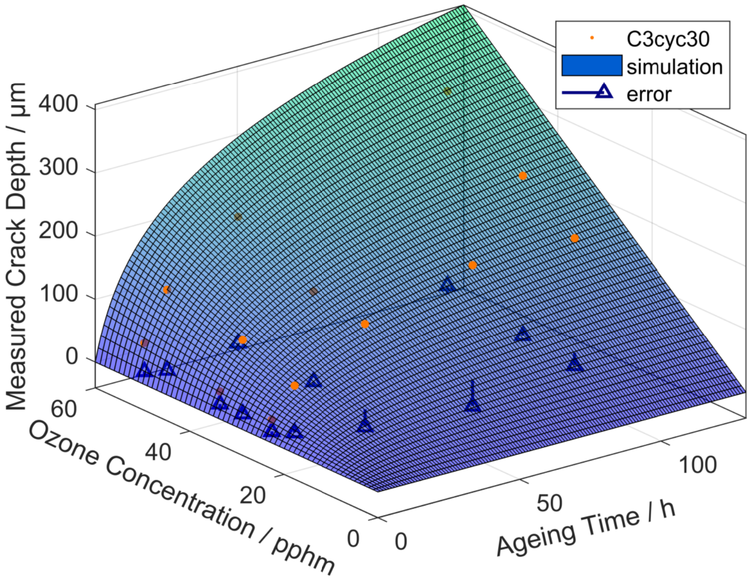

Figure 4.14 Simulation of the crack depth for `C3cyc30` with Eq. (4.16).

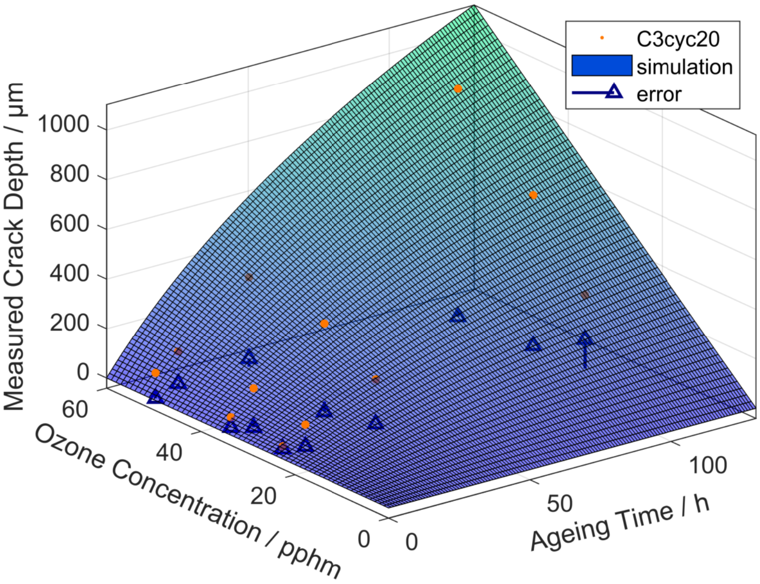

Figure 4.15 Simulation of the crack depth for `C3cyc20` with Eq. (4.16).

in Figure 4.11 where the `LR` assumes a delay of cracking even for 75 h ageing time.

4.2.2 Comments on Consecutive Ageing Sets

Diffusion characteristics can change with the ageing progress. Starting with a pristine sample, the simulation of the crack depth with the evolution equations covers a change in diffusion. Consequently, if the ozone concentration is changed

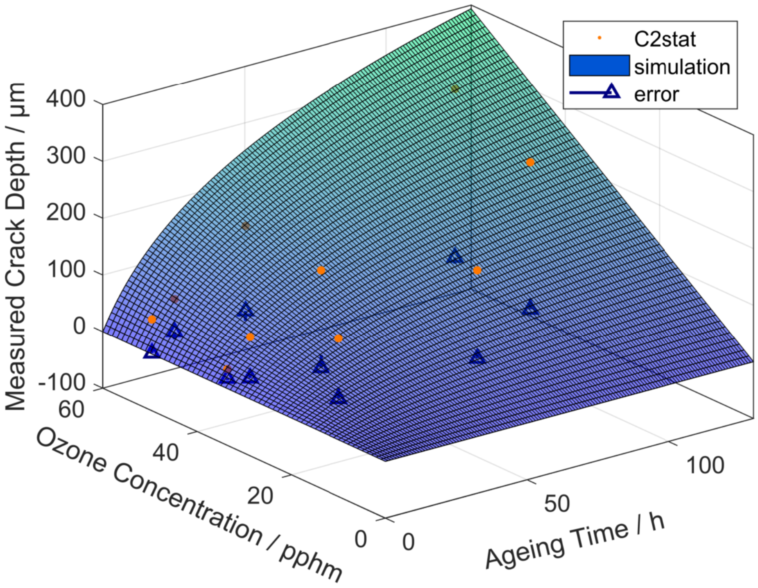

Figure 4.16 Simulation of the crack depth for `C2stat` with Eq. (4.17).

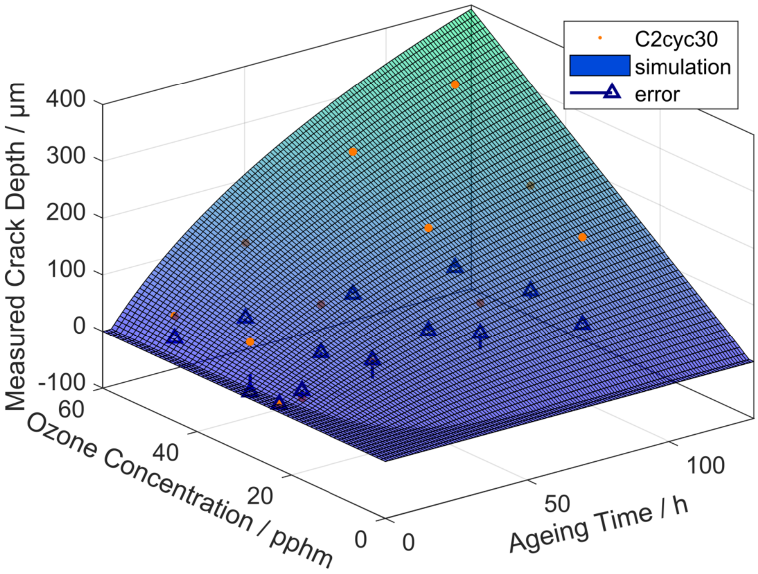

Figure 4.17 Simulation of the crack depth for `C2cyc30` with Eq. (4.17).

in a second ageing set, the initial diffusion characteristics are not equal to a pristine sample and thus the crack evolution is not equal to the one simulated for a pristine sample. From the second ageing set on, the diffusion is assumed to be reduced, which is in line with the measured change of the surface layer described experimentally in Section 3.2.1, Section 3.2.2, Section 3.2.3, and Section 3.3.2. Consecutive ageing experiments were conducted for `C2` and `C3` with static strain

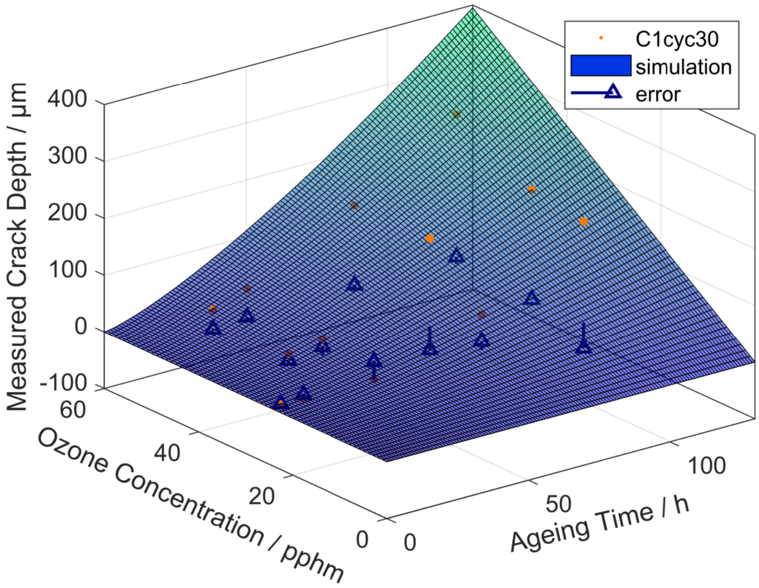

Figure 4.18 Simulation of the crack depth for `C1cyc30` with Eq. (4.18).

during ageing resulting in the measured crack depth listed in Table 4.4. As expected, the simple superposition of corresponding calculated crack depths based on the results of Section 4.2.1 overestimates the measured crack depth with a factor of 1.2 – 1.9. Comparing the compounds without (`C3`) and with antiozonants (`C2`), on average, the overestimation, i.e. the intensity of diffusion change is larger in `C3` aligned with the experimental results in Section 3.2. To quantify the change further, additional experimental data is required.

4.2.3 Simulation of Ambient Ozone Level

Considering a constant ambient ground-level concentration of 3 pphm, the crack depths are calculated with the derived evolution equations for long ageing periods (Table 4.5). The cyclic strains considered are all 30 ± 10 % to compare the three compounds.

Regarding static strains, the addition of 6PPD is advantageous compared to the unprotected NR, as shallower cracks are predicted. In contrast, with a cyclic strain of 30 ± 10 %, after one month, `C2` catches up with the crack depth calculated for `C3`. Considering `C1`, the deceleration of crack development is of short duration. Already after one week the predicted cracks grow extremely fast, for the equation chosen, Eq. 4.18, which is a power law.

Table 4.4 Comparison of crack depths in µm for consecutive ageing in measurement and calculation.

	Ageing Set	pphm/h				
Compound, `C3`	1	75/37	25/74	25/74	25/74	52/37
	2	25/74	52/37	52/37	52/37	25/25
	3	-	25/4	-	25/25	-
Crack depth		µm				
Measured		339	227	260	267	204
Superposition of calc. crack depths		528	441	418	512	341
Relation		1.6	1.9	1.6	1.9	1.7
	Ageing Set	pphm/h				
Compound, `C2`	1	75/37	25/74	52/37	25/74	
	2	25/25	25/25	25/25	52/37	
	3	-	-	-	25/25	
Crack depth		µm				
Measured		191	130	213	286	
Superposition of calc. crack depths		416	232	316	458	
Relation		1.8	1.5	1.2	1.3	

Table 4.5 Calculated crack depth in µm for long ageing periods at 3 pphm ozone concentration for different mechanical loads.

Compound and type of strain	**24 h**	**7 d**	**30 d**	**180 d**	**365 d**	**3650 d**
`C3`, **static** strain	11	29	45	66	74	100
`C2`, **static** strain	8	22	34	50	56	77
`C3`, **cyclic** strain	11	22	31	42	47	61
`C2`, **cyclic** strain	0	18	41	67	77	111
`C1`, **cyclic** strain	2	28	195	2112	5309	113 494

It might be a matter of the time taken for wax to migrate to the surface, thereby increasing the beneficial effect for long ageing times at very low ozone concentrations. The prediction for `C1` seems to be extremely negative, whereas the predicted crack depth for the long-term ageing of `C2` and `C3` yields realistic values. To validate the predictions, measurements in a similar ageing time would be necessary.

Table 4.6 Equivalent time until a crack depth of 10 years ageing under 3 pphm is achieved by applying 50 pphm.

Compound and strain	**Equivalent ageing**, h
`C3`, static strain	10.3
`C2`, static strain	11.0
`C3`, cyclic strain	4.3
`C2`, cyclic strain	29.5
`C1`, cyclic strain	114 011

Through an accelerated ozone concentration of 50 pphm, theoretically the equivalent crack depth regarding 10 years of ageing at 3 pphm is achieved after the time given in Table 4.6.

4.3 Validation

Table 4.7 Databases for validation of evolution equations and corresponding GOF as in 4.3.

Database **to** fit	Database **for** validation	GOF Estimators normalised to number of data sets		
		RMSE / µm	MAE / µm	MAEr / %
`C3stat`	`BWstat`	34.0	29.0	25
`C3stat`	`Z3stat`	62.2	47.2	7
`C3cyc30`	`C3cyc12`	76.0	66.5	22
`C3cyc20`	-			
`C2stat`	`Z2stat`	57.6	10.6	27
`C2cyc30`	`C2cyc12`	53.5	18.8	17
`C1cyc30`	-			

Database Used to Validate Parameters In Table 4.7, the database available to validate the evolution equations in Section 4.2 is listed with correlating GOF estimators for the validation data. Concerning `C3cyc20` and `C1cyc30`, no additional data is available to validate the resulting evolution equations. In addition, only the crack depths generated by ozone concentrations below 75 pphm are considered. Since for `C3cyc12` and `C2cyc12` the parameter range tested focuses on high ozone concentrations, excluding 75 pphm, only three measurements are available for validation. As series `D` is only aged at 75 pphm, it is not used to validate the evolution equations.

The prediction value of the evolution equations fitted in Section 4.2.1 is evaluated by RMSE, MAE, and MAEr calculated for the validation databases. Comparing the fit and validation GOF estimators, up to 21 times higher MAE is calculated for all sets except `Z2stat`. However, MAE is sensitive to the sign of the error in each point. Besides `Z2stat`, BWstat also results in a similar RMSE, while the other validation data sets have up to 4.5 times higher RMSE compared to their correlating fit database. The range of MAEr is comparable with 13 – 23 % in the fitting and 7 – 27 % within validation.

As shown in Section 4.2.1, the absolute error is concentrated on the parameter sets with a larger relative uncertainty of measurement which is visible in the following plots: Figures 4.19, 4.20, 4.21, 4.22 and 4.23.

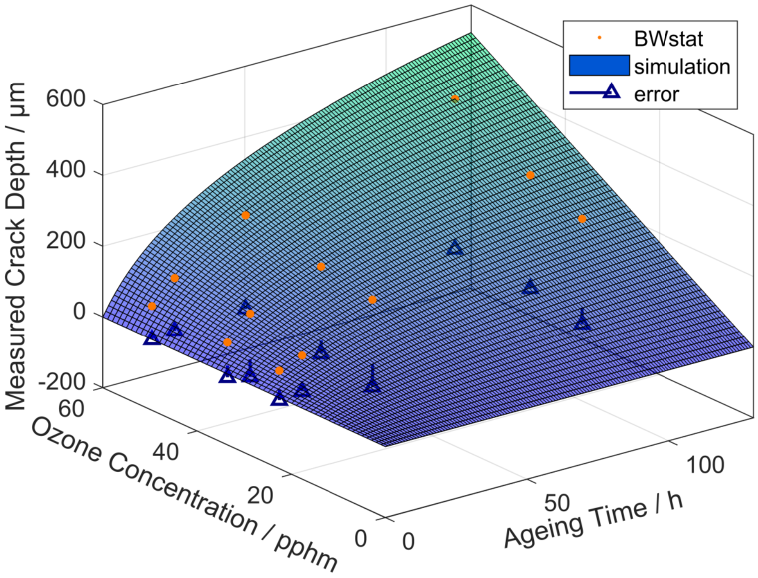

Figure 4.19 Validation of Eq. (4.16) fitted for `C3stat` with `BWstat`.

4.4 Discussion of Selected Evolution Equations

The evolution of crack depth with time and under different ozone concentrations in the tested range is similar when including the different strain types (static and cyclic). It can be simulated by one equation Eq. (4.17) with a logarithmic dependence on the ageing time and linear dependence on ozone concentration. By adaption of the parameters for the different compounds and strain states measured, the crack depths are approximated well. The exception is `C1` which displays a more rapid increase of cracks with time following the power law and

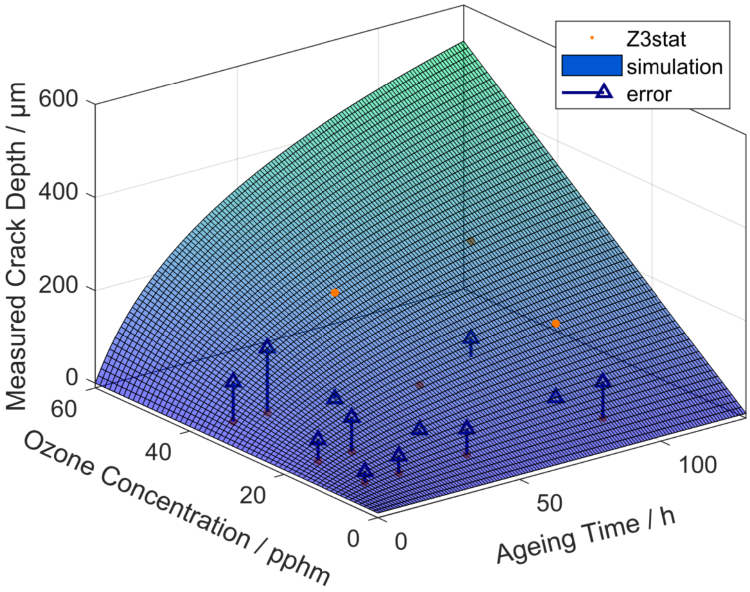

Figure 4.20 Validation of Eq. (4.16) fitted for `C3stat` with Z3stat.

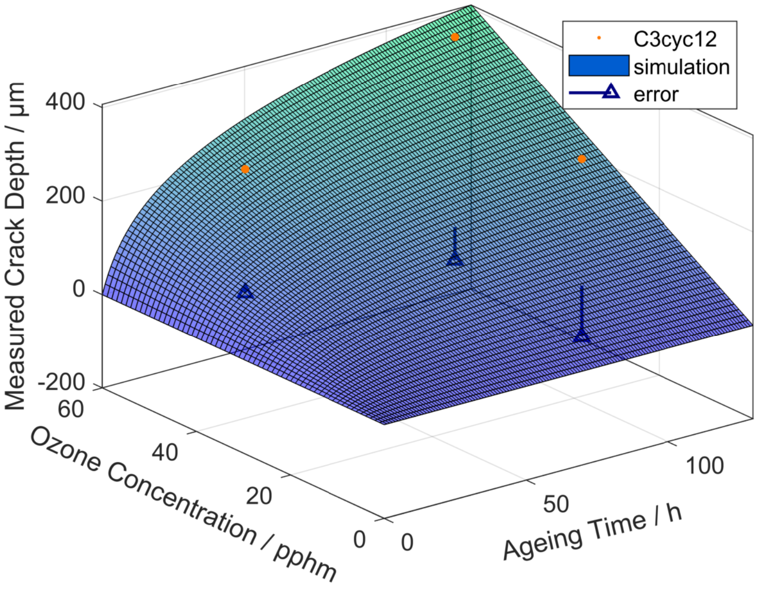

Figure 4.21 Validation of Eq. (4.16) fitted for `C3cyc30` with `C3cyc12`.

a not as clearly linear evolution with ozone concentration.

In addition, as the ozone concentration is fluctuating on the ground level with daytime and during the year, sequential ageing sets could help to quantify the change in diffusion due to ozone ageing. The evolution equation is based on crack data generated for a fixed ozone concentration attacking a pristine sample, and thus any change in diffusion characteristics is implicit. When changing the

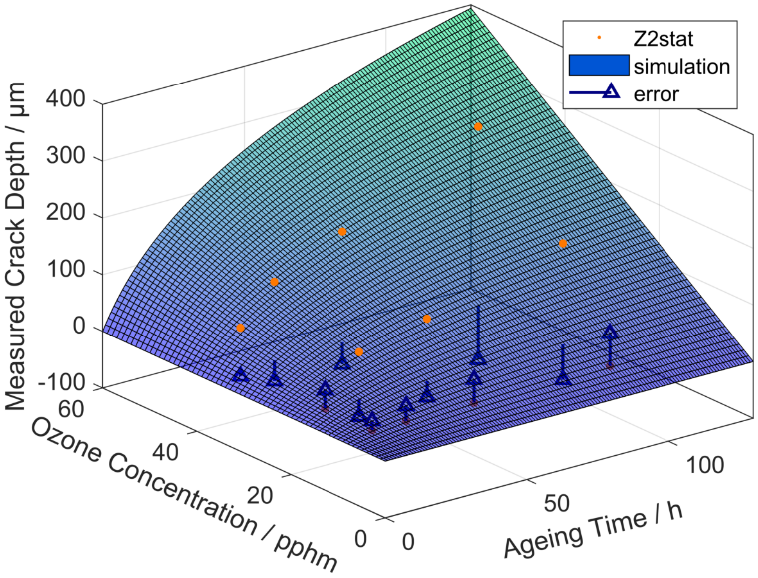

Figure 4.22 Validation of Eq. (4.17) fitted for `C2stat` with `Z2stat`.

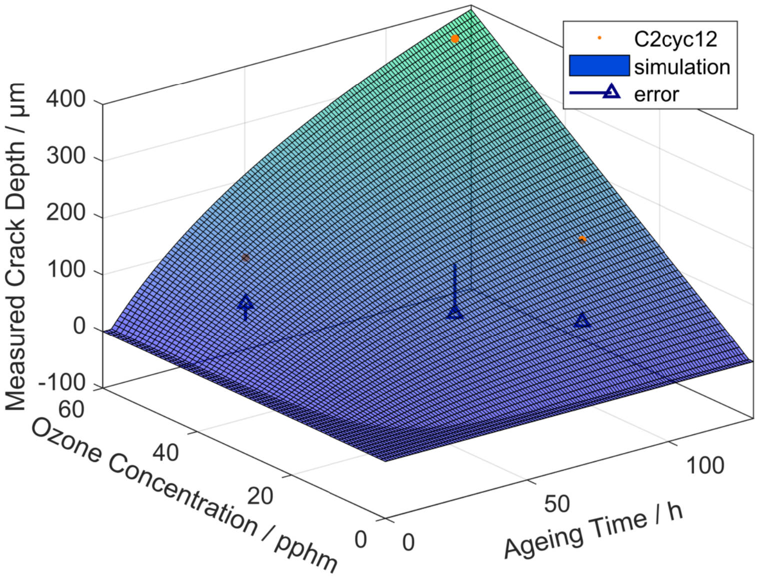

Figure 4.23 Validation of Eq. (4.17) fitted for `C2cyc30` with `C2cyc12`.

ozone concentration in sequential ageing sets, the sample is no longer pristine and a simple superposition of calculated crack depths overestimates the measured one. A reduced rate of crack depth must be present for `C2` and `C3` for subsequent ageing sets compared to the first ageing set. With more data, it might be possible to quantitatively analyse a reduction factor due to prior ageing parameters.

In conclusion, with the derived evolution equation the crack depth can only be simulated for constant ozone loading. A constant ambient ozone level of 3 pphm is predicted to lead to crack depths of 60 – 110 µm within 10 years in `C2` and `C3`. However, no validation data for long-term ageing under low concentrations is available. Additional longterm measurements – especially in the lower ozone concentration range and for consecutive ageing sets – are recommended to validate the approximation for the range of realistic ground-level ozone concentrations. The validation of higher ozone levels with different databases shows that the evolution equations derived are capable of predicting measured data with a similar accuracy as the fitting in the first place.

> *An artistic statement rarely emerges from a vacuum. It grows out of some kernel of inspiration that eventually becomes an individual creation.*
>
> — Hilary Hahn

5

Conclusion, Recommendations and Outlook

Conclusion

As expected, the ageing of NR is experimentally stated to be dependent on the

1. Ageing time
2. Ozone concentration
3. Strain level, and
4. Strain type: static or cyclic

present during ozone exposure. Considering the literature review in Section 1.3.4, many statements can be confirmed.

However, considering low ozone concentrations in the literature, the results of artificial ageing processes should be evaluated carefully due to uncertainties in fast ozone measurements necessary in accelerated ageing procedures. Thus, a scattering of measurements is observed for crack depths at low ozone concentrations and short ageing times.

Compared to thermal-oxidative ageing, ozone ageing has a shallower layer with measurable change. The change in stiffness (Section 3.3.2) and density (Section 3.2.4) is only measured in the top layer, which is cut from the aged sample of about 150 µm. In addition, the change in density is less pronounced compared to thermo-oxidative ageing. Ageing at 40 °C for a maximum of 111 h in air does not cause a significant change in the stress-strain curve in a uniaxial tensile test (Section 2.3.1), while the range of measured stresses overlaps for pristine and aged samples. This confirms that thermo-oxidative ageing can largely be ruled out by temperature. In addition, it is experimentally proven that even under static stress of up to 80 %, no cracks develop beyond surface flaws for thermo-oxidative ageing at 40 °C.

A threshold strain during ozone ageing is necessary for cracks to evolve as shown in the surface images of the samples exemplarily outlined in Section 3.3.5. Additionally, the observation of slight changes in the stress-strain curve for unstrained ozone aged samples supports the absence of cracks without strain discussed in Section 2.3.4. However, once the threshold is passed, the static strain level does not correlate to crack depth as addressed in Section 3.3.4. No variations in the crack distance distribution or the crack length above 10 % strain are observed. A growing crack distance with ageing time supports the merging of cracks highlighted in the literature. Evolved cracks show a branching like those observed for fatigue tests without ozone loading.

Without strain during ageing, an embrittled surface layer is confirmed by shallow hardening with less then 100 μm of depth measured in microhardness tests (see Section 3.3.2). Although the change is shallow enough to show little difference compared to pristine material in uniaxial tension tests. From the FT-IR measurements (Section 3.2.1), it is concluded that a shallow molecular change reaches about 20 μm from the surface inwards, albeit only for `C3`. In the aged surface layer split a 150 μm thick, the DSC tests described in Section 3.2.2 display a lowered specific heat capacity for aged samples of `C3` but no change in T_g. Using the *HotDisk®* method (Section 3.2.3), the pristine c_p value achieved by DSC tests is confirmed using the results outlined in Section 3.2.4.

The importance of surface homogeneity and flaws for crack initiation and geometry is recognised in the sample preparation in Section 2.4.2, just as Braden and Gent [64] highlight a correlation between surface smoothness as the induced cut length and the threshold stress. In contrast, the sample thickness has no influence on the resulting crack depth. This is confirmed by the first method to quantify the crack depth via uniaxial tension tests, demonstrated in Section 3.3.4. The experimental approach employs optical analysis using a microscope as a second approach in order to investigate the cross-section. This method results in better detection of the maximal cracks achieved, which may not necessarily be of homogeneous depth.

The fatigue tests illustrated in Section 3.3.3 show that ozone ageing prior to mechanic fatigue loading drastically reduces the lifetime. Manufacturing flaws are the initiation location of cracks for pristine samples, which are predominated by cracks presenting even bigger flaws after ageing. Interestingly, although wax is part of the compounds used, it does not prevent cracking, even if the process temperature is at the melting peak of the wax applied. In addition, dynamic strain, which should enhance migration, leads to premature failure compared to static strain.

In research presented in this thesis, the importance of cyclic strain is clarified for the evolution of cracks with and without antiozonants. After a deceleration of crack evolution including antiozonants, for long-term ageing the unprotected compound displays the shallowest cracks. Comparing the crack depth at cyclic strain during ageing in Section 3.3.5, the amplitude reaching the unloaded initial state causes cracks almost twice as deep compared to cyclic load without unloading. Adding 6PPD yields smaller crack depths for static strain during ozone ageing but enhances the crack depth under cyclic loading for long ageing times. Additional wax prevents cracking for uniaxial tension load, but increases the crack depth for cyclic loading.

As postulated in the literature, the evolution with ozone concentration can be approximated by a linear correlation (see Section 4.1.4 and Section 4.2). However, contrary to some statements in the literature, the linearity is no longer given at 75 pphm. The evolution with time can be approximated for all compounds and mechanical strains during ageing with the same evolution equation, by adapting the parameters to achieve different crack depths correlating to the strain states and compounds for `C2` and `C3`. Only `C1` behaves differently regarding the evolution with time (Section 4.1.3).

Although the analytical analyses of the crack depth for constant ozone loading were successful, the change of evolution of cracks for sequential loading with different ozone concentrations points to a change in diffusion characteristics. Therefore, it is questionable if the calculation of the crack depth with the evolution equation derived will deliver the crack depth to be found in real outdoor tests. In addition, several other environmental uncertainties introduced by random fluctuations of additional properties might influence the result of outdoor weathering.

Recommendations

To measure the ozone resistance of NR in the lab, it is recommended to use ozone concentrations below 50 pphm. Thus, the linear dependence of the crack depth on ozone concentration enables the prediction of crack depths for lower concentrations, as described in Section 4.1.4. However, the lower the concentration, the more variation is caused by the inaccuracy of the rapid ozone measurement necessary to control the ageing device, as outlined in Section 2.3.2. In addition, the ageing time should be chosen long enough to reduce possible measurement error from the set-up and cool-down phases of the lab devices. Considering the almost constant result of the lifetime after 38 h in the fatigue experiments in Section 3.3.3 no fewer than 40 h are recommended for artificial ageing.

Consequently, artificial ageing at 50 pphm for 2 d is considered to be ideal based on the experiments presented in this thesis.

Outlook

Since none of the common antiozonants sufficiently protects NR from cracking under ozone loading, coatings might be applied for protection [45]. Already described by Braden and Gent [2], silicone stopcock grease is used to partially prevent ozone attack on an NR sample. Other materials are applied such as PMMA for protection of polymers in solar panels [45] and a titanium dioxide coating has also been tested. However, for the protection of rubber, the deformation in use must be withstood by the coating and the adhesion between coating and rubber [136]. Coating rubber with polydimethylsiloxane (PDMS) was tested [80] to evaluate an easy protection possibility apart from wax and PPDs or blending of rubber types. Favourably, PDMS has a glass transition temperature of about $-65\,°\mathrm{C}$, which is slightly lower than that of NR. Thus, a reasonable application range with rubbery behaviour of both partners is ensured. Adhesion has been investigated by the start of delamination under a quasi-static tensile load of bar-shaped samples and began at 60 % strain. The cracking on the surface and in the cross-section of NR could be prevented for 111 h ageing at 75 pphm ozone concentration under cyclic deformation of $(12 \pm 5)\,\%$ strain. Below the coating, neither cracks nor any difference to pristine material could be identified using optical microscopy and IR measurements of the cross-section. Silicone coating is unaffected by the application temperature range, delivering constant protection over time without migration or consumption and possible application after vulcanisation. However, no combination with wax is reasonable as wax hinders the adhesion between the materials.

To successfully apply PDMS coatings in the industrial sector, several further aspects should be considered. Firstly, no protection against O_2 is expected due to the diffusion openness of silicone to O_2 and the adhesion has to be increased and tested for the application of close loadings that might include shear and abrasion.

The options to achieve better adhesion could include:

- Increasing the surface energy
- Roughening the surface
- Applying mechanical anchorage or a textured surface by the mould at the vulcanisation process

Since the measurements showed a strong deviation in the crack depth due to the artificial ageing process, conducting more measurements would be beneficial to reducing uncertainties. Moreover, long-term ageing under low ozone concentrations should be carried out in order to validate the extrapolation of evolution functions. The challenge is to either isolate the ozone ageing from other environmental impacts on NR in outdoor tests and using the chemically time-consuming ozone concentration measurement or to measure artificially generated ozone concentrations in the lab with the necessary accuracy rapidly enough to be able to regulate the system. In addition, the ozone concentration on the ground level fluctuates with daytime and season as it differs due to geographic location. Therefore, future research should deal with subsequent ageing sets based on the evaluation functions to include the diffusion-dependent change of crack evolution detected. Based on the FT-IR approach and results presented in this thesis, one should consider measurements with a resolution that enables a correlation of the changed layer depth to diffusion characteristics.

A
Data Tables

A.1 Fatigue Test Data

Table A.1 Cycles until failure and lifetime reduction according to the failure criterion described in Section 3.3.3.

	Unaged	Avg.	Scatter	Samples	
	150 N	9.20E+04	1.66	4	
	120 N	3.03E+05	1.65	4	
	100 N	5.99E+05	1.70	4	
No def.	Aged	Avg.	Scatter	Samples	Lifetime % :
75-111	150 N	8.36E+04	1.62	4	91
	120 N	2.48E+05	1.06	4	82
Stat. def.	Aged				
Ozone	Time	Avg.	Scatter	Samples	Lifetime % :
150	4	1.48E+05	1.30	4	49
150	8	7.27E+04	1.92	3	24
150	20	3.92E+04	1.99	3	13
150	24	3.05E+04	1.48	3	10
150	37	3.52E+04	2.78	3	12
150	55	1.48E+04	2.46	3	5
75	37	1.11E+05	1.61	3	36
75	55	1.00E+05	1.64	3	33
75	74	1.14E+05	2.11	3	38
75	111	1.33E+05	1.53	3	44

75	131	1.27E+05	1.76	3		42
75	168	1.22E+05	2.03	3		40
52	37	2.58E+05	1.51	3		85
52	74	2.16E+05	1.31	3		71
Dyn. def.	aged					
Ozone	Time	Avg.	Scatter	Samples	Avg. (Miner)	Lifetime % :
75	20	1.08E+05	1.49	4	1.15E+05	38
75	37	7.10E+04	1.19	4	7.98E+04	26
75	55	5.89E+04	1.75	4	7.06E+04	23
75	111	2.29E+04	4.23	4	3.44E+04	11
25	4	2.10E+05	1.31	4	2.13E+05	70
25	8	1.93E+05	1.13	4	1.98E+05	65
25	37	1.34E+05	1.55	4	1.51E+05	50
25	55	1.34E+05	1.71	4	1.60E+05	53
25	111	8.80E+04	1.97	4	1.32E+05	44

A.2 Correlation Parameters Between Ageing Parameters and Crack Depth

Table A.2 Pearson and Spearman correlation values and cosine similarity between ageing time and crack depth excluding crack depths for 75 pphm.

Crack depth / ageing time	Pearson		Spearman		Cosine
	r_P	p_P	r_{Sp}	p_{Sp}	r_{cos}
C3: static strain	1.98E-15	0.87	2.18E-18	0.90	0.93
C3: cyclic strain	5.96E-05	0.71	9.66E-10	0.90	0.86
C2: cyclic strain	5.09E-04	0.83	1.93E-04	0.86	0.94
C1: cyclic strain	5.23E-06	0.93	1.02E-05	0.92	0.95
All	5.01E-20	0.73	5.05E-28	0.82	0.88

Table A.3 Pearson and Spearman correlation values and cosine similarity between ozone concentration and crack depth without crack depths for 75 pphm.

Crack depth / ozone concentration	Pearson		Spearman		Cosine
	r_P	p_P	r_{Sp}	p_{Sp}	r_{cos}
C3: static strain	1.80E-02	0.34	4.00E-02	0.30	0.82
C3: cyclic strain	4.43E-02	0.34	1.97E-02	0.39	0.77

Crack depth / ozone concentration	Pearson		Spearman		Cosine
C2: cyclic strain	5.00E-02	0.46	7.48E-02	0.42	0.80
C1: cyclic strain	8.28E-02	0.41	2.00E-01	0.31	0.63
All	1.35E-06	0.38	2.74E-06	0.37	0.77

Table A.4 Pearson and Spearman correlation values and cosine similarity between ageing time resp. ozone concentration and crack depth.

Normalised data to 111 h resp. 52 pphm	Pearson		Spearman		Cosine
	r_P	p_P	r_{Sp}	p_{Sp}	r_{cos}
Crack depth / ageing time	7.67E-44	0.95	1.12E-46	0.96	0.96
Crack depth / ozone concentration	5.41E-16	0.73	5.06E-25	0.84	0.97

A.3 Simulation of Crack Depth – Parameters over Time

Table A.5 Fit parameters m and s for `LN+`, Eq. 4.11 using `C3stat` for 25 – 75 pphm ozone concentration displayed in Figure 4.4.

Ozone concentration	m	s	RMSE
25 pphm	1.27×10^{2}	4.93×10^{-2}	55.9
36 pphm	1.39×10^{2}	6.99×10^{-2}	82.4
52 pphm	1.80×10^{2}	8.06×10^{-2}	103.7
52 (linear parameters) pphm	1.55×10^{2}	9.24×10^{-2}	
75 pphm	1.77×10^{2}	1.29×10^{-1}	118.3

Table A.6 Fit parameters m and s for `LN+` displayed in Figure 4.5 and $t_{\mathrm{cd,max}}$ and k for `EXP` and p and q for `LIN` using `C3cyc30` and `C3cyc20` for 25 – 75 pphm ozone concentration.

Database	`C3cyc30`			`C3cyc20`		
`LN+`	m	s	RMSE	m	s	RMSE
25 pphm	8.27×10^{1}	1.03×10^{-1}	17.6	1.42×10^{2}	6.51×10^{-2}	26.1
36 pphm	9.89×10^{1}	9.62×10^{-2}	23.1	3.83×10^{2}	3.46×10^{-2}	14.3
52 pphm	1.09×10^{2}	1.63×10^{-1}	18.5	1.43×10^{3}	7.82×10^{-3}	55.7
75 pphm	1.18×10^{2}	2.23×10^{-1}	29.6	4.16×10^{2}	7.06×10^{-2}	47.4

Database	`C3cyc30`			`C3cyc20`		
`EXP`	$t_{\text{cd,max}}$	k	RMSE	$t_{\text{cd,max}}$	k	RMSE
25 pphm	1.86×10^{2}	3.58×10^{-2}	13.6	3.25×10^{2}	2.28×10^{-2}	13.2
36 pphm	2.63×10^{2}	2.30×10^{-2}	57.8	7.48×10^{2}	1.48×10^{-2}	16.0
52 pphm	3.39×10^{2}	2.68×10^{-2}	60.8	1.88×10^{3}	5.80×10^{-3}	58.4
75 pphm	3.94×10^{2}	3.07×10^{-2}	76.3	1.01×10^{3}	2.02×10^{-2}	92.7
`LIN`	p	q	RMSE	p	q	RMSE
25 pphm	5.03×10^{1}	-4.58×10^{-1}	23.0	9.84×10^{1}	-1.65×10^{2}	57.9
36 pphm	6.38×10^{1}	-5.74×10^{-1}	25.1	2.13×10^{2}	-3.97×10^{2}	218.4
52 pphm	8.72×10^{1}	-8.87×10^{-1}	42.1	3.38×10^{2}	-7.01×10^{2}	575.1
75 pphm	9.68×10^{1}	-8.75×10^{-1}	51.1	2.98×10^{2}	-5.00×10^{2}	361.1

Table A.7 Fit parameters m and s for `LN+` displayed in Figure 4.6 and $t_{\text{cd,max}}$ and k for `EXP` using `C2stat` for 36 – 75 pphm ozone concentration.

Database	`C2stat`		
`LN+`	m	s	RMSE
36 pphm	1.10×10^{2}	7.02×10^{-2}	11.6
52 pphm	1.76×10^{2}	4.26×10^{-2}	10.9
75 pphm	5.59×10^{2}	2.42×10^{-2}	50.4
`EXP`	$t_{\text{cd,max}}$	k	RMSE
36 pphm	2.59×10^{2}	2.33×10^{-2}	3.10
52 pphm	3.68×10^{2}	1.64×10^{-2}	20.4
75 pphm	9.83×10^{2}	1.22×10^{-2}	63.4

Table A.8 Fit parameters D and k for `EXP` and `LN+` for `C2cyc30` and `POW` for `C1cyc30` for 25 – 75 pphm ozone concentration displayed in Figure 4.7.

Database	`C2cyc30`			`C1cyc30`			
`EXP`	$t_{\text{cd,max}}$	k	RMSE	`POW`	g	n	RMSE
25 pphm	1.44×10^{5}	8.56×10^{-6}	34.3		2.65	6.78×10^{-4}	7.50
36 pphm	2.24×10^{2}	1.97×10^{-2}	49.8		1.55	1.29×10^{-1}	53.6
52 pphm	5.43×10^{2}	7.86×10^{-3}	16.0		1.39	3.74×10^{-1}	4.00
75 pphm	1.60×10^{3}	3.58×10^{-3}	53.6		1.66	3.98×10^{-1}	28.7

Database	`C2cyc30`			`C1cyc30`
`LN+`	m	s	RMSE	
25 pphm	7.76×10^{4}	1.64×10^{-5}	55.5	
36 pphm	8.95×10^{1}	7.42×10^{-2}	51.8	
52 pphm	3.75×10^{2}	1.19×10^{-2}	21.2	
75 pphm	1.33×10^{3}	4.33×10^{-3}	52.4	

A.4 Simulation of Crack Depth – Parameters over Ozone

Table A.9 Fit parameters b and f for `LR` using `C3stat` for 4 – 111 hours displayed in Figure 4.9.

Database	`C3stat`		
	b	f	adj r^2
4 hours	1.67	-1.76×10^{1}	0.74
12 hours	2.74	-9.52	0.48
37 hours	4.92	-3.50×10^{-14}	0.68
111 hours	8.32	-1.44×10^{-11}	0.87

Table A.10 Fit parameters b and f for `LR` using `C3cyc30` and `C3cyc20` for 4 – 111 hours displayed in Figure 4.10.

Database	`C3cyc30`			`C3cyc20`		
	b	f	adj r^2	b	f	adj r^2
4 hours	1.13	-6.61	0.94	2.29	-4.13×10^{1}	0.99
12 hours	2.52	-1.37×10^{-12}	0.89	3.16	-7.14×10^{-10}	0.45
37 hours	4.11	-8.33×10^{-14}	0.78	7.04	-4.36×10^{-13}	0.72
111 hours	6.20	-5.47×10^{-14}	0.91	2.11×10^{1}	-1.94×10^{2}	0.97

Table A.11 Fit parameters b and f for `LR` using `C2cyc30` and `C1cyc30` for 12 – 111 hours displayed in Figure 4.11.

Database	`C2cyc30`			`C1cyc30`		
	b	f	adj r^2	b	f	adj r^2
12 hours	80.8	-2.24×10^{-14}	0.74			
37 hours	3.62	-4.88×10^{1}	0.94	1.75	-3.40×10^{1}	0.97

	`C2cyc30`					
Database				`C1cyc30`		
75 hours	5.66	-4.43×10^{1}	0.95	3.30	-1.94×10^{1}	0.07
111 hours	6.38	-1.91×10^{1}	0.97	51.3	-3.16×10^{-14}	0.58

Bibliography

[1] **T. Gehling, J. Schieppati, W. Balasooriya, R. C. Kerschbaumer, and G. Pinter**, "Fatigue behavior of elastomeric components: A review of the key factors of rubber formulation, manufacturing, and service conditions," *Polym. Rev.*, vol. 63, no. 3, pp. 763–804, 2023. DOI: `https://doi.org/10.1080/15583724.2023.2166955`.

[2] **M. Braden and A. Gent**, "The attack of ozone on stretched rubber vulcanizates. I. The rate of cut growth.," *J. Appl. Polym. Sci.*, vol. 3, no. 7, pp. 90–99, 1960.

[3] **W. V. Mars and A. Fatemi**, "Multiaxial fatigue of rubber: Part II: Experimental observations and life predictions," *Fatigue Fract. Eng. Mater. Struct.*, vol. 28, no. 6, pp. 523–538, 2005.

[4] **M. J. Bhala**, "Non-migratory antiozonant system for natural rubber," Ph.D. dissertation, Loughborough University, 1997.

[5] **J. Verdu**, *Oxidative Ageing of Polymers*. John Wiley & Sons, 2012.

[6] **WTEx**, *Distribution of natural rubber exports based on value in 2022, by country*, Accessed 21 Feb 2024, Statista: WTEx, Sep. 2023. [Online]. Available: `https://www.statista.com/statistics/275399/world-consumption-of-natural-and-synthetic-caoutchouc/`.

[7] **H. E. Warmke**, "Experimental Polyploidy and Rubber Content in *Taraxacum kok-saghyz*," *Bot. Gaz.*, vol. 103, no. 3, 1945. DOI: `10.1086/335301`.

[8] **J. B. van Beilen and Y. Poirier**, "Guayule and russian dandelion as alternative sources of natural rubber," *Crit. Rev. Biotechnol.*, vol. 27, no. 4, pp. 217–231, 2007. DOI: `10.1080/07388550701775927`.

[9] **T. Schmidt, M. Lenders, A. Hillebrand, N. van Deenen, O. Munt, R. Reichelt, W. Eisenreich, R. Fischer, D. Prüfer, and C. S. Gronover**, "Characterization of rubber particles and rubber chain elongation in taraxacum koksaghyz," *BMC Biochem.*, vol. 11, no. 1, pp. 1–11, 2010.

[10] **M. Salehi, M. Bahmankar, M. R. Naghavi, and K. Cornish**, "Rubber and latex extraction processes for taraxacum kok-saghyz," *Ind. Crop. Prod.*, vol. 178, p. 114 562, 2022, ISSN: 0926-6690. DOI: `https://doi.org/10.1016/j.indcrop.2022.114562`.

[11] **J. E. Puskas, K. Cornish, B. Kenzhe-Karim, M. Mutalkhanov, G. Kaszas, and K. Molnar**, "Natural rubber – Increasing diversity of an irreplaceable renewable resource," *Heliyon*, vol. 10, no. 3, 2024.

[12] **Malaysian Rubber Board**, *Consumption of natural and synthetic rubber worldwide from 1990 to 2022 (in million metric tons)*, Accessed 20 Feb 2024, Statista: Malaysian Rubber Board, Jul. 2023. [Online]. Available: `https://www.statista.com/statistics/275399/world-consumption-of-natural-and-synthetic-caoutchouc/`.

[13] **W. Andrew**, *Service Life Prediction of Polymers and Plastics Exposed to Outdoor Weathering*, **C. C. White, K. M. White, and J. E. Pickett**, Eds. 2017, ISBN: 978-0-323-49776-3.

[14] **M. Zaghdoudi, A. Kömmling, M. Jaunich, and D. Wolff**, "Oxidative ageing of elastomers: Experiment and modelling," *Continuum Mech. Therm.*, vol. 36, no. 2, pp. 289–297, 2024. DOI: `https://doi.org/10.1007/s00161-022-01093-9`.

[15] **M. Coja and L. Kari**, "Using waveguides to model the dynamic stiffness of pre-compressed natural rubber vibration isolators," *Polymers*, vol. 13, no. 11, p. 1703, 2021. [Online]. Available: `https://doi.org/10.3390/polym13111703`.

[16] **M. Vizcaíno-Vergara, L. Kari, L. B. Tunnicliffe, and J. J. C. Busfield**, "Evolution of the viscoelastic properties of filler reinforced rubber under physical aging at room temperature," *Polymers*, 2023.

[17] **L. R. G. Treloar**, *The Physics of Rubber Elasticity*, Third Edition. Clarendon Press Oxford, 1975.

[18] **S. K. De, J. R. White, and K. Naskar**, *Rubber technologist's handbook, Volume 2*. Rapra Technology Limited, 2001, ISBN: 1-84735-101-8.

[19] **R. Brown**, *Physical Testing of Rubber*. Springer Science and Business Media, 2006.

[20] **A. N. Gent**, *Engineering with rubber*. Carl Hanser Verlag, München, 2012.

[21] **M. J. Forrest**, *Rubber Analysis: Characterisation, Failure Diagnosis and Reverse Engineering*, 2nd ed. Walter de Gruyter GmbH & Co KG, 2019, ISBN: 978-3-11-064027-4.

[22] **K. Loos, A. B. Aydogdu, A. Lion, M. Johlitz, and J. Calipel**, "Strain-induced crystallisation in natural rubber: A thermodynamically consistent model of the material behaviour using a serial connection of phases," *Continuum Mech. Therm.*, vol. 33, pp. 1107–1140, 2021.

[23] **J. S. Murphy and J. R. Orr**, *Ozone chemistry and technology. A review of the literaure: 1961–1974*. The Franklin Institute Press, Philadelphia, 1975.

[24] **United States Environmental Protection Agency**, *NAAQS table*, Accessed 20 Feb 2024. [Online]. Available: `https://www.epa.gov/criteria-air-pollutants/naaqs-table`.

[25] **Bundesumweltamt**, *Aktuelle Luftdaten*, Accessed 02 Apr 2024, Aug. 2023. [Online]. Available: `www.umweltbundesamt.de/daten/luft/luftdaten/karten`.

[26] **D. Brück**, "Ozonolyse von ungesättigten Kautschuken und Vulkanisatenein überblick," *KGK, Kautsch. Gummi Kunstst.*, vol. 42, no. 9, pp. 760–770, 1989.

[27] **N. M. Huntink, R. N. Datta, and J. W. M. Noordermeer**, "Addressing durability of rubber compounds," *Rubber Chem. Technol.*, vol. 77, no. 3, pp. 476–511, 2004.

[28] **P. Charrier, Y. Marco, V. L. Saux, and R. K. P. S. Ranawerra**, "On the influence of heat ageing on filled NR for automotive AVS applications," in *Constitutive Models for Rubber VII: Proceedings of the 7th European Conference on Constitutive Models for Rubber*, 2012, pp. 381–388.

[29] **R. Criegee**, "Mechanism of ozonolysis," *Angew. Chem. Int. Edition 14*, vol. 14, no. 11, pp. 745–752, 1975.

[30] **F. Cataldo**, "Protection mechanism of rubbers from ozone attack," *Ozone: Sci. Eng.*, vol. 41, no. 4, pp. 358–368, 2019.

[31] **J. Lemaire, J.-l. Gardette, and J. Lacoste**, "Use of micro-ftir spectrophotometry in the determination of polymer photoageing mechanisms," *Makromol. Chem., Macromol. Symp.*, vol. 431, pp. 419–431, 1993.

[32] **W. V. Mars and A. Fatemi**, "Factors that affect the fatigue life of rubber: A literature survey," *Rubber Chem. Technol.*, 2004.

[33] **S. B. Christian Geletneky**, "The mechanism of ozonolysis revisited by 17o-nmr spectroscopy," *Eur. J. Org. Chem.*, no. 8, pp. 1625–1627, 1998.

[34] **T. Zheng, X. Zheng, S. Zhan, J. Zhou, and S. Liao**, "Study on the ozone aging mechanism of natural rubber," *Polym. Degrad. Stab.*, vol. 186, p. 109 514, 2021, ISSN: 0141-3910.

[35] **F. H. Kendall and J. Mann**, "Reaction of ozone with natural hevea and acrylonitrile-butadiene rubbers.," *J. Polym. Sci.*, vol. 19, no. 93, pp. 503–518, 1956.

[36] **F. Cataldo**, "Early stages of p-phenylenediamine antiozonants reaction with ozone: Radical cation and nitroxyl radical formation," *Polym. Degrad. Stab.*, vol. 147, pp. 132–142, Jan. 2018.

[37] **F. H. A. Rodrigues, E. F. Santos, J. P. A. Feitosa, N. M. P. S. Ricardo, and R. C. M. D. Paula**, "Ozonation of unstretched natural rubber: Part i. effect of film thickness," *Rubber Chem. Technol.*, vol. 74, no. 1, pp. 57–68, 2001.

[38] **J. L. Bolland**, "Kinetics of olefin oxidation," *Q. Rev. Chem. Soc.*, vol. 3, no. 1, pp. 1–21, 1949.

[39] **M. Edge, N. S. Allen, R. Gonzalez-Sanchez, C. M. Liauw, S. J. Read, and R. B. Whitehouse**, "The influence of cure and carbon black on the high temperature oxidation of natural rubber I. Correlation of physico-chemical changes," *Polym. Degrad. Stabil.*, vol. 64, pp. 197–205, 1998.

[40] **M. Celina and K. T. Gillen**, "Advances in exploring mechanistic variations in thermal aging of polymers," in *Service Life Prediction of Polymeric Materials*, **J. W. Martin, R. A. Ryntz, J. Chin, and R. A. Dickie**, Eds., Boston: Springer, 2009, pp. 45–56, ISBN: 978-0-387-84876-1.

[41] **A. Herzig, M. Johlitz, and A. Lion**, "Experimental investigation on the consumption of oxygen and its diffusion into elastomers during the process of ageing," in *Proceedings of the 9th European Conference on Constitutive Models for Rubber (ECCMR)*, vol. 9, 2015, pp. 23–28.

[42] **M. Johlitz**, *Zum Alterungsverhalten von Polymeren: Experimentell gestützte, thermo-chemomechanische Modellbildung und numerische Simulation*. Universität der Bundeswehr München, 2016.

[43] **M. Broudin, Y. Marco, V. LeSaux, P. Charrier, W. Hervouet, and P. Y. LeGac**, "Investigation of thermo-oxidative ageing effects on the fatigue design of automotive anti-vibration parts," *MATEC Web of Conferences*, vol. 165, no. 08004, 2018.

[44] **B. Musil**, "Ein Beitrag zur experimentell gestützten Modellierung der chemo-thermomechanischen Alterung von Nitrilkautschuk," Ph.D. dissertation, Neubiberg, Universität der Bundeswehr München, 2020.

[45] **A. Früh, H.-J. Egelhaaf, and H. Hintz**, "PMMA as an effective protection layer againt the oxidation of P3HT and MDMO-PPV by ozone," *J. Mater. Res.*, vol. 33, no. 13, pp. 1891–1901, 2018.

[46] **Y. Iwase, T. Shindo, H. Kondo, Y. Ohtake, and S. Kawahara**, "Ozone degradation of vulcanized isoprene rubber as a function of humidity," *Polym. Degrad. Stabil.*, vol. 142, pp. 209–216, Aug. 2017.

[47] **S. Kamaruddin and A. H. Muhr**, "Investigation of ozone cracking on natural rubber," *J. Rubber Res.*, vol. 21, no. 2, pp. 73–93, 2018.

[48] **DIN ISO 1431-1**, *Rubber, vulcanized or thermoplastic - resistance to ozone cracking - part 1: Static and dynamic strain testing (ISO 1431-1:2012)*, Standard, Deutsches Institut für Normung e. V., 2017.

[49] **DIN ISO 1431-3**, *Rubber, vulcanized or thermoplastic - resistance to ozone cracking - part 3: Reference and alternative methods for determining the ozone concentration in laboratory test chambers (ISO 1431-3:2017)*, Standard, Deutsches Institut für Normung e. V., 2021.

[50] **P. H. Mott and C. M. Roland**, "Ozone detection by crack-induced opacity in rubber," *Rubber Chem. Technol.*, vol. 72, no. 4, pp. 769–778, 1999.

[51] **J. Spreckels**, "Ein Beitrag zur Berücksichtigung von Alterungs- und Umwelteinflüssen bei der Lebensdauerprüfung von Elastomerbauteilen," Ph.D. dissertation, TU Hamburg-Harburg, 2013.

[52] **A. Herzig**, "Thermo-oxidative ageing of elastomers. A contribution to the experimental investigation and modelling," Ph.D. dissertation, Universität der Bundeswehr München, 2020.

[53] **C. Neuhaus**, "Methodenentwicklung für die Lebensdaueruntersuchung thermomechanisch beanspruchter Elastomerlager," Ph.D. dissertation, Universität der Bundeswehr München, 2019.

[54] **X. Colin, L. Audouin, M. L. Huy, and J. Verdu**, "Kinetic modelling of the thermal oxidation of polyisoprene elastomers. Part 2: Effect of sulfur vulcanization on mass changes and thickness distribution of oxidation products during thermal oxidation," *Polym. Degrad. Stabil.*, vol. 92, pp. 898–905, 2007.

[55] **S. Kamaruddin, P. Y. Le Gac, Y. Marco, and A. H. Muhr**, "Formation of crust on natural rubber after ageing," in *Proceedings of the 7th European Conference on Constitutive Models for Rubber (ECCMR)*, 2011, pp. 197–202.

[56] **Q. L. Zhao, X. G. Li, and J. Gao**, "Aging of ethylene–propylene-diene monomer (EPDM) in artificial weathering environment," *Polym. Degrad. Stab.*, vol. 92, no. 10, pp. 1841–1846, 2007.

[57] **T. Jared, D. D'hooge, N. Bosco, C. Delgado, and R. Dauskardt**, "Evaluating and predicting molecular mechanisms of adhesive degradation during field and accelerated aging of photovoltaic modules," *Prog. Photovolt.*, vol. 26, no. 12, pp. 981–993, 2018, ISSN: 1099-159X. DOI: `10.1002/pip.3045`.

[58] **K. T. Gillen, R. L. Clough, and C. A. Quintana**, "Modulus profiling of polymers," *Polym. Degrad. Stabil.*, vol. 17, no. 1, pp. 31–47, 1987.

[59] **R. L. Clough and K. T. Gillen**, "Polymer degradation under ionizing radiation: The role of ozone," *J. Polym. Sci. Pol. Chem.*, vol. 27, no. 7, pp. 2313–2324, 1989, ISSN: 1099-0518. DOI: `10.1002/pola.1989.080270715`.

[60] **K. Geels, D. B. Fowler, W. U. Kopp, and M. Rückert**, *Metallographic and materialographic specimen preparation, light microscopy, image analysis, and hardness testing*. ASTM international West Conshohocken, 2007, vol. 46.

[61] **J. C. Andries, D. B. Ross, and H. E. Diem**, "Ozone attack and antiozonant protection of vulcanized natural rubber. A surface study by attenuated total reflectance spectroscopy.," *Rubber Chem. Technol.*, vol. 48, no. 1, pp. 41–49, 1975.

[62] **R. G. Newton**, "Mechanism of exposure-cracking of rubbers. With a review of the influence of ozone," *Rubber Chem. Technol.*, vol. 18, no. 3, pp. 504–556, 1945.

[63] **D. J. Buckley and S. B. Robison**, "Ozone Attack on Rubber Vulcanizates," *J. Polym. Sci.*, vol. 19, no. 91, pp. 145–158, 1956.

[64] **M. Braden and A. Gent**, "The attack of ozone on stretched rubber vulcanizates. II. Conditions for cut growth," *J. Appl. Polym. Sci.*, vol. 3, no. 7, pp. 100–106, 1960.

[65] **M. Braden and A. Gent**, "The attack of ozone on stretched rubber vulcanizates. III. Actions of antiozonants," *J. Appl. Polym. Sci.*, vol. 6, no. 22, pp. 449–455, 1962.

[66] **E. H. Andrews and M. Braden**, "The reaction of ozone with surfaces of natural rubber, and its dependence upon strain," *J. Polym. Sci.*, vol. 55, no. 162, pp. 787–798, 1961.

[67] **E. H. Andrews and M. Braden**, "The surface reaction of ozone with chemically protected rubber," *J. Appl. Polym. Sci.*, vol. 7, no. 3, pp. 1003–1013, 1963.

[68] **G. J. Lake**, "Ozone cracking and protection of rubber," *Rubber Chem. Technol.*, vol. 43, no. 5, pp. 1230–1254, 1970.

[69] **G. J. Lake and P. B. Lindley**, "Role of Ozone in Dynamic Cut Growth of Rubber," *J. Appl. Polym. Sci.*, 1965.

[70] **J. Schieppati, B. Schrittesser, S. Tagliabue, L. Andena, A. Holzner, J. Poduška, and G. Pinter**, "Fatigue analysis and defect size evaluation of filled NBR including temperature influence," *Materials*, vol. 15, no. 11, p. 3745, 2022.

[71] **M. Flamm, J. Spreckels, T. Steinweger, and U. Weltin**, "Effects of very high loads on fatigue life of NR elastomer materials," *Int. J. Fatigue*, vol. 33, no. 9, pp. 1189–1198, 2011.

[72] **J. Schieppati, B. Schrittesser, A. Wondracek, S. Robin, A. Holzner, and G. Pinter**, "Impact of temperature on the fatigue and crack growth behavior of rubbers," *Procedia Structural Integrity*, vol. 13, pp. 642–647, 2018.

[73] **R. J. Harbour, A. Fatemi, and W. V. Mars**, "Fatigue crack growth of filled rubber under constant and variable amplitude loading conditions," *Fatigue Fract. Eng. Mater. Struct.*, vol. 30, no. 7, pp. 640–652, 2007, ISSN: 8756-758X.

[74] **S. Beurrot, B. Huneau, and E. Verron**, "In Situ SEM Study of Fatigue Crack Growth Mechanismin Carbon Black-Filled Natural Rubber," *J. Appl. Polym. Sci.*, vol. 117, no. 3, pp. 1245–1866, 2010.

[75] **A. Schmid, B. Seufert, Z. Pezelj, U. Weltin, and J. Spreckels**, "Kundennaher Betriebsfestigkeitsnachweis von Elastomerbauteilen im Fahrwerksbereich unter Berücksichtigung von Alterung und Ermüdung," *Mater. Test.*, vol. 52, no. 07-08, pp. 543–548, 2010.

[76] **P. M. Lewis**, "Effect of ozone on rubbers: Countermeasures and unsolved problems," *Polym. Degrad. Stab.*, vol. 15, no. 1, pp. 33–66, 1986.

[77] **S. D. Razumovskii and D. M. Lisitsyn**, "Reactions of ozone with double bonds in polymer and biosystem chemistry," *Polym. Sci. Ser. A*, vol. 50, no. 12, pp. 1187–1197, 2008, ISSN: 0965-545X. DOI: `10.1134/S0965545X08120018`.

[78] **F. Röthemeyer and F. Sommer**, *Kautschuktechnologie*. Hanser Verlag, 2006.

[79] **R. N. Datta, N. M. Huntink, S. Datta, and A. G. Talma**, "Rubber vulcanizates degradation and stabilization," *Rubber Chem. Technol.*, vol. 80, no. 3, pp. 436–480, 2007.

[80] **C. Treib and M. Johlitz**, "Ozone ageing of polydimethylsiloxane coated natural rubber," in *Consitutive Models for Rubber XII*, CNC Press Taylor and Francis Group, 2022, pp. 408–414.

[81] **F. Ignatz-Hoover, B. H. To, R. N. Datta, A. J. De Hoog, N. M. Huntink, and A. G. Talma**, "Chemical additives migration in rubber," *Rubber Chem. Technol.*, vol. 76, no. 3, pp. 747–768, 2003.

[82] **L. Nasdala**, "Ein viskoelastisches Schädigungsgesetz für den stationär rollenden Reifen," Ph.D. dissertation, Universität Hannover, 2000.

[83] **G. Salomon and F. V. Bloois**, "The mechanism of ozone cracking. I. Ozone cracking of plastic films," *J. Appl. Polym. Sci.*, vol. 7, no. 3, pp. 1117–1132, 1963.

[84] **P. H. Mott and C. M. Roland**, "Aging of natural rubber in air and seawater," *Rubber Chem. Technol.*, vol. 74, no. 1, pp. 79–88, 2001.

[85] **S. Kamaruddin, A. H. Muhr, P. Y. L. Gac, Y. Marco, and V. L. Saux**, "Modelling naturally aged NR mouldings," in *Proceedings of the 8th European Conference on Constitutive Models for Rubber (ECCMR)*, London: CRC Pr I Llc., Jun. 2013, pp. 37–42.

[86] **G. Ehrenstein and S. Pongratz**, *Beständigkeit von Kunststoffen*. Carl Hanser Verlag, 2007.

[87] **T. H. Larsen and E. M. Furst**, "Microrheology of the liquid-solid transition during gelation.," *Phys. Rev. Lett.*, vol. 100, no. 14, p. 146 001, 2008.

[88] **M. Celina, K. T. Gillen, and R. A. Assink**, "Accelerated aging and lifetime prediction: Review of non-Arrhenius behaviour due to two competing processes," *Polym. Degrad. Stabil.*, vol. 90, no. 3, pp. 395–404, 2005.

[89] **J. M. Pérez *et al.***, "Effect of reprocessing and accelerated ageing on thermal and mechanical polycarbonate properties," *J. Mater. Process. Technol.*, vol. 210, no. 5, pp. 727–733, 2010.

[90] **T. W. Dakin**, "Electrical insulation deterioration treated as a chemical rate phenomenon," *Trans. Am. Inst. Electr. Eng.*, vol. 67, no. 1, pp. 113–122, 1948.

[91] **K. T. Gillen, R. Bernstein, and M. Celina**, "Die Herausforderungen beschleunigter Alterungsverfahren für die Vorhersage der Elastomerlebensdauer - Teil 1," *Gummi Fasern Kunstst.*, 2016.

[92] **C. Treib, A. Lion, and M. Johlitz**, "FT-IR Microscopic Analysis of the Chemical Change in the Molecular Structure after Ozone Ageing of Natural Rubber," in *Lectures Notes on Advanced Structured Materials*, Springer, 2022, pp. 241–252.

[93] **Y. S. Zuev and S. I. Pradvednikova**, "Influence of Concentration of Ozone upon Cracking of Vulcanized Rubber," *Rubber Chem. Technol.*, 1962.

[94] **B. Dolezel**, *Die Beständigkeit von Kunststoffen und Gummi*. Carl Hanser Verlag, 1978.

[95] **K. Nonnenmacher**, "Dynamic rubber test by ozone," *KGK. Kautschuk, Gummi, Kunststoffe*, vol. 61, no. 5, pp. 230–232, 2008.

[96] **P. B. Lindley**, "Relation between hysteresis and the dynamic crack growth resistance of natural rubber," *Int. J. Fracture*, vol. 9, no. 4, pp. 449–462, 1973. DOI: `10.1007/bf00036325`.

[97] **D. Ehrhardt**, "Einige kritische Bemerkungen zum statisch-mechanischen Ozonkammertest," *KGK, Kautsch. Gummi Kunstst.*, vol. 50, no. 8, pp. 614–618, 1997.

[98] **C. S. Gronover, D. Wahler, and D. Prüfer**, "Natural rubber biosynthesis and physic-chemical studies on plant derived latex," in **M. Elnashar**, Ed. InTech, 2011, ch. 4, pp. 75–88, ISBN: 978-953-307-179-4.

[99] **J. B. V. Beilen and Y. Poirier**, "Production of renewable polymers from crop plants," *Plant J.*, vol. 54, no. 4, pp. 684–701, 2008.

[100] **P. J. Crutzen, M. G. Lawrence, and U. Pöschl**, "On the background photochemistry of tropospheric ozone," *Tellus B.*, vol. 51, no. 1, pp. 123–146, 1998.

[101] **Bayerisches Landesamt für Umwelt (LfU)**, *Langzeitverläufe der Schadstoffbelastung an den bayerischen LÜB-Messstationen*, Accessed 16 Nov 2021, Bürgermeister-Ulrich-Straße 160, 86179 Augsburg, Jul. 2020. [Online]. Available: `www.lfu.bayern.de`.

[102] **J. H. Seinfeld**, "Urban air pollution: State of the science," *Science*, vol. 243, no. 4892, pp. 745–752, 1989, American Association for the Advancement of Science. DOI: `10.1126/science.243.4892.745`.

[103] **J. F. da Silveira Petruci, D. N. Barreto, M. A. Dias, E. P. Felix, and A. A. Cardoso**, "Analytical methods applied for ozone gas detection: A review," *Trends Anal. Chem.*, vol. 149, pp. 1–9, 2022. [Online]. Available: `https://doi.org/10.1016/j.trac.2022.116552`.

[104] **Bayerisches Landesamt für Umwelt (LfU)**, *Faktenblatt Ozon*, Accessed 16 Nov 2021, Bürgermeister-Ulrich-Straße 160, 86179 Augsburg, 2018. [Online]. Available: `www.lfu.bayern.de`.

[105] **United States Environmental Protection Agency**, *Ground-level Ozone Basics*, Accessed 05 Feb 2023, United States Environmental Protection Agency, May 2021. [Online]. Available: `https://www.epa.gov/ground-level-ozone-pollution/ground-level-ozone-basics`.

[106] **G. J. Lake and P. G. Mente**, "Ozone Cracking and Protection of Elastomers at High and Low Temperatures," *J. nat. Rubb. Res.*, vol. 7, no. 1, pp. 1–13, 1992.

[107] **G. Salisbury, A. R. Rickard, P. S. Monks, B. J. Allan, S. Bauguitte, S. A. Penkett, N. Carslaw, A. C. Lewis, D. J. Creasey, D. E. Heard, P. J. Jacobs, and J. D. Lee**, "Production of peroxy radicals at night via reactions of ozone and the nitrate radical in the marine boundary layer," *J. Geophys. Res.*, vol. 106, no. D12, pp. 12 669–12 687, 2001, ISSN: 0148-0227. DOI: `10.1029/2000JD900754`.

[108] **Europen Environment Agengy**, *Air quality statistics*, Accessed 02 Apr 2024, 2024. [Online]. Available: `https://www.eea.europa.eu/data-and-maps/dashboards/air-quality-statistics`.

[109] **P. E. Karlsson, J. Klingberg, M. Engardt, C. Andersson, J. Langner, G. P. Karlsson, and H. Pleijel**, "Past, present and future concentrations of ground-level ozone and potential impacts on ecosystems and human health in northern europe," *Sci. Total Environ.*, vol. 576, pp. 22–35, 2017.

[110] **M. Kruza, A. C. Lewis, G. C. Morrison, and N. Carslaw**, "Impact of surface ozone interactions on indoor air chemistry: A modeling study," *Indoor Air*, vol. 27, no. 5, pp. 1001–1011, 2017.

[111] **S. Mitra, A. Ghanbari-Siahkali, and K. Almdal**, "A novel method for monitoring chemical degradation of crosslinked rubber by stress relaxation under tension," *Polym. Degrad. Stabil.*, vol. 91, pp. 2520–2526, 2006.

[112] **S. Nie, J. Lacayo-Pineda, N. Willenbacher, and M. Wilhelm**, "Aging of natural rubber studied via Fourier-transform rheology and double quantum NMR to correlate local chain dynamics with macroscopic mechanical response," *Polymer*, vol. 181, no. 121804, 2019.

[113] **C. Neuhaus, A. Lion, and M. Johlitz**, "Influence of thermo-oxidative ageing on fatigue-lifetime of NR," in *Proceedings of the 9th European Conference on Constitutive Models for Rubber (ECCMR)*, vol. 9, 2015, pp. 429–432.

[114] **A. R. Azura, A. H. Muhr, and A. G. Thomas**, "Diffusion and reactions of oxygen during ageing for conventionally cured natural rubber vulcanisate," *Polym.-Plast. Technol. Eng.*, vol. 45, no. 7, pp. 893–896, 2006.

[115] **K. T. Gillen, M. Celina, and R. Bernstein**, "Validation of improved methods for predicting long-term elastomeric seal lifetimes from compression stress-relaxation and oxygen consumption techniques," *Polym. Degrad. Stabil.*, vol. 82, no. 1, pp. 25–35, 2003.

[116] **U. Tamm**, "Beseitigung von organischen Schadstoffen in Abgasen durch Oxidation mit Ozon," Ph.D. dissertation, Martin-Luther-Universität Halle-Wittenberg, Nov. 2002.

[117] **D. 53504:2017-03**, *Testing of rubber - Determination of tensile strength at break, tensile stress at yield, elongation at break and stress values in a tensile test*, Standard, Deutschen Instituts für Normung, 2017.

[118] **D. O. Hummel**, *Atlas der Kunststoffanalyse*. Hanser, 1968.

[119] **J. Bergström**, *Mechanics of Solid Polymers - Theory and Computational Modeling*. Elsevier, William Andrew, 2015.

[120] **S. E. Gustafsson**, “Transient plane source techniques for thermal conductivity and thermal diffusivity measurements of solid materials,” *Rev. Sci. Instrum.*, vol. 62, no. 3, pp. 797–804, 1991.

[121] **J.-B. L. Cam**, “Endommagement en fatigue des élastomères,” Ph.D. dissertation, Ecole Centrale de Nates, 2005.

[122] **A. Palmgren**, *Die Lebensdauer von Kugellagern*. VDI, 1924.

[123] **M. Miner**, “Cumulative damage in fatigue,” *J. Appl. Math.*, 1945.

[124] **E. Haibach**, *Betriebsfestigkeit: Verfahren und Daten zur Bauteilberechnung*. Springer-Verlag, Berlin, 1989.

[125] **L. Mullins**, “Effect of stretching on the properties of rubber,” *Rubber Chem. Technol.*, vol. 21, pp. 281–300, 1948.

[126] **G. Marckmann and E. Verron**, “Comparison of hyperelastic models for rubberlike materials,” *Rubber Chem. Technol.*, vol. 79, pp. 835–858, 2006.

[127] **A. Charvet, C. Vergelati, P. Sotta, and D. R. Long**, “Damage mechanisms of plasticized cellulose acetate under tensile deformation studied by ultrasmall-angle x-ray scattering,” *Macromolecules*, vol. 52, pp. 6613–6632, 2019.

[128] **H. P. Latscha and U. Kazmaier**, “Chemie für Biologen,” in Springer-Verlag GmbH Berlin Heidelberg, 2016, ch. 12, Kinetik chemischer Reaktionen, pp. 201–216, ISBN: 978-3-662-47783-0. DOI: `10.1007/978-3-662-47784-7`.

[129] **M. Baerns, A. Behr, A. Brehm, J. Gmehling, K.-O. Hinrichsen, H. Hofmann, M. Kleiber, N. Kockmann, U. Onken, R. Palkovits, A. Renken, and D. Vogt**, *Technische Chemie*. John Wiley & Sons, 2023.

[130] **M. Lang**, *Datenkompetenz*. Carl Hanser Verlag Munchen, 2023, ISBN: 978-3-446-47585-4.

[131] **T. DelSole and M. Tippett**, *Statistical Methods for Climate Scientists*. Cambridge University Press, 2022, ISBN: 9781108659055. DOI: `https://doi.org/10.1017/9781108659055`.

[132] **M. Kryszkiewicz**, “Encyclopedia of business analytics and optimization,” in IGI Global, 2014, ch. 1 The Cosine Similarity in Terms of the Euclidean Distance, pp. 1–11. DOI: `10.4018/978-1-4666-5202-6.ch223`.

[133] **T. Chanwimalueang and D. P. Mandic**, “Cosine similarity entropy: Self-correlation-based complexity analysis of dynamical systems,” *Entropy-switz.*, vol. 19, no. 12, p. 652, 2017.

[134] **S. Scheid and S. Vogl**, *Data Science, Grundlagen, Methoden und Modelle der Statistik*. Carl Hanser Verlag München, 2021, ISBN: 978-3-446-47001-9.

[135] **S. Papp, W. Weidinger, K. Munro, B. Ortner, A. Cadonna, G. Langs, R. Licandro, M. Meir-Huber, D. Nikolić, Z. Toth, B. Vesela, R. Wazir, and G. Zauner**, *Handbuch Data Science und KI*. Carl Hanser Verlag München, 2022, ISBN: 9783446469471.

[136] **N. Y. Ning, Z. P. Zheng, L. Q. Zhang, and M. Tian**, “An excellent ozone-resistant polymethylvinylsiloxane coating on natural rubber by thiol-ene click chemistry,” *Express Polym. Lett.*, 2014.